Understanding recovery behavior of advanced high strength automotive steels

A thesis

Submitted

by

S JANAKIRAM

In partial fulfillment of the requirements for the award of the degree of

Doctor of Philosophy

In

Materials Engineering

Under the supervision of

Prof. Jai Prakash Gautam

Professor, School of Engineering Sciences and Technology, University of Hyderabad

Dr. P. Sudharshan Phani

Scientist - F, International Advanced Research Centre for Powder Metallurgy and New Materials (ARCI), Hyderabad



School of Engineering Sciences and Technology,

University of Hyderabad, Hyderabad,

India.

DECLARATION

I, S. JANAKIRAM declare that this thesis work entitled "Understanding recovery

behavior of advanced high strength automotive steels", submitted in partial fulfillment

of the requirements for the award of **Doctor of Philosophy**, in Materials Engineering at the

School of Engineering Sciences and Technology (SEST), University of Hyderabad is

completely my own work except for those referred. This work was carried out under the

supervision of Prof. Jai Prakash Gautam and Dr. P. Sudharshan Phani. This report is

a record of bonafide work carried out by me and the results incorporated in it have not been

reproduced/copied from any source. This work has not been submitted to any other

University or Institute for the award of any other degree or equivalent.

S. Janak Lom

S. JANAKIRAM

Reg. No.: 12ETMM05

School of Engineering Sciences and Technology,

University of Hyderabad



CERTIFICATE

This is to certify that the thesis work entitled "Understanding recovery behavior of advance high strength automotive steels", submitted by S. JANAKIRAM bearing Reg. No. 12ETMM05 in partial fulfillment of the requirements for the award of the degree of Doctor of Philosophy in Materials Engineering is a bonafide record of the work that has been carried out by him under my supervision. This thesis has not been submitted previously in part or in full to this or any other University or Institution for the award of any degree or diploma.

Thesis Supervisor

Prof. Jai Prakash Gautam

Professor, School of Engineering

Sciences and Technology University

School of Hxderabad

Lan

Dr. P. Sudharshan Phani

Scientist - F, International Advanced Research Centre for Powder Metallurgy and New Materials (ARCI), Hyderabad

Approved by

Prof. Dibakar Das

Prof. Dibakar Das

Dean.

School of Engineering Sciences and Technology

School of Engineering Sciences and Teenholders and 500 046

University of Hyderabad



CERTIFICATE

This is to certify that the thesis entitled "Understanding recovery behavior of advanced high strength automotive steels" submitted by S. JANAKIRAM bearing registration number 12ETMM05 in partial fulfillment of the requirements for the award of Doctor of Philosophy, in Materials Engineering at the School of Engineering Sciences and Technology (SEST) is a bonafide work carried out by him under my supervision and guidance. This thesis is free from plagiarism and has not been submitted previously in part or in full to this or any other University or Institution for the award of any degree or diploma.

- a. Part of this thesis has been published in,
 - 1. Scripta Materialia DOI 10.1016/j.scriptamat.2020.113676.
- b. Presented in the following conferences:
 - 1. Rex-GG, August 4-9th, 2019 (International)
 - 2. DSL, Jun 25-29, 2018 (International)
 - 3. ICOTOM, Nov 5-10, 2017 (International)
 - 4. AHSS, Feb 22-23, 2017 (International)

Further, the student has passed the following courses towards the fulfillment of coursework requirements for Ph.D.

Course Code	Name	Credits	Pass/Fail
AC801	Research Methodology	4	Pass

and was exempted from doing coursework (recommended by Doctoral Committee) based on the following courses passed during her M.Tech. Program (in Int. M.Tech. /Ph.D. program) and the M.Tech. degree was awarded:

Course Code	Credits	Pass/Fail	
MT401	Thermodynamics and Phase Equilibria	4	Pass
MT402	Characterization of Materials	4	Pass
MT403	Advanced Engineering Mathematics	4	Pass
MT404	Seminar	2	Pass
MT405	Mechanical Behavior of Materials/Selection of Materials	4	Pass
MT406	Concepts of Materials Science	4	Pass
MT407	Materials Processing and Characterization Laboratory	4	Pass
MT408	Dislocation and Plasticity	2	Pass
MT451	Materials & Technologies for Energy Systems	4	Pass
MT452	Diffusion and Kinetics	2	Pass
MT453	Modeling and Simulation	4	Pass
MT454	Powder Metallurgy and Ceramics	4	Pass
MT455	Surface Engineering	4	Pass
MT456	Metal Forming Science and Technology	2	Pass
MT457	Laboratory	4	Pass
MT458	Seminar	2	Pass
MT500	Dissertation	18	Pass

Supervisor ASH GAUTAM

The professor of Engineering Sciences & Technology of Hyderabad University of Hyderabad Hyderabad-500 046.

Prof. Dibakar Das

School of Engineering Sciences and Technology
University of Hyderabad, Hyderabad 500 046.

ACKNOWLEDGEMENTS

First and foremost, I express my deep sense of gratitude and respect to my research supervisor *Prof. Jai Prakash Gautam*, Professor, for his keen interest, constant and valuable guidance, strong motivation, and constant encouragement during my research work.

I express my deep sense of gratitude and respect to my research co-supervisor Dr. Sudharshan $Phani\ Pardhasaradhi$, Scientist - E, ARCI, for helping me with Nanoindentation testing, analysis, his keen interest, constant and valuable guidance, strong motivation, and encouragement during my research work

I express my deep sense of gratitude and respect to my research collaborator *Prof. Leo A.I. Kestens Ghent University, Ghent, Belgium* for helping me with all the technical discussions and valuable guidance, during my research work and partially funding for all my conferences abroad.

My doctoral review committee members *Prof. Koteswararao V Rajulapati, and Dr. Swati Ghosh Acharyya and Prof. Pinaki Prasad Bhattacharjee* (IIT-Hyderabad) have been helpful, critical and supportive over the last several years in making this work better. I am also thankful to the Dean of School of Engineering Sciences and Technology, *Prof. Dibakar Das* and all other faculties in the department for providing me the facilities to carry out my research work. Heartfelt thanks would go out for *Dr. Sairam K. Malladi* IIT-Hyderabad for helping me in TEM measurements and analysis.

I would also like to thank the technicians and non-teaching staff of SEST.

I would like to thank Tata Steel Research, (RD&T), IJmuiden, The Netherlands for supplying the materials and DST FIST and DST PURSE for funding the instrumentation facility (FESEM-EBSD).

I would like to thank University Grants Commission (UGC), Ministry of Tribal Affairs Government of India for proving fellowship in the form of NFHE-ST.

I would like to thank, *Abhijit, Kamal Mankari, Amit, Vamsi Krishna Rentala, Jagdeesh, Aaksash*, and the entire team of *Prof. Jai Prakash Gautam* helped me with innumerable tricky problem sets and became some of my close friends.

Lastly, I thank my mom-dad for always supporting me in every endeavor. I would probably be somewhere else if it were not for my family's invincible and contagious optimism in me.

S. JANAKIRAM

Table of contents

<u>DEC</u>	CLARATION	2
<u>CEF</u>	RTIFICATE	3
<u>ACI</u>	KNOWLEDGEMENTS	5
1 Intro	oduction	17
1.1	High and advanced high strength steels	17
1.2	Materials usage in Future steels vehicles (FSV)	18
1.3	Thermomechanical processing of HSS/AHSS	19
1.4	Motivation	21
1.5	Thesis Objectives	23
1.6	Outline of thesis	23
2 Liter	rature review	27
2.	.1 Cold deformed state	27
2.	.1.1. Deformation in two-phase alloys	31
2.2 A	Annealing	33
2.3	Recovery	33
2.	.3.1 Polygonization	35
2.	.3.2 Sub grain formation	36
2.	.3.3 The influence of second phase particles upon recovery	37
2.	.3.4 Influence of particles on the growth of subgrain	37
2.	.3.5 Precipitation on subgrain formation	38
2.	.3.6 Sub grain growth controlled by coarsening particle:	38
2.	.3.6 Techniques employed to investigate recovery	39
2.	.3.8 Recovery kinetics	41
2.	.3.9 Recovery in IF steels.	42
2.	.3.10 Recovery in ELC steel.	43
2.	.3.11 Recovery in C-Mn steels.	44
2.4	Recrystallization	44
2.	.4.1 Factors affecting recrystallization	45
2.	.4.2 Mechanisms of nucleation	47
2.	.4.3 Effect of the second phase on recrystallization	49
2.	4.4 Recrystallization in low carbon steels	50

2.5	A critical review of literature	52
Exper	imental Procedure	56
3.1	Materials and their chemical composition	56
3.2	Thermomechanical processing:	57
3.3	Annealing	58
3.3	.1 Recovery annealing	58
3.3	.2 Partial recrystallized annealing	59
3.4	Sample preparation	60
3.4	.1 Sample preparation for EBSD	61
3.4	.2 Sample preparation for TEM	61
3.5	Characterization	61
3.5	.1 Optical and Scanning electron microscopy	61
3.5	.3 Electron backscatter diffraction:	63
3.5	5.5 Transmission electron microscopy (TEM)	64
3.6	Mechanical testing	64
3.6	.1 Micro Vickers hardness	65
3.6	5.2 Nano Indentation	65
3.7	Deconvolution of data	67
3.7	.1 Deconvolution of hardness data	68
3.7	.2 Deconvolution of EBSD data	69
Micro	structure and properties evolution in Cold Rolled High Strength Stee	75
4.1	Introduction	75
4.2	Experimental procedure:	77
4.2	.1 Chemical composition and processing	77
4.2	.2 Characterization and mechanical testing	78
4.3	Results	79
4.3	.2 Microstructure evolution after 80% cold rolling	80
4.3	.3 KAM evolution after Cold rolling	81
4.3	.4 Deconvolution of ferrite and pearlite after 80% Cold rolling	83
4.3	.5 KAM distribution of ferrite and pearlite	84
4.3	6.6 MHV evolution after cold rolling	85
4.3	.7 Nanoindentation hardness mapping after cold rolling	86
4.3	.8 Deconvolution from Hardness maps	87
Ha	rdness distribution of ferrite and pearlite after Cold rolling	88

4.4	Discussions	89
4.4	4.1 Microstructure and properties evolution cold rolling	89
4.4	4.2 Role of pearlite on structure and property correlation in ferrite and pearlite	90
4.5	Summary and conclusions	92
5 Insigh	nts on early recovery kinetics at 300 °C	97
5.1	Introduction	97
5.2	Experimental procedure:	100
5.2	2.1 Composition and processing:	100
5.2	2.2 Characterization and mechanical testing:	100
5.3	Results	101
5.3	3.1 Microstructural evolution by SEM	101
5.3	3.2 KAM evolution	102
5.3	3.3 KAM distribution	104
5.3	3.4 TEM analysis	107
5.3	3.5 Micro hardness	108
5.3	3.6 Nanoindentation mapping	109
5.3	3.7 Hardness of ferrite and pearlite	111
5.4	Discussion	112
5.4	1.1 Recovery kinetics	113
5.4	4.2 Role of pearlite on recovery kinetics at 300 °C	115
5.5	Summary and conclusions	118
6 Recov	very kinetics at 500 °C	125
6.1	Introduction	125
6.2	Experimental procedure:	126
6.2	2.1 Composition and processing:	126
6.2	2.2 Characterization and mechanical testing:	126
6.3	Results	127
6.3.1	Microstructural evolution with SEM	127
6.3.2	Kernel average misorientation (KAM) evolution	128
6.3.3	KAM distribution of ferrite and pearlite	130
6.3.4	TEM analysis	133
6.3.5	Micro Vickers hardness evolution	134
6.3.6	Nanoindentation mapping	135
6.3	3.7 Hardness distribution of ferrite and pearlite	

6.4	Discussion		
6.4	1 Recovery kinetics		
6.4	2 Role of pearlite on recovery kinetics at 500 °C		
6.5	Summary and conclusions		
7 Partia	recrystallization annealing at 700 °C		
7.1	Introduction		
7.2	Experimental details		
7.3	Results		
7.3	1 Microstructural evolution by SEM		
7.3	2 KAM evolution after annealing at 700°C		
7.3	3 Nanoindentation mapping		
7.3	4 Deconvolution from hardness map		
7.4	Discussion		
7.4	1 Role of pearlite		
7.5	Summary and conclusions		
Refere	ences		
8 Summ	8 Summary and conclusions and future scope of work		
8.1	Future scope of work,		

List of Figures

Figure 1-1	Relationships between strength and total elongation for low strength, conventional HSS, and AHSS steels	10
Figure 1-2	Materials usage for future steels vehicles	
Figure 1-3	Schematic of Thermomechanical processing in AHSS steels.	
Figure 2-1	Microstructural hierarchy after deformation by the slip in polycrystalline	.20
1 iguic 2-1	metals Dislocations (a), dislocation boundaries (b), deformation and transition	
	bands (c), shear bands (d)	20
Figure 2-2	Schematic showing grain subdivision (a) small and (b) large strain	
Figure 2-3	Change in cell size and misorientation of cell boundaries as a function of local	50
Tiguic 2-3	orientation in rolled pure iron	31
Figure 2-4	Deformation zone around particles in severely rolled polycrystalline [8]	
Figure 2-5	Stages of recovery in plastically deformed material	
Figure 2-6	Recovery by polygonization consisting of an edge dislocation in bent crystal.	
1180110 = 0	(a) Deformed condition (b) dislocation annihilation (c) tilt boundary formation.	35
Figure 2-7	Shows tilt boundary energy and the energy per dislocation as a function of	
1180110 = 1	misorientation.	35
Figure 2-8	High-resolution TEM electron micrograph of 10% deformed aluminum	
8	(a) deformed (b) annealed at 250 °C for 2 min. [3]	37
Figure 2-9	TEM micrograph showing Al2O3 particles pinning dislocation on grain	
8	boundary and LAGB in aluminum [11]	38
Figure 2-10	The coarsening of second phase particles controls the extended recovery	
Figure 2-11	SIBM of a boundary dividing a grain with low stored energy (E1) from one	
\mathcal{E}	with higher stored energy (E2), (b) pulling of the dislocation structures behind	
	the migrating boundary, (c) the migration of boundary is free of the dislocation	
	structure, and (d) SIBM beginning at a single big subgrain	48
Figure 2-12	Schematic microstructure showing a concurrent process of cementite dissolution	
	and recrystallization [32]	
Figure 2-13	Dissolved carbon content as a function of heating rate and dispersion of cementit	te
_	particle with varying particle spacing (λ) [32]	51
Figure 3-1	Schematic flow chat of materials thermomechanical processing and	
_	characterization	58
Figure 3-2	Schematic flow chat of static recovery	
Figure 3-3	Schematic flow chat of partial recrystallization	60
Figure 3-4	Schematic showing cross-section and surface used for measurement by different	
	techniques like SEM, EBSD, HARDNESS, TEM	61
Figure 3-5	Shows (a) optical micrograph with ferrite and pearlite band (b) monochrome	
	bitmap highlighting pearlite	62
Figure 3-6	Shows image quality map (a) consisting of recovered, recrystallized ferrite and	
	pearlite band (b) KAM map (c).	64
Figure 3-7	Showing (a) SEM, (b) hardness map from nanoindentation	67

Figure 3-8	Showing (a) SEM, (b) hardness map from nanoindentation (c) mechanical	
	(deconvoluted) phase map showing binned regions of ferrite, pearlite and (d)	
	hardness histogram of individual phase features	69
Figure 3-9	Shows ferrite and pearlite obtained from (a) SEM and EBSD (b) IQ map,	
	(c) KAM map	71
Figure 3-10	(a) SEM micrograph, (b) hardness map, (c) deconvoluted map and (d) average	
	KAM of individual phase, ferrite –F and pearlite -P	72
Figure 4-1	Hot rolled microstructures consisting of only ferrite in (a) Alloy 1 and ferrite	
	pearlite phases, (b) Alloy 2, (c) Alloy 3 (d) Alloy 4	80
Figure 4-2	Cold rolled microstructures with ferrite (a) ULC and ferrite pearlite phases, (b)	
	HSLA, (c) DP600 (d) DP600	81
Figure 4-3	IQ and Kernel average misorientation (KAM) showing evolution of local	
	grain misorientation and strain distribution in cold rolled microstructures	
	with ferrite in (a) Alloy 1 and ferrite-pearlite phases, (b) Alloy 2	
	(c) Alloy 3 (d) Alloy 4 banded pearlite.	83
Figure 4-4	IQ and deconvoluted maps of cold rolled microstructures with ferrite in	
	(a) Alloy 1 and ferrite-pearlite phases, (b) Alloy 2 (c) Alloy 3	
	(d) Alloy 4 banded	84
Figure 4-5	Showing KAM distribution of (a) ferrite and (b) pearlite after 80% cold	
	rolling in Alloy 1, Alloy 2, Alloy 3, and Alloy 4.	85
Figure 4-6	Hardness evolution after cold rolling in Alloy 1, Alloy 2, Alloy 3, Alloy 4	86
Figure 4-7	Shows (a) SEM micrographs and (b) hardness maps 80% cold rolled	
	microstructures with ferrite in alloy 1 and ferrite-pearlite phase's alloy 2,	
	alloy 3, and alloy 4.	87
Figure 4-8	Showing (a) SEM micrographs and (b) deconvoluted maps in alloy 1	
	consisting of only ferrite and ferrite-pearlite phase's alloy 2, alloy 3,	
	and alloy 4	88
Figure 4-9	Showing hardness distribution of (a) ferrite and (b) pearlite of 80% cold	
	rolled steel sheets in Alloy 1, Alloy 2, Alloy 3, Alloy 4	89
Figure 4-10	Role of pearlite on KAM misorientation and hardness in (a) ferrite and	
	(b) pearlite after 80% cold rolling in alloy 1, alloy 2, alloy 3 and alloy 4	92
Figure 5-1	Shows microstructural changes after recovery annealing at 300° for	
	30, 60,120 and 300 min of soaking time in (a) Alloy 1, and ferrite pearlite	
	phases, (b) Alloy 2, (c) Alloy 3 (d) Alloy 4	102
Figure 5-2	Kernel average misorientation (KAM) changes after recovery annealing	
	at 300° for 30, 60,120 and 300 min of soaking time in (a) Alloy 1, and	
	ferrite pearlite phases, (b) Alloy 2, (c) Alloy 3 (d) Alloy 4	104
Figure 5-3	Kernel average misorientation (KAM) distribution of ferrite and pearlite	
	from cold rolled to recovery annealed at 300 °C at a different soaking time	
	in alloy 1, alloy 2, alloy 3, and alloy 4	106
Figure 5-4	TEM micrographs of ferrite (a, b, c) and pearlite (d, e, f) in (a, d) cold	
	rolled and subsequently recovery annealed at 300 °C for (b, e) 30 min	
	and (c, f) 300 min of soaking time. Images in ferrite and pearlite were	
	acquired along the $z = [001]$ axis	108

Figure 5-5	Micro Vickers hardness as a function of soaking time after recovery	
	annealing at 300 °C for 30, 60, 120,300 min of soaking time in Alloy 1,	
	Alloy 2, Alloy 3 and Alloy 4 [28]. Hardness at 0 min refers to the	100
F: 7.6	cold-rolled state.	109
Figure 5-6	Nanoindentation hardness mapping of alloy 1, alloy 2, alloy 3/4 in cold	111
T: 6.5	rolled state and after recovery annealing at 300 °C for 30 min	111
Figure 5-7	Hardness histograms of ferrite and pearlite in alloy 1, alloy 2, alloy 3/4	440
	in cold rolled state and after recovery annealing at 300 °C for 30 min	
Figure 5-8	The fractional change in hardness as a function of time at 300 °C	113
Figure 5-9	Hardness in (a) bulk ferrite and (b) pearlite as a function of pearlite	
	fraction after cold rolling and recovery annealing at 300 °C for 30 min	118
Figure 6-1	SEM microstructural changes after recovery annealing at 300° for	
	30, 60,120 and 300 min of soaking time in (a) Alloy 1, and ferrite	
	pearlite phases, (b) Alloy 2, (c) Alloy 3 (d) Alloy 4 [8]	128
Figure 6-2	Kernel average misorientation (KAM) changes after recovery annealing	
	at 300° for 30, 60,120 and 300 min of soaking time in (a) Alloy 1, and ferrite	
	pearlite phases, (b) Alloy 2, (c) Alloy 3 (d) Alloy 4 F-ferrite, P-pearlite	130
Figure 6-3	Kernel average misorientation (KAM) distribution of ferrite and pearlite	
	from cold rolled to recovery annealed at 300 °C at a different soaking time	
	in alloy 1, alloy 2, alloy 3, and alloy 4	132
Figure 6-4	TEM micrographs of ferrite (a, b, c) and pearlite (d, e, f) in (a, d) cold	
	rolling and subsequently recovery annealed at 500 °C for (b, e) 30 min	
	and (c, f) 300 min of soaking time. Images in ferrite and pearlite were	
	acquired along the $z = [001]$ axis.	134
Figure 6-5	Micro Vickers hardness as a function of soaking time after recovery	
	annealing at at 500 °C for 30, 60, 120,300 min of soaking time in Alloy 2,	
	Alloy 3 and Alloy 4 [8]. Hardness at 0 min refers to the cold-rolled state	135
Figure 6-6	Nanoindentation hardness mapping of alloy 1, alloy 2, alloy 3/4 in cold	
C	rolled state and after recovery annealing at 300-500 °C for 30 min	136
Figure 6-7	Hardness histograms of ferrite and pearlite in alloy 1, alloy 2, alloy 3/4	
8	in cold rolled state and after recovery annealing at 300-500 °C for 30 min	138
Figure 6-8	The fractional change in hardness as a function of log (1+at) at 500 °C	
Figure 6-9	Hardness of (a) bulk ferrite and (b) pearlite as a function of pearlite fraction	
118010 0 >	after cold rolling and recovery annealing at 500 °C for 30 min	144
Figure 7-1	shows hardness changes as a function of soaking time (a) and percentage	
115010 / 1	changes in hardness as a function of soaking time (b) in alloy 2, alloy 3,	
	and alloy 4 on annealing at 700 °C	151
Figure 7-2	Microstructural changes on partial recrystallization annealing at 700 °C	131
rigure 7-2	• • •	151
E: 7.2	for various soaking time in (a) alloy 2 (b) alloy 3 (c) alloy 4	131
Figure 7-3	SEM showing changes in ferrite and pearlite in (a, b, c) and only pearlite	150
Ei 7. 4	in (d, e, f) of alloy 2, alloy 3 and alloy 4	152
Figure 7-4	Shows microstructural changes after annealing at 700° (a) IQ and	154
	(b) KAM maps in alloy 2, alloy 3, alloy 4	154

Figure 7-5 Shows microstructure and corresponding hardness changes in		
	(a) IQ map, (b) hardness map (c) hardness map overlaid by grain	
	boundary map after annealing 700°C in alloy 2, alloy 3, and alloy 4	156
Figure 7-6	Shows recrystallized, recovered ferrite and pearlite after annealing	
	at 700 °C in (a) IQ map (a) and (b) deconvoluted maps overlaid by	
	grain boundary map, in alloy 2, alloy 3, and alloy 4	157
Figure 7-7	Hardness histograms of alloys 2, alloy 3 and alloy 4	158
Figure 7-8	Shows hardness vs temperature in individual phases' ferrite and pearlite	
	in alloy 2 and alloy 3.	162
Figure 7-9	Schematic of structural changes in ferrite- pearlite in (a) cold rolled state,	
	recovery at (b) 300 (c) 500 °C and partial recrystallization (d) 700 °C	163

Abstract

Tailoring of cold rolling to promote recovery and recrystallization process during annealing in single phase steels is well understood. In contrast, HSS/AHSS consists of ferrite-pearlite as the initial cold rolled microstructure. The recovery and recrystallization behavior in the ferrite might be different from pearlite. Understanding the behavior of individual phases is important in optimizing the properties and design of AHSS. This study investigates the early recovery, recovery behavior at 300, 500 °C and partial recrystallization at 700 °C for various soaking times after 80% cold rolling. Mainly pearlite fraction and its distribution were varied in three HSS/AHSS to investigate the role of pearlite at different annealing temperatures in comparison to single ferrite consisting steel. It is quite challenging to investigate recovery with only microscopy techniques due to subtle changes in structure. So we provide a comprehensive understanding of the correlative investigation across the multiple length scales using SEM, EBSD, TEM and nanoindentation. This study reveals the temperature and composition-driven recovery kinetics at 300 and 500 °C. A combination of electron microscopy and nanoindentation and a simple kinetics model enables new insights on what drives the kinetics and/or the dominating mechanisms at different temperatures. It was found that at 300 °C, single ferrite consisting of steels resulted in recovery, and interestingly ferrite-pearlite consisting HSS resulted in increasing hardness from the cold rolled state. Hardness increases show a clear dependence on the pearlite fraction and soaking time. Cottrell kinetics suggest and obey $t^{2/3}$ in the case of banded pearlite distribution. Whereas in non-banded pearlite

distribution the amount of free carbon available decreases due to the presence of microalloying element Nb and the kinetics deviate $t^{2/3}$ law. Upon annealing at 500 °C, a significant decrease in hardness is observed in single ferrite consisting of steels mainly due to the onset of partial recrystallization. Whereas ferrite-pearlite consisting steels hardness decreases indicating recovery. Decreases in hardness were similar in all the three HSS steel consisting of ferrite and pearlite. Recovery kinetics suggest that fractional change in a property is inversely proportional to temperature and the logarithmic of time and follows khulmanns models. On annealing at 700 °C, boundary mobility response due to recrystallization ferrite was also captured and the structure-property correlation was established.

Chapter 1

Introduction

1

Since the early 1900s, steel has always been the material of choice for automakers all over the world. Steel represents approximately for around 65-70 percent of the average automobile's body weight and acts as the vehicle's skeleton. Each car requires around 900 kg of steel. As the cars must meet the new legislative regulations on greenhouse gas emissions, safety, durability, and acoustic comfort. The automotive industry's top priority today is to reduce vehicle weight to improve passenger safety and vehicle performance [1]. By proposing the concept of lightweight design, High strength steels (HSS) and Advanced High strength steels (AHSS) provide a convincingly reasonable solution to the above conflicting requirements [2–4]. These steels are the fastest growing material in today's automotive industry and a critical material for reducing vehicle mass.

1.1 High and advanced high strength steels

High Strength Steel (HSS) is a type of steel with a tensile strength of (270 to 700 MPa) as shown in the strength elongation banana diagram in Figure 1-1. Tensile strength higher than 700 MPa is referred to as AHSS. The principal difference between these steels is their microstructure. HSS either consists of a single ferrite phase or it may contain a small amount of pearlite in C-Mn steels. AHSS consists of ferrite with a combination of martensite, bainite, austenite, and/or retained austenite, in sufficient quantities to produce unique mechanical properties. AHSS has a higher strain hardening capacity than conventional steels, resulting in

a superior strength-ductility combination. They provide a distinct combination of low weight, high strength, and optimized formability, allowing automakers to use less material and thus significantly reduce vehicle weight. However, issues like formability and weldability are constraints in the development of HSS.

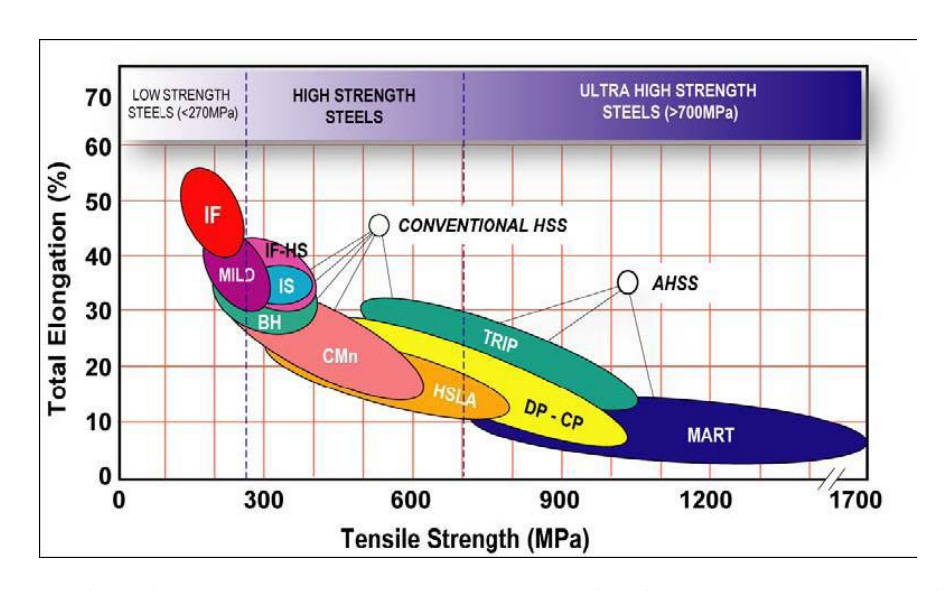


Figure 1-1 Relationships between strength and total elongation for low strength, conventional HSS, and AHSS steels [5]

1.2 Materials usage in Future steels vehicles (FSV)

Figure. 2 shows the pie chart and different grades of steel used in various components of car body structure for FSV such as battery electric (BEV) and plug-in hybrid electric (PHEV). It shows that approximately 75% of steels used are HSLA, DP, and TRIP steels, which are HSS and AHSS. These steels are mainly used in areas of vehicles such as crash zones, where energy absorption is extremely crucial, and door frames as shown in Figure 1-2.

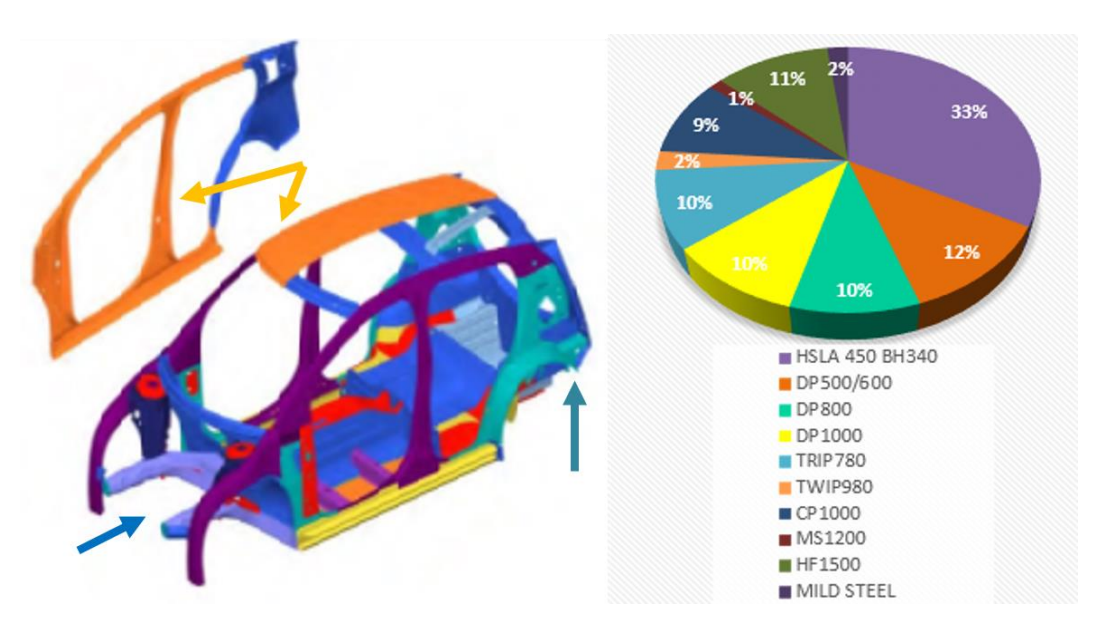


Figure 1-2 Materials usage for future steels vehicles [5]

1.3 Thermomechanical processing of HSS/AHSS

Thermomechanical processing is carried out to alter the properties (mechanical, chemical, physical) of the steel. The properties are large extent governed by the structure of the steels, the structure is commonly referred to as a microstructure. The correlation between changes in steel microstructure caused by thermomechanical processing and changes in their properties is critical to form and design HSS/AHSS steels with desired properties. Industrial thermomechanical processing of a sequence of HSS is shown as schematic in Figure. 1-3. Thermomechanical processing, includes slab reheating, hot rolling cold rolling, and annealing (recovery, recrystallization and phase transformation).

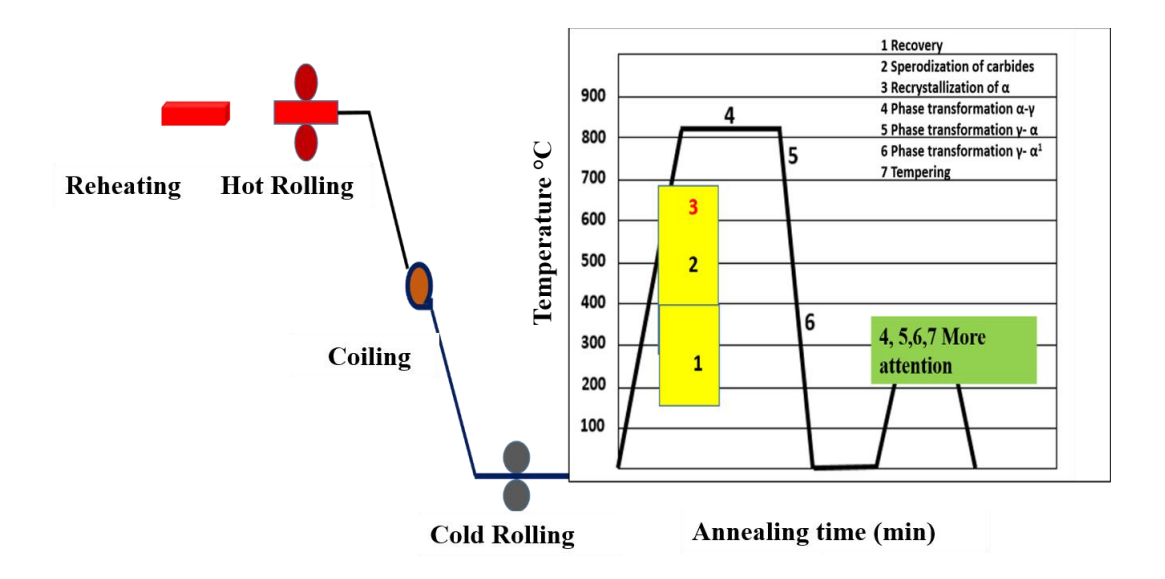


Figure 1-3 Schematic of Thermomechanical processing in AHSS steels.

During reheating of the steel slab, where the dissolution of all the particles takes place and a fully annealed structure is obtained. The temperature and time of reheating depend upon the chemical composition and the presence of Microalloying elements if any present in it. Reheated slabs are hot rolled at different temperatures, in the present case (above the austenite recrystallization) [6]. Followed by coiling to obtain ferrite pearlite structure, with required grain size and distribution. These steel sheets are further cold rolled to reduce thickness and improve the surface quality. Cold rolling also results in deformation and elongation of grain in the rolling direction. This also sets the condition for microstructural development during annealing.

During annealing heat is applied to the samples where major structural changes take place in the microstructure due to various annealing phenomena such as recovery, recrystallization and phase transformation, tempering takes place as shown in the schematic of Figure 1-3. During heating, pearlite dissolution and spherodization of cementite take place, whereas in ferrite recovery and recrystallization of ferrite (α) grains takes place. Which in turn, is decided by the heating rate, chemical composition and degree of cold rolling. Whereas in the phase transformation stage, ferrite (α), transforms to austenite (γ), carbide dissolution, austenite nucleation and growth, etc take place. Phase transformation temperature, soaking time and chemical composition decide the amount of austenite nucleation. After soaking in the phase transformation region the austenite transforms to martensite, ferrite (γ) transforms (α) to obtain the final dual phase ferrite martensite structure. Finally, tempering of martensite is carried out during the last stage. The microstructural evolution during thermomechanical processing will be discussed in detail in chapter 2.

In industrial grade high strength or low carbon automotive steels most of the research is focused on the processing, chemical composition and competition between recovery, ferrite recrystallization during austenite formation in intercritical annealing temperature was given lots of importance[7–11]. However, there are still gaps in the literature in systematic understating of physical metallurgy in recovery and partial recrystallization of AHSS. Recovery and recrystallization are important stages of structural changes which affect the final dual-phase or multi-phase microstructure during thermomechanical processing of the high-strength steel sheet. Investigating recovery helps in optimizing the process parameters during recrystallization, phase transformation and chemical composition, as well as to enhance the ductility by retaining cold rolled strength as much as possible by back annealing reported by ray et al.

1.4 Motivation

During recovery deformed structure is retained and subtle changes in structure occur due to a set of processes. Whereas during recrystallization migration of high angle grain boundary takes place and grains are free from any defects. However, these subtle changes lead to changes in mechanical properties.

Investigation of recovery with only electron microscopy is quite challenging due to subtle changes in structure and their evolution which occur at nm to mm scale. Also, it's difficult to see the effect of any local interaction that causes the changes in the structure and properties. Recovery is often monitored by, resistivity, XRD broadening, magnetic coercivity, hardness and yield strength which are bulk characterization techniques. However, these techniques do not give the local microstructural information of individual phase features causing the changes in properties. AHSS steels have ferrite-pearlite as their initial parent phase it is further challenging to investigate the role or contribution of each phase on the properties during the recovery or partial recrystallization annealing.

NanoBlitz 3D is a high-resolution indentation technique developed by nanoindenter iMicro® from Nanomechanics Inc. (now KLA Corporation), Oak Ridge, USA. Materials such as multiphase alloys, multi-layered coatings, and composites will be mapped using the technique. More than 10,000 data points are available in the mapping tool, where each indent takes less than a second to test. Machine Learning algorithms are used to process the data to determine the hardness and modules of individual phase features in the microstructure after mapping. Due to its advantage of mapping large areas in less time, using this technique, it is possible to monitor the hardness changes of individual phase constituents in the deformed and annealing condition. Additional complementary microscopy techniques were used to monitor the structural changes to establish structure-property correlation.

1.5 Thesis Objectives

The thesis's objective is to provide a comprehensive overview and a semi-quantitative link between microstructure, mechanical properties during each stage of thermomechanical processing i.e. after cold rolling, early recovery, recovery regime and partial recrystallization. It is well known that defect density increases during cold rolling, whereas, rearrangements, the annihilation of defects and carbon mobility take place during recovery. During recrystallization grain boundary mobility is expected. However, how these fundamental aspects are influenced by pearlite content is not well investigated. These aspects thus form the basis for framing the following objectives.

- 1) To understand the microstructural evolution after cold rolling, early recovery at 300°C and recovery annealing at 500°C and partial recrystallization at 700 °C, with varying the pearlite area fraction and its distribution
- 2) To investigate the micron-scale mechanical properties of individual constituents and their correlation with the microstructural changes observed under the EBSD and TEM.
- 3) Use simple models to provide new insights into the dominating mechanisms that drive the recovery kinetics at 300 and 500°C

1.6 Outline of thesis

This thesis is structured into five chapters that cover a variety of topics related to the studies conducted throughout this PhD study.

Chapter 1: This chapter serves as an introduction to the current thesis

<u>Chapter 2:</u> A literature review on the process taking place during thermomechanical processing mainly in cold rolling, recovery and recrystallization.

<u>Chapter 3:</u> This chapter presents the selection of different grades of HSS/AHSS steels, with varying chemical composition, their prior thermomechanical processing history, and thermal treatment given during the annealing stage in this work. All the experimental tools, strategy, characterization techniques used and sample preparation required for microstructural investigation at various length scales are described. The techniques used for mechanical property measurement and their post-processing analysis are also described.

Chapter 4: Presents the microstructure and properties evolution after 80% cold-rolled in different HSS/AHSS steels having variation in pearlite area fraction and distribution in comparison to single phase steels. We utilize these advances in characterization technology to quantify the properties of constituent phases/features and are then correlated to the microstructure changes determined by electron microscopy.

Chapter 5: This chapter investigates the static recovery behavior of 80% cold rolled HSS steels in comparison to single phase steels on recovery annealing at temperatures 300°C. Small-scale mechanical characterization and extensive microstructural characterization were carried out on various grades of HSS/AHSS after early recovery at 300 °C. Micron-scale microstructure property correlation and new insights on the recovery kinetics will be presented. The interplay of microstructure with properties is correlated with early recovery regime.

<u>Chapter 6:</u> This chapter investigates the static recovery behavior of 80% cold rolled HSS steels in comparison to single ferrite phase steels at 500 °C.

Chapter 7: This chapter presents the microstructural changes in individual phases' ferrite and pearlite on partial recrystallization at 700 °C, subsequent changes in properties are captured by nanoindentation and are correlated with the microstructural changes in three different HSS/AHSS steels.

<u>Chapter 8:</u> Presents the summary of the thesis and provides the ideas for future work to establish the structure-property correlation during the intercritical annealing of multiphase AHSS.

References

- [1] G.S. Patria, U.S.A. Combat, C. Development, A. Materials, Advanced High Strength Steel Utilization, Weight Reduction, and Cost Implications Presented by:, (2017). https://doi.org/10.13140/RG.2.2.31790.82240.
- [2] T. Nanda, V. Singh, V. Singh, A. Chakraborty, S. Sharma, Third generation of advanced high-strength steels: Processing routes and properties, Proc. Inst. Mech. Eng. Part L J. Mater. Des. Appl. 233 (2019) 209–238. https://doi.org/10.1177/1464420716664198.
- [3] E. Cañibano Álvarez, J.C. Merino Senovilla, J. Romo García, C. Maestro Martín, J. Sanz López, Integration of High Strength Steel (HSS) elements in automotive industry, Key Eng. Mater. 549 (2013) 340–348. https://doi.org/10.4028/www.scientific.net/KEM.549.340.
- [4] L. Zhao, J.G. Speer, P. Hodgson, N. Tsuji, Editorial: New Developments and Challenges in Advanced High-Strength Steels, Front. Mater. 8 (2021) 1–2. https://doi.org/10.3389/fmats.2021.786932.
- [5] S. Keeler, M. Kimchi, P.J. Mooney, Advanced High-Strength Steels Guidelines Version 6.0, WorldAutoSteel. (2017) 314. https://www.worldautosteel.org/projects/advanced-high-strength-steel-application-guidelines/.
- [6] T. Tanaka, Controlled rolling of steel plate and strip, Int. Met. Rev. 26 (1981) 185–209. https://doi.org/10.1179/imtr.1981.26.1.185.
- [7] J. Teixeira, M. Moreno, S.Y.P. Allain, C. Oberbillig, G. Geandier, F. Bonnet, Intercritical annealing of cold-rolled ferrite-pearlite steel: Microstructure evolutions and phase transformation kinetics, Acta Mater. 212 (2021). https://doi.org/10.1016/j.actamat.2021.116920.
- [8] C. Zheng, D. Raabe, Interaction between recrystallization and phase transformation during intercritical annealing in cold-rolled dual-phase steel: A cellular automaton model, Acta Mater. 61 (2013) 5504–5517. https://doi.org/10.1016/j.actamat.2013.05.040.
- [9] M. Calcagnotto, Y. Adachi, D. Ponge, D. Raabe, Deformation and fracture mechanisms in fine-and ultrafine-grained ferrite/martensite dual-phase steels and the effect of aging, Acta Mater. 59 (2011) 658–670. https://doi.org/10.1016/j.actamat.2010.10.002.
- [10] N. Peranio, Y.J. Li, F. Roters, D. Raabe, Microstructure and texture evolution in dual-phase steels: Competition between recovery, recrystallization, and phase transformation, Mater. Sci. Eng. A. 527 (2010) 4161–4168. https://doi.org/10.1016/j.msea.2010.03.028.
- [11] S.S. Ghasemi Banadkouki, E. Fereiduni, Effect of prior austenite carbon partitioning on martensite hardening variation in a low alloy ferrite-martensite dual phase steel, Mater. Sci. Eng. A. 619 (2014) 129–136. https://doi.org/10.1016/j.msea.2014.09.041.

Chapter 2

Theoretical background

2`

This chapter provides a brief overview of the fundamental processes or micromechanisms involved during the cold rolling and annealing mainly in (recovery, recrystallization) related to this thesis. The deformed energy present during cold rolling is the driving force for recovery and recrystallization. All the above processes interact with each other in many ways. This chapter mainly focuses on techniques used to characterize microstructural evolution and factors affecting them during the cold rolling, recovery and recrystallization mainly in steels.

2.1 Cold deformed state

Metallic materials undergo plastic deformation such as cold rolling, forging, drawing, etc, to produce useful end products. Cold rolling is a widely used deformation process to make thin sheets, strips with good dimensional tolerance and surface finish. Cold rolling is generally carried out below ~0.3 Tm, (Tm refers to the absolute melting point of the material).

During cold rolling of metallic polycrystalline material, a series of changes take place as listed below.

- Grain changes its overall shape, where equiaxed grain transformed as pancaked
 after cold rolling and grain elongates in the rolling direction causing to increase
 in the grain boundary area.
- Substructure formation takes place within the grain and point defects are generated.

 Sub structural changes are associated with the formation and accumulation of dislocations

The majority of energy expended during cold deformation appears as heat, with only a small amount stored in the metal as strain energy in the form of various lattice defects [1]. The amount of stored energy retained is determined by the deformation process and other variables such as material composition, as well as the rate and temperature of cold deformation.

The principal mode of deformation in simple cubic materials is either by slip or twinning. In low carbon steels, plastic deformation is due to crystallographic slip. The active slip planes are {110}, {112, {123}, in the closed packed direction <111> for BCC materials [2]. During deformation crystals generally change their orientation, different orientations develop within the original grain in most cases leading to subgrain division and fragmentation. It is well known that the microstructure is subdivided at various length scales, during deformation.

The hierarchy of the microstructural evolution in polycrystalline materials deformed by slip is shown in Figure 2-1. [3].

Initially, dislocations are formed as random structures or as tangles, these dislocations forms cells and subgrain structures as a result of the dynamic recovery process. Cells are the smallest volume in the cold rolled structure as shown in Figure 2-1(a-b). During large-scale deformation of a coarse-grained material subdivides into different orientations as a result of either inhomogeneous stresses transferred by adjoining grain or the intrinsic instability of the grain. The resulting deformation bands divergent orientations can be produced by using several slip mechanisms. Transition bands are those with narrow regions between the deformation bands which can be diffused or sharp as shown in Figure 2-1(c). In polycrystalline material shear bands occurs on a plane inclined to the rolling plane, and are non-crystallographic in nature.

Shear bands pass through multiple grains and even extend throughout the specimen causing plastic instability as shown in Figure 2-1(d).

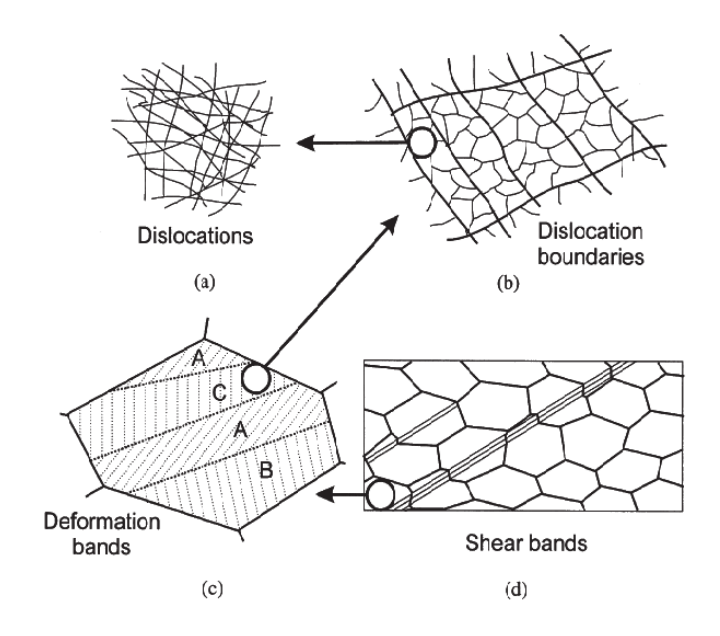


Figure 2-1 Microstructural hierarchy after deformation by the slip in polycrystalline metals Dislocations (a), dislocation boundaries (b), deformation and transition bands (c), shear bands (d) [3]

As a result of deformation, grain is fragmented into different oriented regions. Dislocation cell boundaries divide the areas into two ranges of scales, from small to large strain [4]. Small to medium strain, as shown in Figure 2-2(a) leads to long regular boundaries including single dense dislocation walls (DDWs) and double-walled micro bands (MB). At large strain as shown in Figure 2-2(b), small DWW and MB and replaced by flat cell blocks and are sandwiched by lamellar dislocation boundaries (LBs).

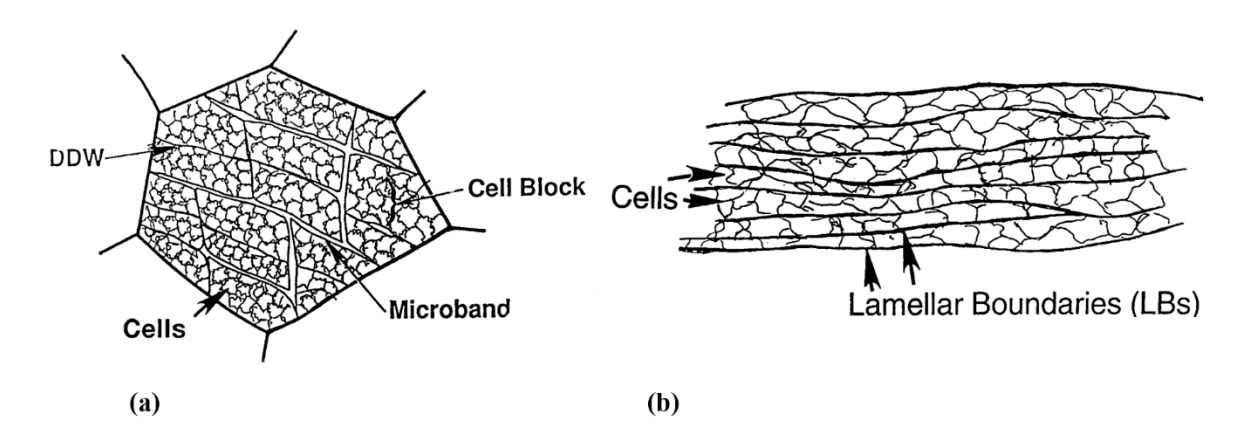


Figure 2-2 schematic showing grain subdivision (a) small and (b) large strain [4]

Cell boundaries are classified into two types of boundaries, incidental dislocation boundaries (IDB) and geometrically necessary boundaries (GNB) [5]. Formation of IDB takes place by random trapping of dislocations and has low misorientation angles on average. Whereas GNB consists of as DWWs, MB, LBs and sub boundaries that distinguish different deforming regions. GNBs are grouped in parallel families and have a unique orientation in relation to the deformation axis. For both IDBs and GNBs, the average misorientation angle increases and decreases their spacing to increase stress and strain. The spacing of GNBs decreases at a significantly higher rate than that of IDBs, which increases their misorientation angle. [4]. It is also important to mention that cell/subgrain size and misorientation is depended upon the grain orientation, resulting in variation in the stored energy in different components. Dillamore et al [6], as shown in Figure 2-3, the stored energy of the α -fiber components of the rolling texture in deformed iron in the following order E110>E111>112>E100.

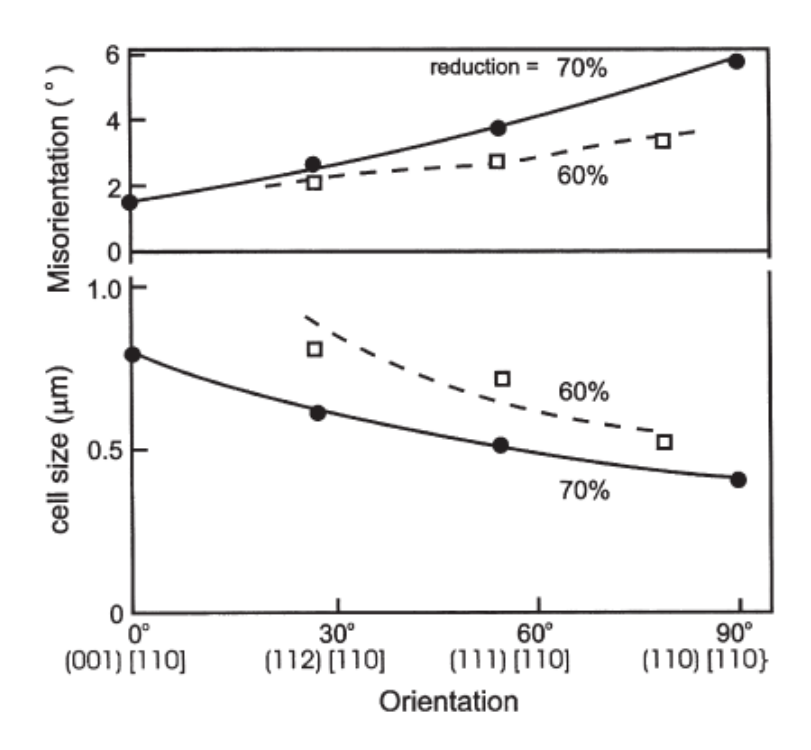


Figure 2-3 Change in cell size and misorientation of cell boundaries as a function of local orientation in rolled pure iron [6].

2.1.1. Deformation in two-phase alloys

Industrially most of the AHSS alloys consist of two phases, a matrix phase and a second phase that is dispersed. The presence of the second phase during deformation affects the microstructure and thus in turn affects annealing behavior. In this regard, the key elements of deformation in two-phase alloys are as follows

- The second phase or particle's impact on the overall density of dislocations.
 This has the potential to enhance the driving force for recrystallization.
- The particles/second phase influences the deformation and causes inhomogeneity of the matrix. This may have an impact on the availability of recrystallization sites.
- The type of the deformation structure in the proximity of the particles. This
 decides whether particle-simulation nucleation of recrystallization is possible.

In the case of large second phase particles during deformation large strain inhomogeneity is formed. Large particles obstruct dislocation slip and thus accumulate dislocation in their surroundings, where local lattice rotation typically about the <112> orientation axis, can occur, resulting in relatively high dislocation density zones with a large orientation gradient. These zones are referred two as particle deformation zones (PDZ) as shown in Figure 2-4 and are influenced by strain, particle size, particle shape, interface strength and matrix phase properties [7].

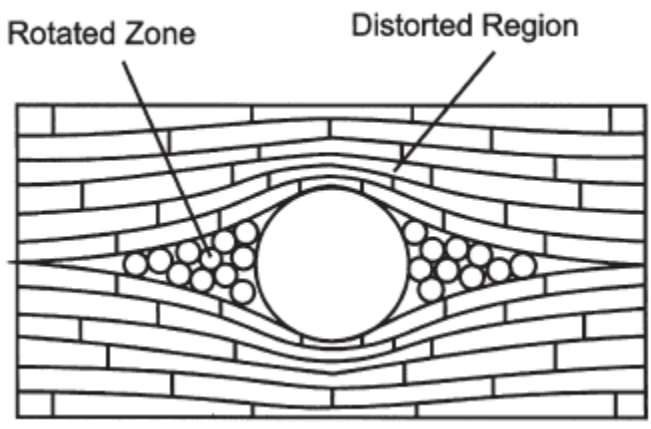


Figure 2-4 Deformation zone around particles in severely rolled polycrystalline [34]

Due to several experimental difficulties, there is a scarcity of quantitative data regarding deformation zones in polycrystalline materials [3]. Deformed zones in rolled alloys are often seen to be extended in the rolling direction as shown in Figure 2-4. Small subgrains of <0.1 µm are formed close to the second phase particles. A little further away from the particles subgrain are distorted and elongated. Transmission electron microscopy (TEM) and high-resolution electron backscatter diffraction (HR-EBSD) techniques have enabled us to measure orientation spread (gradient), size, shape and orientation of deformed zones in rolled polycrystalline materials [3].

2.2 Annealing

Annealing refers to heating a piece of material that has been previously cold deformed. Annealing permits an engineer in optimizing the various properties. As cold deformation increases hardness, strength and reduces ductility. Annealing is performed to enhance the ductility at the expense of strength/hardness.

During annealing various temperature phenomena take place, traditionally they are separated into three

- Recovery, releases stored energy without migration of high angle boundaries, and typically involves annihilation and rearrangements of dislocations to lower the stored energy.
- **2. Recrystallization**, migration of high angle boundaries takes place and it's driven by stored energy.
- **3. Grain growth**, the energy of the grain boundary combination drives the system to adopt a coarse grain size over time. The grain growth process is much slower than recrystallization because it has a much smaller driving force.

2.3 Recovery

The term "recovery" refers to changes in a deformed material that occur prior to recrystallization and the properties partially return the characteristics to their originally deformed values. Primarily, recovery is caused by changes in the material's dislocation structure. Dislocation recovery is a series of micro-mechanisms events, rather than a single microstructural change as depicted schematically in Figure 2-5. In the case of deformed material point defects and dislocations are formed during deformation. Point defects anneal out during low-temperature recovery, this is not considered a separate stage of the recovery in

cold deformed material and will not be further considered. A series of micro-mechanisms shown in Figure 2-5, such as rearrangements of dislocations into cells, the annihilation of dislocations inside the cells, formation of subgrain and growth can occur to lower the stored energy. All the above processes cause a slight increase in ductility, without a significant reduction in strength. The original grain boundary remains similar and will not be affected during recovery.

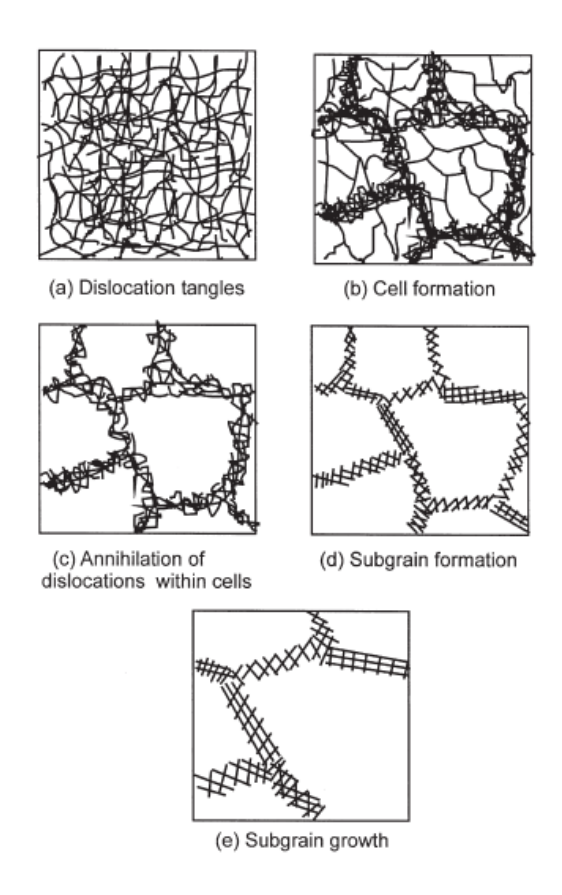


Figure 2-5 Stages of recovery in plastically deformed material. [3] (Humphrey and Hatherly 2004)

The process shown above occurs either during deformation as dynamic recovery or during annealing as static recovery. Different mechanisms have been proposed for sub-grain formation and growth.

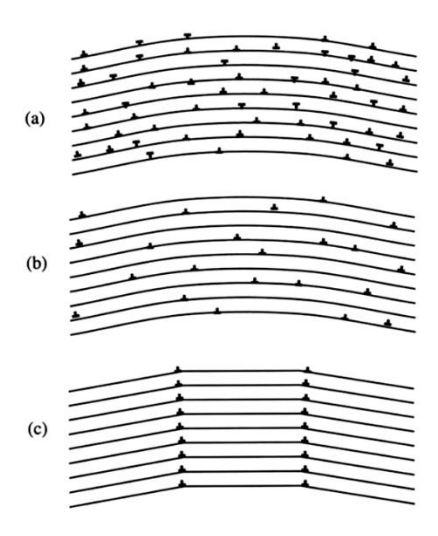


Figure 2-6 Recovery by polygonization consisting of an edge dislocation in bent crystal. (a) Deformed condition (b) dislocation annihilation (c) tilt boundary formation[3].

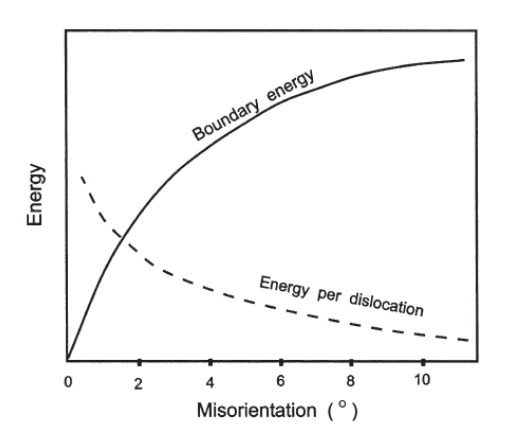


Figure 2-7 Shows tilt boundary energy and the energy per dislocation as a function of misorientation[3].

2.3.1 Polygonization

Polygonization is a fundamental recovery process that leads to rearrangements of dislocations and a decrease in lattice strain energy [8]. As shown in Figure. 2-6, dislocation of the same sign aligns itself into walls to form small angles, polygonized, or subgrain boundaries. These walls are known as tilt boundaries and are a simple type of low-angle boundary. Read-Shockley relationships state, that the energy of a tilt boundary increases with an increase in

misorientation. Increases in misorientation decrease the energy per dislocation as shown in Figure 2-7. As a result, there is a driving force to form, higher misoriented boundaries while the recovery proceeds or continues. Only a few experimental results of the energy of LAGB have been conducted.

2.3.2 Sub grain formation

On the subject to large strain in case of polycrystalline material, medium to high stacking fault materials, dislocation arrange in the form of 3D cells structure. Cell walls are complex dislocation tangles, and their size is dependent on the strain and material composition. Tangled cell walls on 10% deformation are shown in Figure 2-8 (a) and become a more regular dislocation network or LAGB and dislocation in the cell interior diminishes on annealing as in Figure 2-8 (b). The cells become the sub boundaries. This process leads to alter in mechanical properties i.e. a decrease in yield strength but work hardening rate increases as shown by Hasegawa and kocks [9].

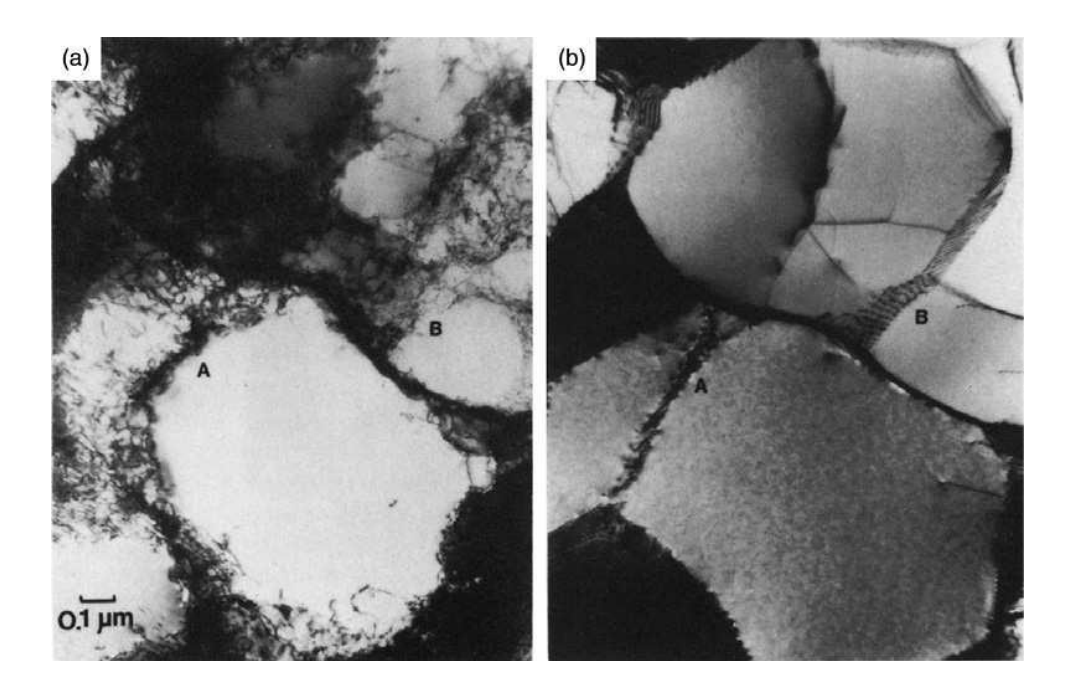


Figure 2-8 High-resolution TEM electron micrograph of 10% deformed aluminum (a) deformed (b) annealed at 250 °C for 2 min. [3]

2.3.3 The influence of second phase particles upon recovery

Second phase particles might present during the deformation or annealing. During deformation, the second phase particles are often distributed uniformly in microstructure, whereas during annealing their distribution is related to the dislocation structure [3]. This section deals with the stabilization of particles that do not alter during annealing.

Recovery mechanisms are influenced by second phase particles in many ways. During annealing rearrangement and annihilation of dislocations to form LAGB, the particles might immobilize the individual dislocation and retard the recovery process.

2.3.4 Influence of particles on the growth of subgrain

The fine particle dispersion might have a strong pinning influence on sub boundaries. These particles are mainly used to anchor and sustain the recovered substructure to increase the alloy

strength and creep resistance at high temperatures. Using an electron microscope as in Figure 2-9 has shown the pinning of individual dislocation boundaries by Al₂ O₃ particles in Aluminium by Hansen and Jones et al.[10].

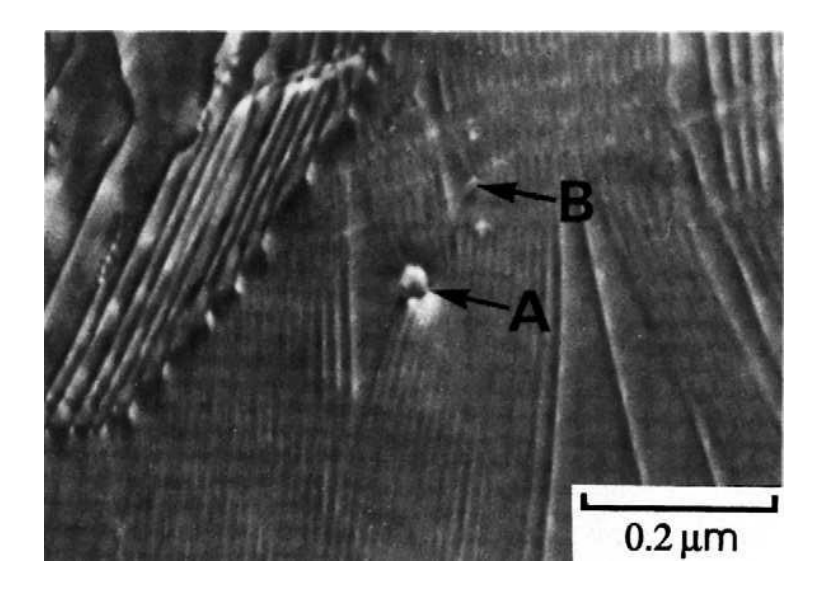


Figure 2-9 TEM micrograph showing Al2O3 particles pinning dislocation on grain boundary and LAGB in aluminum [10]

2.3.5 Precipitation on subgrain formation

During the annealing of supersaturated alloys, it is possible that precipitates might form on the recovered substructure. Hutchinson and Duggan [11] have observed in the Fe-Cu. Precipitation generally occurs on the LAGB, which exerts a strong pinning effect on the sub boundaries and limits the subgrain size.

2.3.6 Sub grain growth controlled by coarsening particle:

If after deformation particle-stabilized subgrain structure is formed, during the recovery annealing process the particles might coarsen. The coarsening of the particles controls the development of subgrain as shown in Figure 2-10. The growth of the subgrains with coarsening of particles is termed extended recovery.

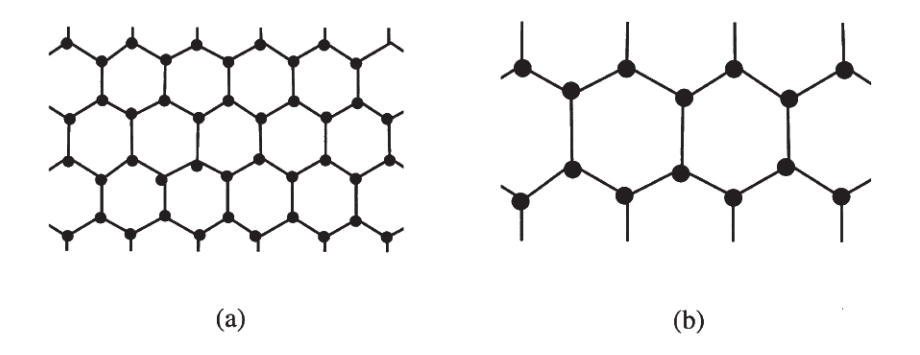


Figure 2-10 The coarsening of second phase particles controls the extended recovery[3].

2.3.6 Techniques employed to investigate recovery

The quantity of stored energy is determined by the number of defects, reorganization and their interaction with each other. As a result, crystalline materials structure sensitive property varies through the recovery process as a function of not just the quantity and distribution of defects, nevertheless the defect pattern also influences the individual property being measured. Investigating the evolution of deformed stored energy alone doesn't provide useful insights into the materials recovery behavior. Understanding and establishing the link between recovery microstructure (mesoscopic) and mechanical properties (macroscopic) is key.

Different techniques used to investigate recovery are divided into two groups

- Property changes monitoring techniques
- Microstructural evolution monitoring techniques

Microstructural evolution during annealing in recovery is monitored by transmission electron microscopy (TEM) [10]. Using this technique local dislocation configuration in the form of cells/ cell walls, sub boundaries. However, quantitative analysis of the grain is difficult due to the density of distribution in many places being too large to be resolved. Another method for characterizing microstructural information is Electron backscatter diffraction (EBSD) [12]. The advantage of this technique is that it can be used to investigate the orientation of many

grains in a large surface area in a short time. Microstructural data is directly obtained by X-ray peak broadening information, such as dislocation density, tiny crystal size and is used to quantitatively observe the changes in microstructure during recovery. Peak broadening information also provides the stored energy in different local orientations or micro-strain distribution [13]. The elastic stored energy of dislocation broadens the X-ray diffraction peaks from the deformed samples. Deconvoluting the broadening readings yields microstructural data such as dislocation density and crystallite size.

Property changes are monitored indirectly by hardness [12], yield/tensile strength [14], resistivity [15], magnetic coercivity [12]. Hardness tests are the most common mechanical assessments of metal softening after annealing. Hardness is defined as a material's resistance to deformation, as assessed by a standard test that assesses surface resistance to indentation. The ability to deform is determined by the number of dislocations and their mobility. The most frequent method for determining hardness is characterized by geometric shape, size and type of indenter and the applied load.

In micro Vickers hardness tester was used in the present thesis with a diamond indenter with a square base in the shape of a pyramid. The angle formed by the pyramid's two opposite faces is 136°. The Vickers hardness is determined by the load and area of the indentation. The relation is given below.

$$Hv = \frac{2L\sin\left(\frac{136^{\circ}}{2}\right)}{d^2}$$

Where L corresponds to load, D is the mean diagonal. Hardness accuracy is dependent upon the measurement of diagonals from an optical microscope and the sample surface area.

2.3.8 Recovery kinetics

During annealing, the evolution of the time-dependent structural parameters like hardness, yield strength, as well as microstructural parameters is used to determine the recovery kinetics. Recovery kinetics in polycrystalline materials follow a logarithmic decrease, which has been proven by several authors [16–18].

In zone refined iron, Michalak Paxton [17] observed logarithmic decay in hardness during isothermal recovery annealing. Initially decay in hardness is faster, but as time progresses it slows down to a regular plateau, regardless of the amount of deformation or purity. It is necessary to make a few observations to fully understand this type of time-dependent recovery kinetics behavior. The basic recovery kinetics are controlled by micro-mechanisms such as dislocation annihilation, dislocation rearrangements into subgrain and subgrain growth. Two alternative rate governing mechanisms have been proposed for the rearrangement and annihilation of dislocation, into low energy configuration; thermally induced glide or climb or cross slip of dislocation [19,20]. The rate-controlling mechanisms are critical for quantifying microstructural rearrangements and mechanical properties evolution over time. In this regard, many quantitative recovery models based on various rate-controlling mechanisms have been proposed in the literature [16,20]. The scope of this thesis does not allow for a consideration of these models.

It is worth noticing that the most often used recovery model is based on thermally activated dislocation glide and climb suggested by Kuhlmaan's [18]. Friedel et al. [19], The thermally activated glide or cross slip governs dislocation annihilation during recovery was investigated. It was claimed that the internal stress (σ) decreases the rate of recovery, and the rate of recovery

$$\frac{d\sigma}{dt} = -\text{c.} \exp\left(\frac{Q_o - \sigma\Omega}{RT}\right)$$
 Equation (1)

Where Q = slip activation energy

k= constant of Boltzmann,

T= temperature in °K

Q decreases as a function of internal stress σ

$$Q(\sigma) = Q_0 - C_2 \sigma$$

Hence,

$$\frac{d\sigma}{dt} = -C_1 \cdot \exp\left(\frac{-(Q_o - C_2\sigma)}{kT}\right)$$
 Equation (2)

$$\sigma = \sigma_o - \frac{kT}{C_2} \ln \left(1 + \frac{t}{to} \right)$$
 Equation (3)

Where, σ_0 is the flow stress with respect to time t =0

At times greater than t_0 decreases in a logarithmic manner. As a result, the activation for recovery is governed by the glide mechanism which is a thermally activated process. With increasing stored energy or dislocation density the activation energy reduces, and it increases during annealing. Similar results were also observed by Michalak Paxton [17] in deformed zone refined iron. They observed logarithmic hardness decay, which showed a fast initial decay before slowing down to a plateau region with increasing time.

2.3.9 Recovery in IF steels.

Mukunthan et al. [17] studied recovery kinetics of 80% cold-rolled Tin-Nb stabilized IF steels employing in situ X-ray peak resolution measurement in the temperature range of (500-600 °C). The activation energy Q during recovery increased from 173 KJ/mole at R₁=0.6

0 to 312 KJ/mole at $R_1 = 0.15$. They suggested that the higher activation energy attributed to the retardation of the recovery, due to excess solute of Ti and Nb in the solid solution and precipitation of fine carbides, nitrides Ti and Nb.

Recovery in IF steels were investigated by Khatirkar et al. [21] on 40, 60 and 80% cold-rolled IF steels samples, recovery annealed at 500 °C for (15-33 hrs). Recovery kinetics by the X-ray line profile measurement in combination with EBSD, recovery kinetics followed a logarithmic relationship. Recovery kinetics was influenced by initial deformation condition and orientation dependent. Significant recovery was observed in 80% of deformed conditions. Deformed γ (ND//<111>) fiber orientation had significant recovery in comparison to the θ (ND//<100>) fiber orientation. During recovery, in-grain misorientation and the number of grain interior and strain localizations both increase. Though the strain localization looked to be orientation insensitive, misorientation developments in ND// <111> grains/bands were more pronounced. The coarsening of γ -fiber bands was also visible in 80 % deformed IF steel. The exact methods and contribution leading to the rapid recovery kinetics in IF steels after 80 % deformed are still unknown.

2.3.10 Recovery in ELC steel.

Recovery in 84% cold-rolled ELC steels was investigated by Martinez-de-Guerenu et al. [12] in the temperature range of (300-500 $^{\circ}$ C). Magnetic coercive field (Hc) evaluation has been used to track the recovery process. Microstructural changes with Hc by the recovery were investigated using TEM and EBSD. The EBSD image quality maps demonstrate that the,

stored energy after cold rolling was distributed heterogeneously across distinct texture components. The γ -fiber grains stored a significant amount of energy and were incorporated in the form of the cellular substructure. During recovery, the cellular structure evolves into a larger subgrain substructure. The recovery rate is higher in the $\{1\ 1\ 1\}$ γ - fiber orientations, compared to other orientations. The recovery kinetics was investigated utilizing coercive field Hc, measurement [22]. As Hc is proportional to dislocation density ρ , $Hc \propto a \sqrt{\rho}$ where a is constant. The fraction of recovery R_y was defined as

$$1 - R_{y} = \frac{H_{c}}{H_{c}^{def}}$$

Where H_c^{def} is the coercive field of deformed condition. The fraction of recovery has been observed to increase the activation energy for the recovery process [22].

2.3.11 Recovery in C-Mn steels.

In C-Mn steels, Smith et al. [23] recovery of ferrite was investigated in the temperature range (150-600 °C), and also varied the stress and strain rate using a stress relaxation test. It was found that activation energy and activation volume during the recovery process varied with temperature, but not with strain or strain rate. The activation energy is close to dislocation core diffusion at low temperatures (150-300 °C). Activation energy is near lattice self-diffusion at higher temperatures (450-600 °C). The activation energy is not dependent on strain or strain rate. The rate-controlling mechanisms are due to thermally induced glide of jogged screw dislocation, which is decorated with the solute carbon atom, above 450 °C.

2.4 Recrystallization

Recrystallization refers to a process in which migration of high angle grain boundary (HGBA) takes place in the deformed or the recovered grain, where a new strain-free grain forms from

nuclei formed in the deformed grain. The only way to create a fully new grain structure with varying grain size, shape, orientation, or texture is to recrystallize after deformation. Recrystallization results in increases in ductility and a decrease in strength when compared to recovery.

When recrystallization is considered, five rules are generally followed, and they summarize the behavior during recrystallization [24].

These rules are

- At higher temperatures, a minimal amount of deformation is necessary to initiate recrystallization.
- 2. The smaller the degree of deformation, the required recrystallization temperature increases.
- 3. The temperature required for recrystallization is reduced by increasing the soaking times during annealing.
- 4. The recrystallized grain size is determined is primarily determined by the degree of deformation, with small grains resulting from a higher deformation.
- The temperature of recrystallization at a given degree of deformation will be increased by
 - Large initial grain size
 - Higher temperature of deformation.

2.4.1 Factors affecting recrystallization

Some of the major factors influencing the rate of recrystallization in materials are briefly described below [3].

- The degree of strain: an increase in the degree of cold deformation increases the
 density of dislocations, implying an increase in the stored energy of materials.

 An increasing degree of strain leads to increases in the differences in stored
 energy, which provides preferable sites for recrystallization and as a result,
 increases the rate of recrystallization.
- 2. Initial texture: as the stored energy is distributed heterogeneously according to the different orientations of the texture components. The rate of recrystallization of different texture components will different.
 - A finer grain size provides more stored energy after a small degree of deformation
 - As grain size increases, the formation of inhomogeneity such as shear bands increases, which serve as nucleation sites.
 - Grain boundaries are preferred sites of nucleation, the fraction of boundaries is higher in fine-grained materials.
 - Grain size influences the formation of deformed texture and as result, it will affect the recrystallization texture.
- 3. Solutes: the presence of solute have the potential effect of inhibiting recrystallization. The rate of recrystallization is slowed when the solute concentration in solid solution increases.
- 4. The temperature of deformation and strain rate: with a higher deformation temperature and low strain rate, the dynamic recovery process reduces the stored energy, resulting in a slower recrystallization rate.

5. The annealing temperature: The rate of recrystallization rises with increasing temperature since it is a thermally activated process. In the recrystallization process, the Arrhenius plot governs the relationship between the time and the temperature to some extent [3]. The time period for 50% recrystallization (t 0.5) is considered if the rate of recrystallization is used as a metric, the relationship is as follows

Rate =
$$1/t_{0.5}$$
 = C exp (- $\frac{Q}{RT}$)

Where C is constant, Q is the activation energy (in J/mol), R is the gas constant, and T is the temperature in degrees (Kelvin). A straight line with a slope is obtained by plotting ln (t 0.5) versus 1/T.

6. Heating rate: when the heating rate is raised, the recovery consumes less stored energy resulting in a higher recrystallization rate.

2.4.2 Mechanisms of nucleation

Three mechanisms are thought to be involved in the nucleation of recrystallization.

Nucleation and growth

Is the first classical mechanism of nucleation of recrystallization, which indicates the formation of defect-free new grain surrounded by a HAGB within deformed material? This mechanism is thought to occur near grain boundaries and second phase particles as well as within the deformation band (ex. shear bands)

Strain-induced boundary migration (SIBM)

SIBM is the second mechanism that develops when the stored energy across the grain boundary differs significantly. Figure 2-11 illustrates the schematic of SIBM. With the expansion of single or many subgrains, HAGB bulges out from one grain to the next. SIBM's new grains are oriented similarly to the old grain from which they bulged. SIBM is observed in low strain conditions which are traditionally recrystallized nucleation is less frequent as reported in [25]

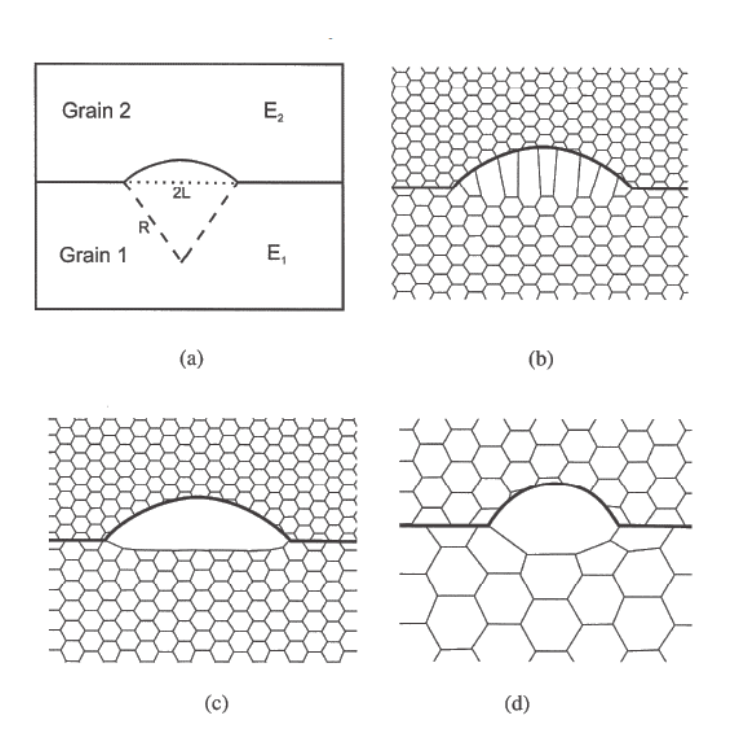


Figure 2-11 SIBM of a boundary dividing a grain with low stored energy (E1) from one with higher stored energy (E2), (b) pulling of the dislocation structures behind the migrating boundary, (c) the migration of boundary is free of the dislocation structure, and (d) SIBM beginning at a single big subgrain.[3]

Sub grain coalescence

Is the third mechanism for recrystallization nucleation [26,27]. During annealing, two adjacent subgrains rotate. The subgrain border between the two grans is removed when their

orientations become the same. The development of a HAGB and nucleation of recrystallization are the result of repeated coalescences process.

The first two mechanisms of recrystallization are similar in that they are both initiated by boundary migration. Many studies show that the most common process for generating new strain-free grain is the mobility of prior-existing grain boundaries in the case of iron [28].

2.4.3 Effect of the second phase on recrystallization

The behavior of recrystallization with second phase particles alters the microstructure in one of two ways [3]. The following are the significant influence on recrystallization with second phase particles.

- It is possible to increase the stored energy and as result, it increases the driving pressure for recrystallization.
- Big particles may act as recrystallization nucleation sites
- Closely spaced particles influenced by the pinning effect on both LAGB and HAGB

Recrystallization is favored by the first two effects, whereas the third tends to inhibit it. As a result, the kinetics of recrystallization, as well as the resultant grain size and texture, will be determined by which of these effects is dominating.

The alloy composition and processing determines the distribution, size and volume fraction of second phase particles and by varying these microstructure and texture can be controlled during recrystallization.

When the particles containing material are distorted, a large-diameter particle can produce a high local concentration of stored energy and large misorientation in the surrounding microstructure and therefore acts as a favorable nucleation site [29,30]. These high energy

zones typically increase to a distance of around a diameter of particle from the particle surface, implying that the size of zones is determined by the particle's size. As a result, if the strained region is greater than the critical nucleus size, nuclei can develop in these strained zones and instantly begin growing due to the misorientation of the surrounding microstructure.

If the particles are finely dispersed (d <0.1 μ m), the nucleation process will be retarded (Zener drag). As fine particles served as inhibitors to the dislocation movement and grain boundary [31,32].

2.4.4 Recrystallization in low carbon steels

Low carbon steels consist of cementite as the second phase in the ferrite matrix. Hutchinson et al [33] has reported that during annealing carbon atoms from the cementite dissolve into a ferrite matrix resulting in competition between carbide dissolution and nucleation of recrystallization as in Figure 2-12. The activation energy of recrystallization is higher than that of carbon dissolution in ferrite. As a result, a high temperature (i.e. fast heating rate) will accelerate recrystallization more than cementite dissolution where the inter-particle spacing has an important role.

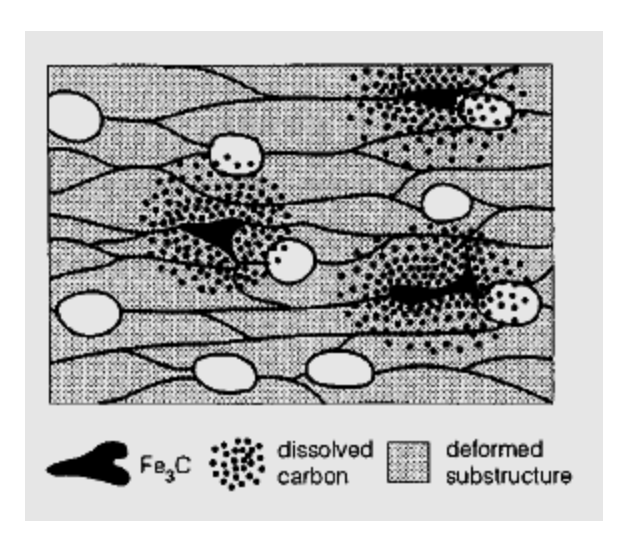


Figure 2-12 schematic microstructure showing a concurrent process of cementite dissolution and recrystallization [33]

Hutchinson et al. [33] varied the inter-particle spacing and calculated the dissolved carbon content as a function of the heating rate as shown in Figure 2-13. The outcome in Figure 2-13 clearly shows that fine spaced particles ($\lambda = 20~\mu m$) the average dissolved in the matrix is 50ppm, whereas coarse carbide spacing of ($\lambda = 80~\mu m$) gives rise to less than 10ppm during rapid annealing condition.

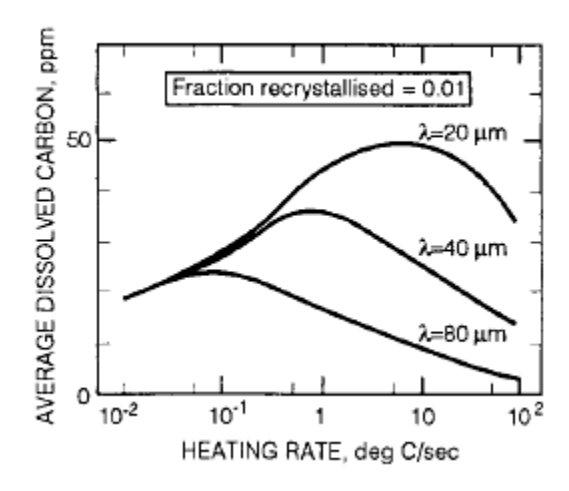


Figure 2-13 dissolved carbon content as a function of heating rate and dispersion of cementite particle with varying particle spacing (λ) [33]

2.5 A critical review of literature

The important microstructural changes during deformation and post deformation processing phenomena mainly recovery and recrystallization in the evolution of the microstructure and properties are extensively discussed.

Recovery observes subtle changes in the microstructure, unless carefully investigated it may go unnoticed. However, it is essential to have a better understanding of the recovery process because it sets the stage for recrystallization by consuming the material's stored energy before recrystallization and controlling the amount available to drive the subsequent recrystallization.

The context of this thesis is to understand the microstructure, and properties evolution after cold rolling, recovery and partial recrystallization annealing of cold rolled ferrite-pearlite HSS/AHSS. To date, no research has been conducted to investigate the relative recovery characteristic of the individual phases of ferrite-pearlite in HSS/AHSS. Ferrite-pearlite microstructure develops a compositional gradient as, pearlite consists of ferrite and cementite, where cementite is a carbon-rich region. Compositional gradient might leads to diffusion elements during annealing and may result in a different thermomechanical response in individual phases and might influence the final properties. Different HSS/AHSS were chosen in this study due to the compositional gradient and to assess the material response in post deformation annealing process.

Subsequent chapters present the experimental investigation performed to capture the recovery behavior in ferrite and pearlite. The heat treatment cycles used to investigate the recovery and partial recrystallization schedules are reported. The methods and methodology to capture the microstructural changes and their corresponding properties changes in

individual phase's ferrite and pearlite during recovery and partial recrystallization are discussed.

References

- [1] G. E.Dieter, Mechnaical Metallurgy, 1961.
- [2] William F. Hosford, Mechnaical behavior of materials, second edi, cambridge press, uinited kingdom, 2009.
- [3] A. Rollett, F. Humphreys, G.S. Rohrer, M. Hatherly, Recrystallization and Related Annealing Phenomena: Second Edition, Elsevier, 2004. https://doi.org/10.1016/B978-0-08-044164-1.X5000-2.
- [4] R.D. Doherty, D.A. Hughes, F.J. Humphreys, J.J. Jonas, D. Juul Jensen, M.E. Kassner, W.E. King, T.R. McNelley, H.J. McQueen, A.D. Rollett, Current issues in recrystallization: A review, Mater. Sci. Eng. A. 238 (1997) 219–274. https://doi.org/10.1016/S0921-5093(97)00424-3.
- [5] D.A. Hughes, N. Hansen, D.J. Bammann, Geometrically necessary boundaries, incidental dislocation boundaries and geometrically necessary dislocations, Scr. Mater. 48 (2003) 147–153. https://doi.org/10.1016/S1359-6462(02)00358-5.
- [6] C.J.E.S. and W.B.H. I. L. Dillamore, P. L. Morris, Transition Bands and Recrystallization in Metals, Proc. R. Soc. London. Ser. A, Math. Phys. 329 (1972) 405–420. https://doi.org/10.1016/S0140-6736(01)16090-3.
- [7] F.J. Humphreys, Dislocation and properties of real materials, in: Proceeding Conf. to Celebr. Fiftienth Anniv. Concept Dislocation Crystalls, institute of metals london, london, 1985: pp. 175–204.
- [8] C. RW, rercytsllization of single crystals after plastic bending, J. Inst. Met. 76(2) (1949) 121–143.
- [9] T. Hasegawa, U.F. Kocks, Thermal recovery processes in deformed aluminum, Acta Metall. 27 (1979) 1705–1716. https://doi.org/10.1016/0001-6160(79)90085-3.
- [10] A.R. Jones, N. Hansen, The interaction between particles and low angle boundaries during recovery of aluminium-alumina alloys, Acta Metall. 29 (1981) 589–599. https://doi.org/10.1016/0001-6160(81)90140-1.
- [11] W.B. Hutchinson, B.J. Duggan, Influence of precipitation on recrystallization and texture development in an iron–1·2% copper alloy, Met. Sci. 12 (1978) 372–380. https://doi.org/10.1179/msc.1978.12.8.372.
- [12] A. Martínez-de-Guerenu, F. Arizti, M. Díaz-Fuentes, I. Gutiérrez, Recovery during annealing in a cold rolled low carbon steel. Part I: Kinetics and microstructural characterization, Acta Mater. 52 (2004) 3657–3664.

- https://doi.org/10.1016/j.actamat.2004.04.019.
- [13] N. Rajmohan, J.A. Szpunar, Cold Rolling and Stress Relieving, 15 (1999) 1259–1265.
- [14] B. Kim, D. San-Martin, P.E.J. Rivera-Díaz-del-Castillo, Modelling recovery kinetics in high-strength martensitic steels, Philos. Mag. Lett. 97 (2017) 280–286. https://doi.org/10.1080/09500839.2017.1342048.
- [15] S. Takaki, J. Fuss, H. Kugler, U. Dedek, H. Schultz, Resistivity Recovery of High Purity and Carbon Doped Iron Following Low Temperature Electron Irradiation., Radiat. Eff. 79 (1983) 87–122. https://doi.org/10.1080/00337578308207398.
- [16] Y.B. and P.G. M. Verdier, Recovery of AlMg Alloys: Flow stress and strain-hardening properties, Acta Mater. 47 (1999) 127–134.
- [17] Michalak J T and Paxton H W, No Title, Trans. Metall. Soc. AIME. 221 (1961) 850.
- [18] J.R. D. Kuhlmann, G. Masing, Zeitschrift Fuer Met. Res. Adv. Tech. 40 (1949) 241–246.
- [19] J. friedel, Dislocations, International, pergamon, oxford, 1964.
- [20] E. Nes, Recovery revisited, Acta Metall. Mater. 43 (1995) 2189–2207. https://doi.org/10.1016/0956-7151(94)00409-9.
- [21] R. Khatirkar, B. Vadavadagi, S.K. Shekhawat, A. Haldar, I. Samajdar, Orientation dependent recovery in interstitial free steel, ISIJ Int. 52 (2012) 884–893. https://doi.org/10.2355/isijinternational.52.884.
- [22] A. Martínez-de-Guerenu, F. Arizti, I. Gutiérrez, Recovery during annealing in a cold rolled low carbon steel. Part II: Modelling the kinetics, Acta Mater. 52 (2004) 3665–3670. https://doi.org/10.1016/j.actamat.2004.04.020.
- [23] A. Smith, H. Luo, D.N. Hanlon, J. Sietsma, S. Van Der Zwaag, Recovery processes in the ferrite phase in C-Mn steel, ISIJ Int. 44 (2004) 1188–1194. https://doi.org/10.2355/isijinternational.44.1188.
- [24] J.E. Burke, D. Turnbull, Recrystallization and grain growth, Prog. Met. Phys. 3 (1952). https://doi.org/10.1016/0502-8205(52)90009-9.
- [25] Willian C leslie, The physical metallurgy of steels, the physic, hemisphere, 1981.
- [26] James C.M.Li, Possibility of subgrain rotation during rercystallization, J. Appl. Phys. 33 (1962) 2958.
- [27] Hu Hsun, Direct observation on the annealing of Si-Fe crystal by electron microscope, Trans. Metall. Soc. AIME. 224 (1962) 75–84.
- [28] W.C. Leslie, The quench-ageing of low-carbon iron and iron-manganese alloys an electron transmission study, Acta Metall. 9 (1961) 1004–1022. https://doi.org/10.1016/0001-6160(61)90244-9.
- [29] F.J. Humphreys, The nucleation of recrystallization at second phase particles in deformed aluminium, Acta Metall. 25 (1977) 1323–1344.

- https://doi.org/10.1016/0001-6160(77)90109-2.
- [30] N. Hansen, acceleration and delayed recystallization in dispersion hardened alloys, Mem. Sci.Rev.Met. 72 (1975) 189–203.
- [31] Nes, E., Ryum N and Hunderi, O. On the zenar Drag, Acta Mater. 33 (1985) 11–22.
- [32] C.S. Smith, Introducation to grains, phases, and interfaces an interpretation of microstructures, Trans. AIME. 175 (1948) 15–51.
- [33] B. Hutchinson, Practical aspects of texture control in low carbon steels, Mater. Sci. Forum. 157–6 (1994) 1917–1928. https://doi.org/10.4028/www.scientific.net/msf.157-162.1917.
- [34] J.R. Porter, F.J. Humphreys, Nucleation of recrystallization at second-phase particles in deformed copper alloys, Met. Sci. 13 (1979) 83–88. https://doi.org/10.1179/msc.1979.13.2.83.

Chapter 3

Experimental Procedure

3

This chapter provides an outline of the chemical composition, their thermomechanical processing, techniques used for microstructural characterization, and mechanical property measurements in the present study are introduced and explained. A new methodology for partitioning the individual phases from different techniques EBSD and nanoindentation mapping is proposed to establish structure-property correlation both qualitatively, and quantitatively are described in detail.

3.1 Materials and their chemical composition

Four different types of steel sheets with varying C-Mn content were investigated in the present study. Their chemical composition and commercial-grade names are reported in Table 3.1. Alloy 1, which has a similar composition to Ultra-Low Carbon grade is used as a reference with the least carbon and only ferrite phase present in this present study. Whereas alloy 2 is similar to HSLA steels with microalloying element Nb, alloys 3 and alloy 4 have a similar composition to dual-phase steels DP600/DP800. All the commercial-grade steel sheets were received after 80% cold rolling from TATA STEEL Europe Ijmuiden, The Netherlands.

Table 3-1 Materials and their chemical composition

GRADE	С	Mn	Si	Nb	Cr
Alloy 1	0.002	1.28	0.22		
Alloy 2	0.06	1.32	< 0.008	0.0034	0.006
Alloy 3	0.09	1.65	0.28	< 0.001	0.057
Alloy 4	0.13	2.00	0.25	< 0.001	0.055

3.2 Thermomechanical processing:

The thermomechanical processing flow chart of AHSS alloys 2, alloy 3, and alloy 4 used in the investigation is shown in Figure 3-1. A cast ingot of 37mm is soaked at 1200 °C for 1 hr. Followed by hot rolling above austenite recrystallization temperature (Tnr). The Tnr temperatures of these steel sheets were determined by Gautam et al [1]. During hot rolling 37mm primary rolled industrial block was further hot rolled in six passes and reduced to a 6mm sheet, percentage rolling reduction in each pass is shown in Figure 3-1. Coiling was carried out at pearlite start temperature (600 °C) to obtain ferrite pearlite microstructures. Whereas alloy 1, was hot-rolled above Ar3 temperature, then air-cooling to ambient temperature. All the steel sheets alloy 1 to alloy 4 were further cold rolled to 80% reduction and sheets thickness was reduced from 6 mm to 1.2 mm as shown in Figure 3-1. Alloy 1 steel in the present study is used for references purpose to compare with alloy 2-4 which consists of ferrite-pearlite (HSS) steels. All the steel sheets were annealed at 300-500 °C to investigate static recovery and at 700 °C to study partial recrystallization. SEM, TEM and EBSD were used for microstructure and texture study. Mechanical properties were obtained from

mechanical testing using a micro Vickers hardness tester and nanoindentation which will be covered in depth in the parts that follow.

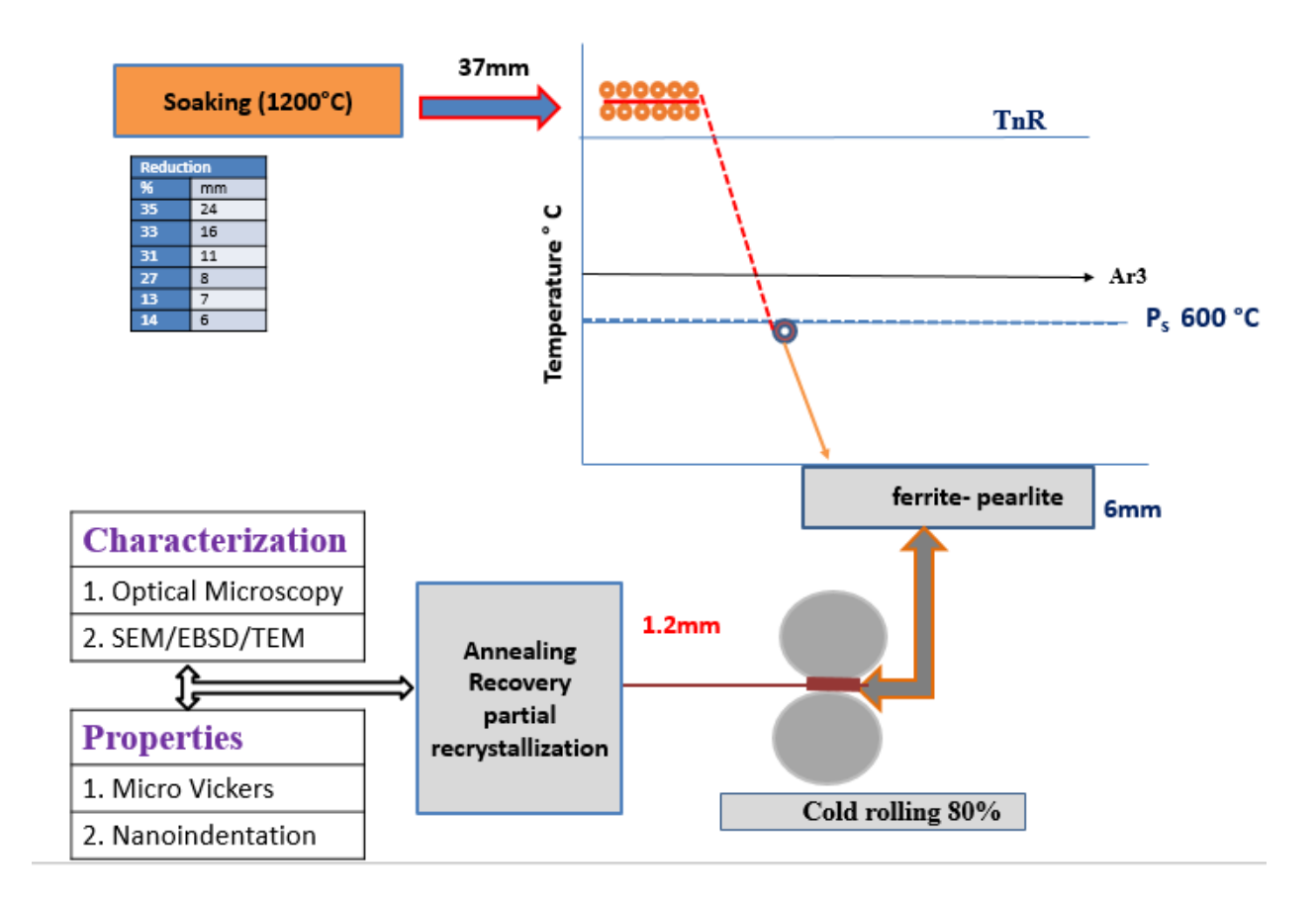


Figure 3-1 Schematic flow chat of materials thermomechanical processing and characterization

3.3 Annealing

Annealing treatment was carried out to investigate the static recovery and partial recrystallization behavior of all the 80% cold-rolled specimens. Small rectangular specimens measuring (LxW) 1.2x1 cm were cut from the center of the cold-rolled sheets.

3.3.1 Recovery annealing

Recovery annealing was carried out in a muffle furnace at 300 and 500 °C for different soaking times 30,60,120 and 300 min followed by furnace cooling. An experimental flow chart for the static recovery regime is shown in Figure 3-2.

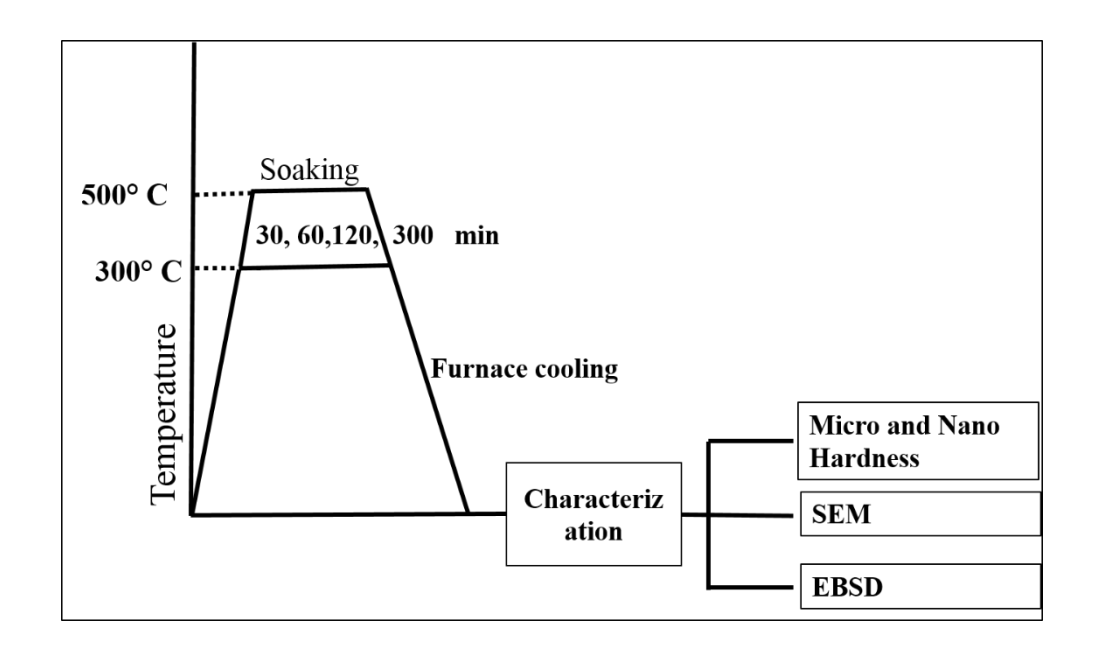


Figure 3-2 Schematic flow chat of static recovery

3.3.2 Partial recrystallized annealing

Partial recrystallized annealing was carried out in a salt bath furnace. The experimental flow chart is shown in Figure 3-3. Annealing was carried out at 700 °C for different soaking times of 10, 20, 30,60,90,120,150,180,300, 420 seconds followed by water quenching to study the partial recrystallization kinetics, morphological changes in microstructure and their associated changes in properties.

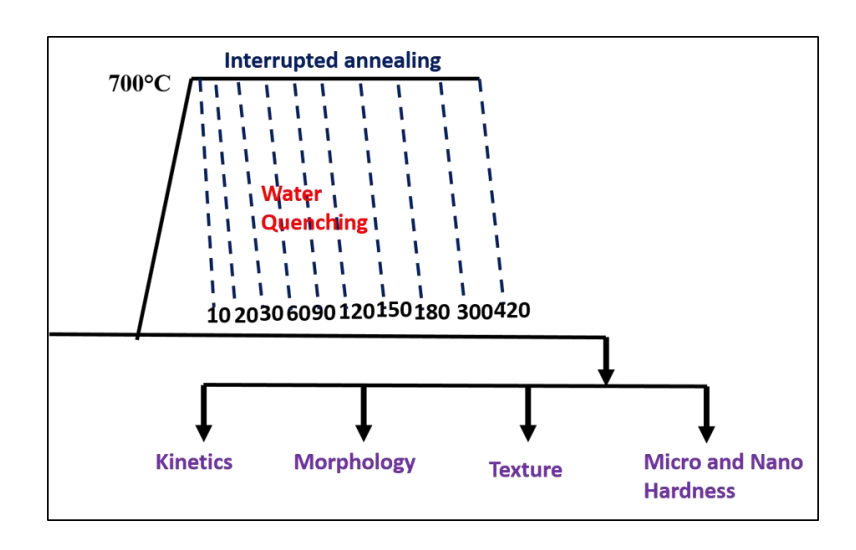


Figure 3-3 Schematic flow chat of partial recrystallization

3.4 Sample preparation

Sample preparation of hot-rolled, cold-rolled and annealed specimens is important for data measurement and analysis with different characterization techniques. The sample must be flat, debris-free and should free from strain-induced due to mechanical polishing for microstructure and property measurement. As part of sample preparation, mechanical polishing was carried out on SiC papers 400,600,800,1000,1200 followed by coarse alumina polishing. Vibratory polishing was carried out on fine colloidal silica of 50 nm for 8 hr. Microhardness and nanoindentation measurements were performed on these flat well-polished samples. In the present study the hardness, microstructural, and texture measurements were performed on the cross-section RD-ND direction, and TEM specimens were prepared from the surface of sheets in the RD-TD direction as shown in the schematic of Figure 3-4.

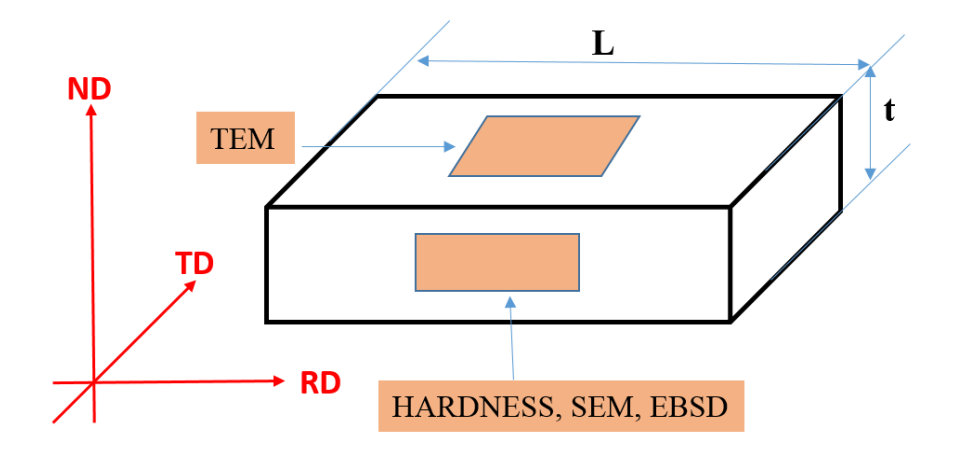


Figure 3-4 Schematic showing cross-section and surface used for measurement by different techniques like SEM, EBSD, HARDNESS, TEM

3.4.1 Sample preparation for EBSD

Sample preparation for EBSD includes standard preparation as per the SEM, followed by electro polished with standard A2 consisting of perchloric acid, butoxyethanol, and distilled water. Electro-polishing was carried out on struers electropol -5, the temperature of the electrolyte was maintained below 5 °C, operating at 25 volts for 10 seconds.

3.4.2 Sample preparation for TEM

TEM samples were mechanically thinned on Sic papers to a thickness of $50-80 \mu m$. The thinned sheets were punched to 3 mm disks and further thinned/polished to $30 \mu m$ by dimpling. Electron transparent regions were made in the dimpled region with a precision ion polishing system (PIPS) made of Gatan model 691 using ion energy (5 Kv) and ion current (40-50 mA)

3.5 Characterization

3.5.1 Optical and Scanning electron microscopy

Microstructural characterization after hot rolling was investigated under an optical microscope (OM). Whereas the cold rolling, annealing microstructures were investigated under the field emission scanning electron microscope (FE-SEM). All the samples were etched with 2% Nital for microstructural investigation under an optical microscope OM and FE-SEM.

An optical microscope (OM) is a light microscope, in the present study, Olympus optical microscope with a digital camera was utilized for distinguishing ferrite and pearlite. The Pearlite area fraction was determined using the images acquired by (OM).

3.5.2 Measurement of pearlite fraction

The area fraction of pearlite was determined using Image J software, as shown in Figure. 3-5. Optical micrographs show the presence of ferrite (white) and pearlite (grey) in Figure 3-5(a). A monochrome bitmap highlighting the pearlite by adjusting the threshold of contrast/brightness in image J software is shown in Figure 3-5(b). About 5-8 similar images in various places of the samples in the given condition were used to calculate the pearlite's area fraction.

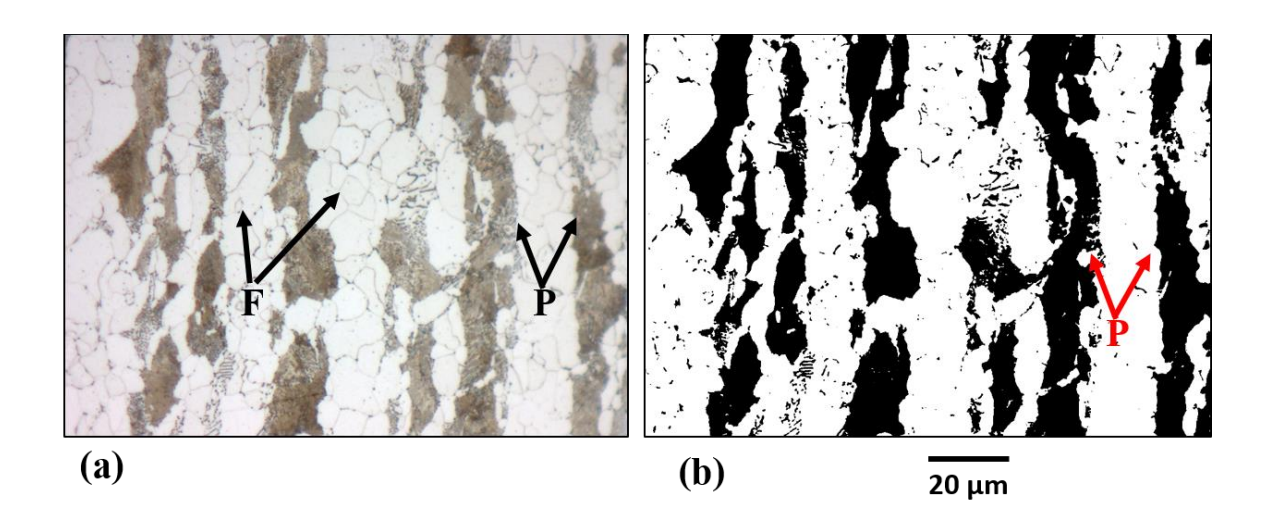


Figure 3-5 shows (a) optical micrograph with ferrite and pearlite band (b) monochrome bitmap highlighting pearlite

The FE-SEM allows the visualization of surfaces with high magnification and a large depth of focus. Unlike a light microscope, the FE-SEM views the specimen using electrons rather than white light. FE-SEM was carried out on FEI NOVA NANOSEM 450, with an accelerating

voltage of 20 kV, at a working distance of 10-15 mm. Microstructural and morphological changes in the ferrite and pearlite after cold rolling, recovery partial recrystallization annealing investigated.

3.5.3 Electron backscatter diffraction:

EBSD was performed on cold-rolled, recovery and partially annealed specimens for strain and texture measurements (crystallographic grain orientation of each grain). The working principle of the EBSD has been well discussed in [2–4]. EBSD measurements were performed on FEI NOVANANO–SEM 450 using an accelerating voltage of 20KV, spot size 5, aperture diameter 50 μ m and at a working distance 12-15 mm. The samples were positioned at 70 degrees toward the EBSD detector. Digiview 5 camera were used to acquire the Kikuchi (EBSD) patterns by hexagonal grid using OIM-TSL data collection software version 7. High-resolution EBSD was performed with a step size of 80 nm on 26 μ m x 26 μ m area where at least two to three pearlite bands were covered in each area. Whereas for texture measurement multiple measurements were performed with step size 0.12 μ m on 200 μ m x 200 μ m area.

Post-processing analysis was carried out using Version 7.2 of the OIM-analysis software. The EBSD misindexed data having less than 0.1 confidence index were excluded from further analysis.

3.5.4 Partitioning of recrystallized grains from EBSD.

Partitioning of recrystallized grains from deformed grains was carried out using kernel average misorientation (KAM) criteria as shown in Figure. 3-6. The image quality (IQ) map in Figure 3-6 (a) consists of recovered, recrystallized ferrite and pearlite bands. Corresponding KAM maps in Figure 3-6 (b), highlight recrystallized grain in (blue color) with misorientation in the

range of 0 - 1° range. The legend shows the quantified fraction of recrystallized grain (blue color) as 0.12%. It is well established that grains with misorientation of less than 1° are considered grain recrystallized elsewhere [5]. The grain higher than the 1° misorientation was considered as recovered ferrite or pearlite. This partition criterion was applied to the recrystallized samples to dissociate recrystallized grain from a recovered or deformed grain of ferrite and pearlite as shown in Figure 3-6 (b).

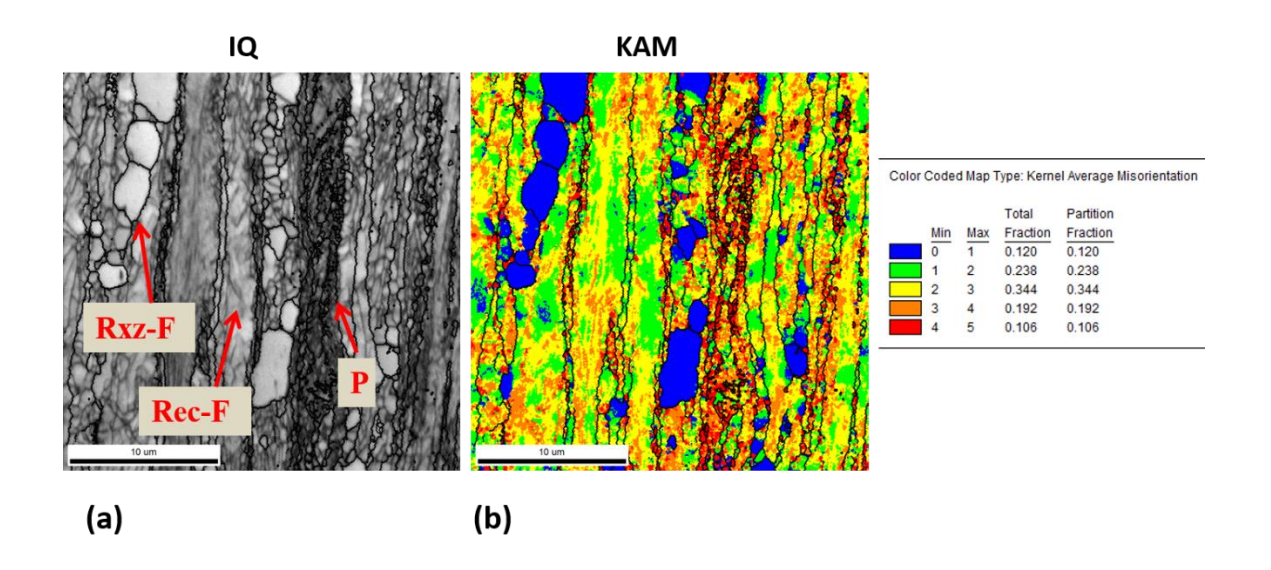


Figure 3-6 shows image quality map (a) consisting of recovered, recrystallized ferrite and pearlite band (b) KAM map (c).

3.5.5 Transmission electron microscopy (TEM)

Unlike the SEM, the electrons in the TEM are transmitted through the sample rather than being captured as secondary and backscattered electrons near the subsurface. The small wavelength of the electrons used in the TEM is the primary cause of the high spatial resolution. The thin foils were observed in TEM (JEOL 2100) operating at 200KV. TEM imaging specifically focused on ferrite and pearlite bands, to observe the structural changes under identical diffraction conditions along the Z = [001] zone axis.

3.6 Mechanical testing

The classical way of studying recovery and recrystallization induced softening is by indentation and tensile testing. In the present study, the indentation technique is employed to measure hardness. Hardness gives a quantified resistance measurement of a material to plastic deformation. Different hardness techniques are employed to study the properties at various length scales. In this study, two different indentation techniques used with different loads are discussed below.

3.6.1 Micro Vickers hardness

Micro Vickers hardness testing was performed on Tinius Olsen FH-006 series with a load of 500 gm and a dwell time of 20 seconds. In each sample, 9 indents were taken across the rolling direction on a flat well-polished surface. The area under the indent represents bulk hardness including multiple grains of both the phase i.e, ferrite and pearlite.

3.6.2 Nano Indentation.

Nanoindentation testing was performed using a commercially available nanoindenter, iMicro® with an InForce50 actuator from Nanomechanics Inc. (now KLA), Oak Ridge, USA. A high-speed mapping tool, NanoBlitz 3D+, was used to perform the mapping, with each indent taking less than a second to perform. Positioning the sample beneath the tip, contacting the surface, loading, unloading, and retracting are all part of the process. The usual Oliver and Pharr approach may be used to determine contact stiffness, hardness, and modulus from the load and depth data at each test spot [6,7]. For all experiments, a diamond Berkovich tip was employed since it allowed for the direct extraction of hardness and elastic modulus using the approach given by Oliver and Pharr. Indentation tests were carried out on flat, well-polished samples with final polishing in a colloidal silica suspension of 50 nm for 8 hours. Indents were performed to a depth not exceeding 100 nm with a spacing of 1µm, resulting in a spacing to

depth ratio of 10 on the recommendation of sudharshan Phani and Oliver in prior work [6]. Maps of $50X50\,\mu\text{m}^2$, with 2500 indents were performed on cold-rolled and recovery annealed samples. whereas in partially recrystallized condition maps of $75X75\,\mu\text{m}^2$ area, with 5625 indents were performed to have a statistically higher number of recrystallized grains. The findings of continuous strain rate testing (0.2 s-1) on fused silica were utilized to determine load frame stiffness and tip area calibration. For these experiments, the contact stiffness was measured continuously as a function of depth using a phase lock amplifier with a frequency of 100 Hz and a displacement amplitude of 2 nm.

In the present study, to understand microstructure and property correlation nanoindentation and SEM imaging were performed in the same region as shown in Figure 3-7. SEM micrographs with nanoindentation imprints as in Figure 3-7 (a) show the presence of both ferrite and pearlite phases. The corresponding hardness map was obtained by nanoindentation mapping as in Figure 3-7(b). An excellent spatial (qualitative) correlation has been observed in the microstructure and a hardness map was observed, also the difference in individual phase features of ferrite and pearlite is observed.

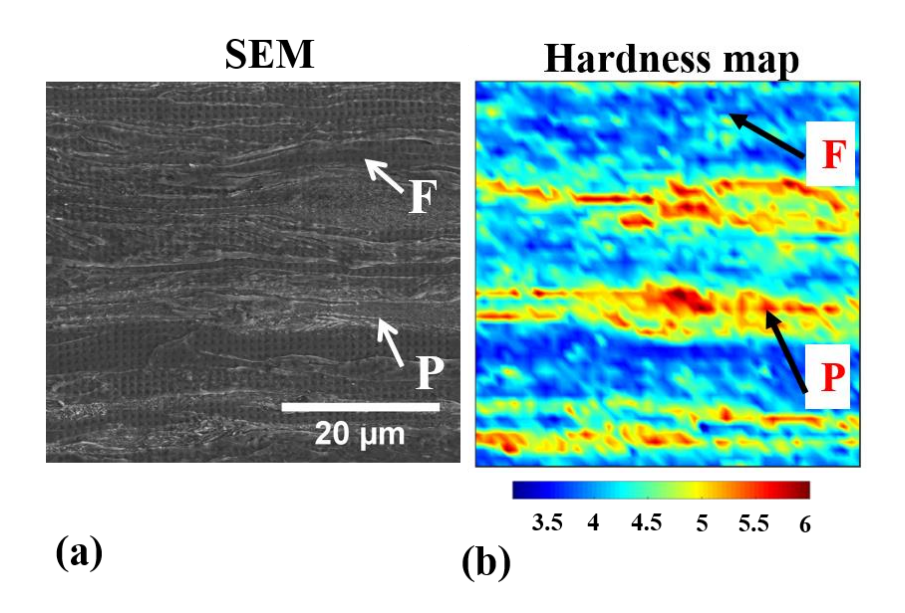


Figure 3-7 Showing (a) SEM, (b) hardness map from nanoindentation

3.7 Deconvolution of data

To determine the intrinsic mechanical characteristics directly/microstructural information in terms of hardness, elastic modulus and KAM values for individual phase ferrite-pearlite, a k-means clustering algorithm was used [8]. The large data sets obtained from mapping were deconvoluted using the k-means clustering algorithm to obtain a mechanical phase map as detailed elsewhere[6,7]. The main purpose of k-means is to divide a set of 'n' observations into a set of 'k' groups. K-means is an iterative refining strategy that starts with k cluster canters by changing cluster canters to a new place at random and minimizing the intra-cluster sum of squares of distances in each iteration. When it is no longer possible to reduce intra-cluster distances, the iterative procedure converges, dividing the data into a preset number of clusters. The cluster into which the data must be binned can be determined by repeatedly running the method for various numbers of clusters and identifying the best number via error minimization, or by having preexisting knowledge of the number of phases present in the mapped region. Because the method partitions the data in such a way that data points within the same cluster

are more similar to those in other clusters, it is expected that each data point will be more similar to those in other clusters. Because the technique splits the data so that data points inside a cluster are more similar than data points in other clusters, each cluster should reflect a separate phase/feature in the spatial map. As the algorithm splits the data so that data points in the same cluster are more similar than data points in other clusters, each cluster should reflect a separate phase/feature in the spatial map. The mean and standard deviation of the data points in each cluster can be utilized as a quantitative measure of the relevant phase's property once they've been clustered.

3.7.1 Deconvolution of hardness data

Figure. 3-8 (a) shows SEM micrograph consisting of two phase ferrite and pearlite and Figure 3-8(b) confirms variation in hardness among ferrite and pearlite. Nanoindentation mapping hardness data were divided into 2 bins to cluster the data of ferrite (blue), and pearlite (red) color as shown in Figure 3-8 (c). It was observed that a good spatial correlation exists between individual phase's ferrite, pearlite from SEM microstructure, hardness map and deconvolution phase map as in Figure 3-8 (a-c). In each phase, the mean and standard deviation of each data point was calculated to correspond to the property of each phase. Probability distribution function curves for ferrite and pearlite were drawn using the average mean and standard deviation of each phase as by Gaussian distribution assuming the curve to be Gaussian [9]. Histograms of hardness were constructed for both ferrite and pearlite as shown in Figure 3-8(d). The center of the peak represents the average hardness of the respective phases and the area under the peak represents the area fraction of the respective phases. The hardness changes after cold rolled, recovery and partial recrystallization annealing are qualitatively and quantitatively extracted similarly in the thesis.

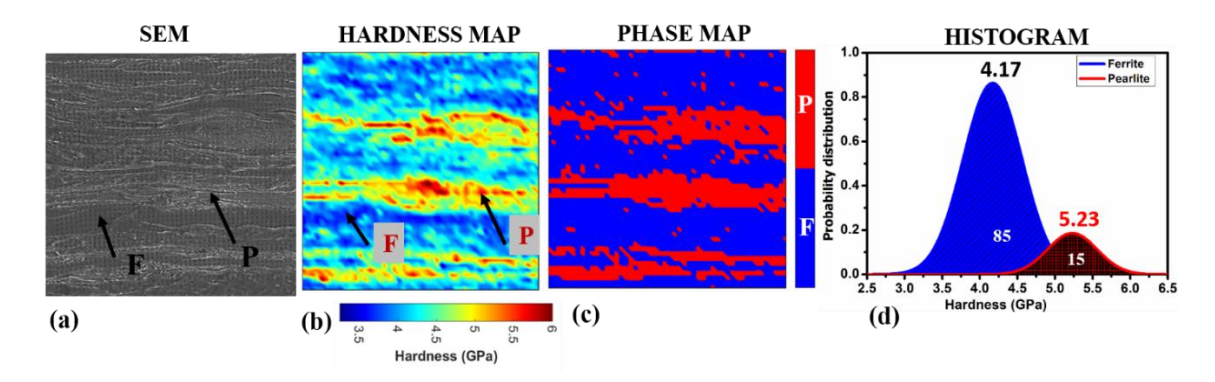


Figure 3-8 Showing (a) SEM, (b) hardness map from nanoindentation (c) mechanical (deconvoluted) phase map showing binned regions of ferrite, pearlite and (d) hardness histogram of individual phase features.

3.7.2 Deconvolution of EBSD data

Due to the similarity in the crystal structure of ferrite and perarlitic ferrite in pearlite, the partitioning of ferrite and pearlite is not straightforward from EBSD data. In multiphase steels ferrite-martensite, IQ and KAM have been successfully utilized in the partitioning of bainite and martensite from ferrite due to different lattice distortion which results in different IQ values[10,11]. EBSD Kikuchi bands of martensite will have deformed arrangements and lower IQ due to crystalline defects such as subgrain, grain boundary, high dislocation density, lattice strain, and increased carbon content deform the lattice [12]. As identification/partition of the phases is dependent upon the resolution of IQ images, researchers depended upon image correlations studies to get good outcomes. One method is to filter the original IQ image and generate multiple Gaussian distributions of the IQ values using a threshold IQ value. [13]. However, when using a self-defined threshold number to divide a continuous multi-peak distribution into two groups (ferrite and martensite), this approach has proved to be erroneous. With some success, the link between IQ levels and martensitic constituents has been employed [14]. They did not, however, give quantitative criteria for determining whether pixels belong to ferrite, bainite, martensite, or high-angle grain boundaries, making the technique very

operator-dependent [15]. Math novel and Stuart write et al. [16] have recommended a kernel-based method for more accurate measurement of phase discrimination in ferrite and martensite with minimum error relative to manual error.

Due to the limitation in partition/identification and quantification of the pixels of individual phases and many of them or operator dependent in this work we utilize both image-based correlation techniques and new machine learning clustering algorithms k-means to the partitioning of ferrite and pearlite based on the pixel information and quantify the misorientation distribution of ferrite and pearlite.

For deconvolution of ferrite and pearlite from EBSD maps, SEM and EBSD were performed in a similar region for image correlation. The data obtained from the EBSD map was used to partition ferrite and pearlite regions based on the IQ of the diffraction pattern and KAM as reported in [17]. Zaffrer et al [18] have reported the advantages of KAM based approach as more reliable than other misorientation methods. As KAM based misorientation method calculates all the average misorientation between the center of the pixel and its neighboring pixel. In the present study, KAM values were calculated with 5th neighbor and the threshold was set 5°. The step size of each map was 80 nm with a hexagonal grid. We measured the average KAM with 4th ot 6th neighbor and did not see many variations in KAM values, the intermediate 5th neighbor was chosen. Also to improve the sensitivity of measurement higher order neighbor was chosen i.e, 5th neighbor. By adopting 5th neighbor this we measure the orientation variation about 400 nm which is good in terms of spatial resolution of the measured EBSD system. Utilizing KAM has dual advantage in this work, first, it is the good method to discriminate phase's accurately with threshold value and reduce the human error. Second is,

KAM is also used to invest age recovery and recrystallization to give a direct measure of structural and substructure changes cause due the above annealing phenomena.

The qualitative correlation of ferrite and pearlite from SEM, IQ and KAM is shown in Figure.3-9. SEM micrograph in Figure 3-9 (a) shows ferrite (dark grey) and pearlite (white grey), IQ map in Figure 3-9 (b-c) shows higher IQ and lower KAM values correspond to ferrite and lower IQ and higher KAM corresponds to pearlite. It was observed that a good spatial correlation exists between the individual phase's ferrite and pearlite in SEM with IQ and KAM maps in Figure 3-9(a-c). The KAM map also revealed that KAM values were greater around grain boundaries, due to its lower IQ in these areas.

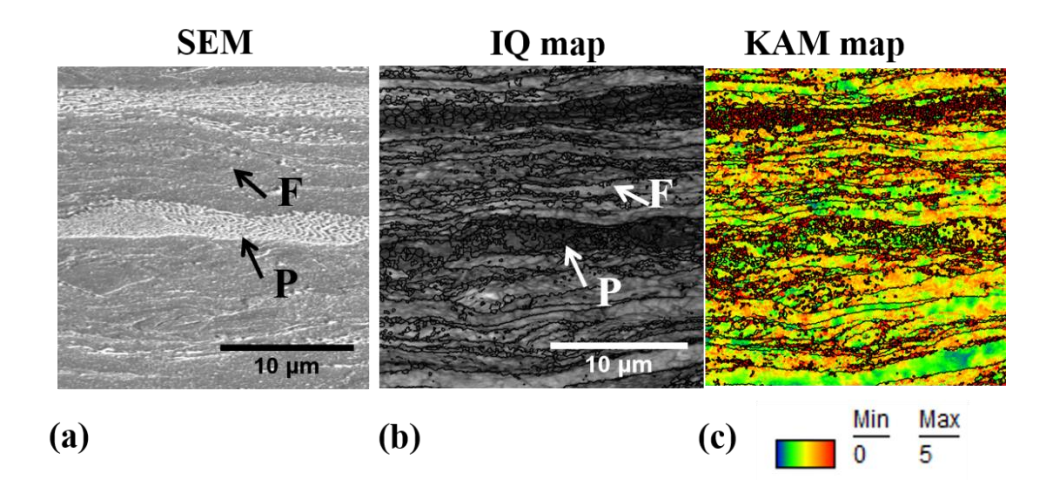


Figure 3-9 shows ferrite and pearlite obtained from (a) SEM and EBSD (b) IQ map, (c) KAM map Ferrite –F and pearlite –P

To deconvolute ferrite and pearlite based on IQ and quantify the average misorientation KAM. Each pixel information such as X, Y position, their corresponding IQ and KAM values were extracted from EBSD maps in an excel sheet. K-means clustering algorithm was used to partition out ferrite and pearlite based on IQ with each pixel information by using mat lab.

Deconvolution of ferrite-pearlite their correlation with SEM micrograph and quantification of KAM values have been shown in Figure 3-10. SEM micrograph shows ferrite and pearlite as in Figure 3-10(a). IQ map shows higher IQ corresponds to ferrite and lower IQ to pearlite as in Figure 3-10(b). IQ data was divided into three bins ferrite (blue) and pearlite (red) and green (grain boundaries) shown in Figure 3-10(c). It was observed that a good spatial correlation exists between ferrite and pearlite in SEM, IQ and deconvolute maps in Figure 3-10(a-c). The mean and standard deviation of each pixel point was obtained in each phase (bin) corresponding to the KAM value of each phase. Probability distribution function curves for ferrite and pearlite were drawn using the mean and standard deviation of individual phases. Histograms of KAM were constructed for both ferrite and pearlite as shown in Figure 3-10(d). The center of the peak represents the average KAM of the ferrite and pearlite. The KAM changes after cold rolled, recovery and partial recrystallization annealing are qualitatively and quantitatively extracted similarly in the thesis.

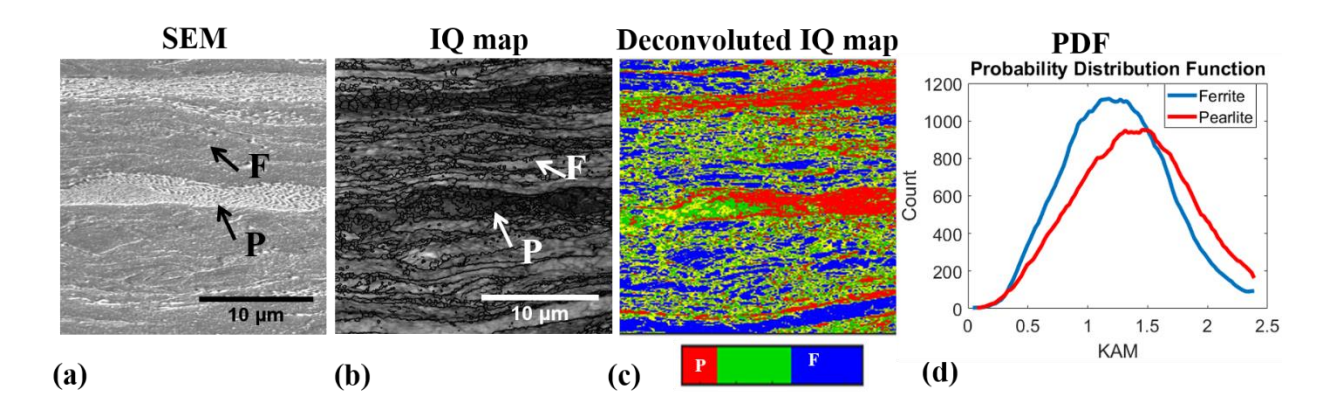


Figure 3-10 Figure. 3.10 (a) SEM micrograph, (b) hardness map, (c) deconvoluted map and (d) average KAM of individual phase, ferrite –F and pearlite –P

References

[1] J. Gautam, A. Miroux, J. Moerman, C. Barbatti, P. Van Liempt, L.A.I. Kestens, Determination of the non-recrystallisation temperature (Tnr) of austenite in high strength C-Mn steels, Mater.

- Sci. Forum. 706–709 (2012) 2722–2727. https://doi.org/10.4028/www.scientific.net/MSF.706-709.2722.
- [2] S. Suwas, R.K. Ray, R.K.R. Satyam Suwas, Crystallographic Texture of Materials, Springer US, 2014. doi:10.1007/978-1-4471-6314-5
- [3] Schwartz, A. J., Kumar, M., & Adams, B. L. (Eds.). (2000). Electron Backscatter Diffraction in Materials Science. doi:10.1007/978-1-4757-3205-4 DOI 10.1007/978-0-387-88136-2
- [4] E.R. Davies, Introduction to texture analysis, 2008. https://doi.org/10.1142/9781848161160_0001.
- [5] Wright, S., Nowell, M., & Field, D. (2011). A Review of Strain Analysis Using Electron Backscatter Diffraction. Microscopy and Microanalysis, 17(3), 316-329. doi:10.1017/S1431927611000055
- [6] P. Sudharshan Phani, W.C. Oliver, A critical assessment of the effect of indentation spacing on the measurement of hardness and modulus using instrumented indentation testing, Mater. Des. 164 (2019) 1–10. https://doi.org/10.1016/j.matdes.2018.107563.
- [7] B. Vignesh, W.C. Oliver, G.S. Kumar, P.S. Phani, Critical assessment of high speed nanoindentation mapping technique and data deconvolution on thermal barrier coatings, Mater. Des. 181 (2019). https://doi.org/10.1016/j.matdes.2019.108084.
- [8] S. Journal, R. Statistical, S. Series, C.A. Statistics, Algorithm AS 136: A K-Means Clustering Algorithm Author (s): J. A. Hartigan and M. A. Wong Published by: Blackwell Publishing for the Royal Statistical Society Stable URL: http://www.jstor.org/stable/2346830, 28 (2009) 100–108.
- [9] J.J. Roa, P. Sudharshan Phani, W.C. Oliver, L. Llanes, Mapping of mechanical properties at microstructural length scale in WC-Co cemented carbides: Assessment of hardness and elastic modulus by means of high speed massive nanoindentation and statistical analysis, Int. J. Refract. Met. Hard Mater. 75 (2018) 211–217. https://doi.org/10.1016/j.ijrmhm.2018.04.019.
- [10] M. Calcagnotto, Y. Adachi, D. Ponge, D. Raabe, Deformation and fracture mechanisms in fineand ultrafine-grained ferrite/martensite dual-phase steels and the effect of aging, Acta Mater. 59 (2011) 658–670. https://doi.org/10.1016/j.actamat.2010.10.002.
- [11] M. Calcagnotto, D. Ponge, E. Demir, D. Raabe, Orientation gradients and geometrically

- necessary dislocations in ultrafine grained dual-phase steels studied by 2D and 3D EBSD, Mater. Sci. Eng. A. 527 (2010) 2738–2746. https://doi.org/10.1016/j.msea.2010.01.004.
- [12] E.A. Ariza-Echeverri, M. Masoumi, A.S. Nishikawa, D.H. Mesa, A.E. Marquez-Rossy, A.P. Tschiptschin, Development of a new generation of quench and partitioning steels: Influence of processing parameters on texture, nanoindentation, and mechanical properties, Mater. Des. 186 (2020). https://doi.org/10.1016/j.matdes.2019.108329.
- [13] S.H. Choi, E.Y. Kim, W. Woo, S.H. Han, J.H. Kwak, The effect of crystallographic orientation on the micromechanical deformation and failure behaviors of DP980 steel during uniaxial tension, Int. J. Plast. 45 (2013) 85–102. https://doi.org/10.1016/j.ijplas.2012.11.013.
- [14] M.J. Santofimia, R.H. Petrov, L. Zhao, J. Sietsma, Microstructural analysis of martensite constituents in quenching and partitioning steels, Mater. Charact. 92 (2014) 91–95. https://doi.org/10.1016/j.matchar.2014.03.003.
- [15] M. De Meyer, L. Kestens, B.C. De Cooman, Texture development in cold rolled and annealed C-Mn-Si and C-Mn-Al-Si TRIP steels, Mater. Sci. Technol. 17 (2001) 1353–1359. https://doi.org/10.1179/026708301101509557.
- [16] S.I. Wright, M.M. Nowell, EBSD image quality mapping, Microsc. Microanal. 12 (2006) 72–84. https://doi.org/10.1017/S1431927606060090.
- [17] J. Wu, P.J. Wray, C.I. Garcia, M. Hua, A.J. Deardo, Image quality analysis: A new method of characterizing microstructures, ISIJ Int. 45 (2005) 254–262. https://doi.org/10.2355/isijinternational.45.254.
- [18] S. Zaefferer, P. Romano, F. Friedel, EBSD as a tool to identify and quantify bainite and ferrite in low-alloyed Al-TRIP steels, J. Microsc. 230 (2008) 499–508. https://doi.org/10.1111/j.1365-2818.2008.02010.x.

Chapter 4

Microstructure and properties evolution in Cold Rolled High Strength Steels

4

The present study investigates, microstructure and mechanical properties evolution in different grades of AHSS with varying pearlite fractions in comparison with single phase ULC steels after 80% cold rolling. High-resolution Nanoindentation mapping was performed at a micrometer length scale to gain more insights into the hardness response of individual phases. Kernel average misorientation analysis was performed to correlate misorientation with the hardness of individual phases. This chapter highlights the results on the role of pearlite on microstructure and properties evolution.

4.1 Introduction

Demand for high-strength steels (HSS) such as HSLA, DP, and TRIP steels is rising in the automotive sector, mostly to reduce the weight of various vehicle components, consequently improving fuel economy and lowering CO2 emissions[1–4]. It is commonly known that DP and TRIP steels offer an excellent balance of mechanical properties such as high strength and ductility The second phase morphology of martensite, distribution and area fraction plays a key role in determining the strength and ductility in DP and TRIP steels[1–4]. These properties are intern decided by the chemical composition, thermomechanical properties and resulting

microstructure of these steels. However, such information on cold rolled HSS steels with varying pearlite fraction, its distribution, and area fraction in ferrite matrix is not well investigated. For the design and development of new AHSS the knowledge of microstructure is paramount.

Low carbon steels consisting of a single ferrite phase, the microstructural and texture evolution after various cold reductions have been well investigated [5–8]. Higher cold rolling reduction enhances the amount of distortion and defect density in the material. In IF steels, homogeneous deformation enhances the texture formation [5,8,9].

Unlike IF steels, High strength steels have higher carbon which leads to a composite microstructure of ferrite and pearlite, whereas pearlite is a combination of ferrite and cementite. Rabee et al [10] have reported that the characterization of pearlite is important as it contributes to the mechanical property of the material. Felipe et al[11] It is well reported that homogeneous deformation during cold rolling causes heterogeneous distribution in ferrite and pearlite phases and varies the mechanical properties at the micrometer length scale. Which subsequently leads to non-uniform deformation and causes weakening of deformation texture [9]. In the case of ferrite-pearlite consisting steels as reported in [12], showed pearlite phases have higher hardness compared to ferrite phases showing heterogeneity in the strength level of the two phases. As ferrite is softer and ductile it accommodates more strain than the pearlite phase. Pearlitic ferrite accommodates strain and cementite remains non-deformed either it fractures or rotates [11]. Heterogeneity is mainly caused due to differences in microstructure, crystal structure, or compositional heterogeneity [13]. In DP steels, heterogeneity in mechanical behavior was well investigated and compared with two different DP800 grade sheets of steel, it was observed that two different sheets of steel showed similar mechanical behavior,

however, the individual phases showed different strength levels[14] (dp steels paper). Experimentally, Kernel average Misorientation (KAM) obtained from EBSD is used to characterize heterogeneity through strain localization [15,16]. Shen et al. [17] reported that a spatial (qualitative) correlation between misorientation and hardness was obtained from nanoindentation in nickel-based superalloys. However, such information in different grades of high strength steels like HSLA, DP steels consisting of composite ferrite pearlite microstructure after cold rolling is not well investigated. Heterogeneity in microstructure complicates understanding the behavior after cold rolling in terms of deformation mechanisms, microstructural, texture evolution, mechanical properties in individual phases

For any product design, the overall properties of a material are determined by microstructural constituent phases, their volume fraction, size, distribution of phases, and properties of individual phase's constituents [18].

4.2 Experimental procedure:

4.2.1 Chemical composition and processing

Four different steel sheets with varying mainly C-Mn compositions were used in this study and their chemical compositions are reported in Table 1. Alloy 1 which has a similar composition to Ultra-Low Carbon grade is used as a reference with the least carbon and only ferrite phase present in this present study. Whereas alloy 2 is similar to HSLA steels and alloys 3/4 have a similar composition to dual-phase steels. In alloys, 2-4 hot rolling was carried out above the austenite recrystallization temperature followed by coiling at pearlite start temperature to have ferrite- pearlite microstructure [19]. The area fraction of the pearlite has been quantified from hot rolled images using Image – J software and the changes in pearlite area fraction with varying amount of carbon has been reported in Table 1. Hot rolled steel sheets of 6 mm were

subsequently cold rolled to 80% reduction having 1.2 mm thickness. The hardness in the cold-rolled state due to varying steel chemistry is also reported in Table 4.1.

Small steel specimens (Length=1.2cm and Width-1 cm) were cut from the center of the cold rolled sheets. Mechanical polishing was carried out on SiC papers, followed by coarse alumina polishing and vibratory polishing with fine colloidal silica of 50 nm for 8 hr.

4.2.2 Characterization and mechanical testing

Microhardness and nanoindentation measurements were performed on these well-polished samples. Tenuis Olsen FH 006 series machine was used for micro Vickers hardness measurement on all the cold rolled and annealed specimens with a Load of 500 gram and 20 s dwell time. Nanoindentation mapping was performed using a commercially available nanoindenter iMicro® with an InForce50 actuator from Nanomechanics Inc. (now KLA Corporation), Oak Ridge, USA. Multiple large indentation maps with 2500 indents per map on a 50 μm x 50 μm area were collected using the NanoBlitz3D high-speed mapping technique. Indentation spacing of 1 μm was maintained and the load was changed such that the indentation depth was 100 nm or lower, which results in a minimum spacing to depth ratio of 10, as per the recommendations of Sudharshan Phani et al.[20]. Note: all the microstructural examinations (SEM-EBSD) and mechanical properties in terms of hardness were investigated on thickness direction RD-ND in this study.

High-resolution EBSD mapping was performed with FEI NOVA NANOSEM 450, with a voltage 20 KV, a working distance 15mm and a step size 80 nm on 26 μ m x 26 μ m area of cold-rolled and recovery annealed samples. Kernel average misorientation maps were extracted from TSL OIM analysis software to see lattice imperfection stored (strain localization) in ferrite and pearlite phases.

For qualitative/quantitative correlation of microstructure with properties in individual phase feature were deconvoluted as reported in chapter 3. Microstructural information was obtained from KAM map and properties were obtained from nanoindentation maps. Partition of ferrite and pearlite from EBSD was carried out based on IQ maps as reported in [21]. KAM values of ferrite and pearlite were extracted and their corresponding distribution was plotted for quantitative information. Whereas, the hardness of ferrite and pearlite were deconvoluted from nanoindentation data in terms of hardness for each constitutive phase. A clustering algorithm called k-means was used to identify the regions with distinct mechanical properties as reported by [22,23].

Table 4-1 Chemical composition, the area fraction of pearlite after hot rolling

GRADE	С	Mn	Nb	Ferrite	Pearlite
				Area	Area
				fraction	fraction (%)
				(%)	
Alloy 1	0.002	1.28		100	
Alloy 2	0.06	1.32	0.0034	93.4± 1.5	7.6 ± 0.5
Alloy 3	0.09	1.65	< 0.001	70.3 ± 6.2	29.6± 6.2
Alloy 4	0.13	2.00	< 0.001	66.5± 4.6	33.5± 4.6

4.3 Results

4.3.1 Microstructure evolution after 80% cold rolling

Microstructural evolution after hot rolling is shown in Figure 4-1. It was observed that alloy 1 consists of only single ferrite (white) with coarse grains as shown in Figure 4.1(a). Whereas alloys 2-4, consists of both ferrite (white color) and pearlite (dark color) as shown in Figure 4-

1(b-d). Alloy 4 shows a higher fraction of pearlite in comparison to alloy 3 and alloy 2 as shown in Figure. 4-1(b-d) and as confirmed from Table 4.1. In alloy 2 as in Figure. 4.1, (b) pearlite colony appears to be in blocks hereafter it will be referred to as non-banded. In alloy 3/4 the pearlite is distributed in the form of a band. Where the band appears to be continuous across the sheet thickness, aligned in the rolling direction. It was observed that alloys 1-4, show differences in ferrite grain size, pearlite area fraction and its distribution the reasons for the same will be discussed in detail in the discussion section.

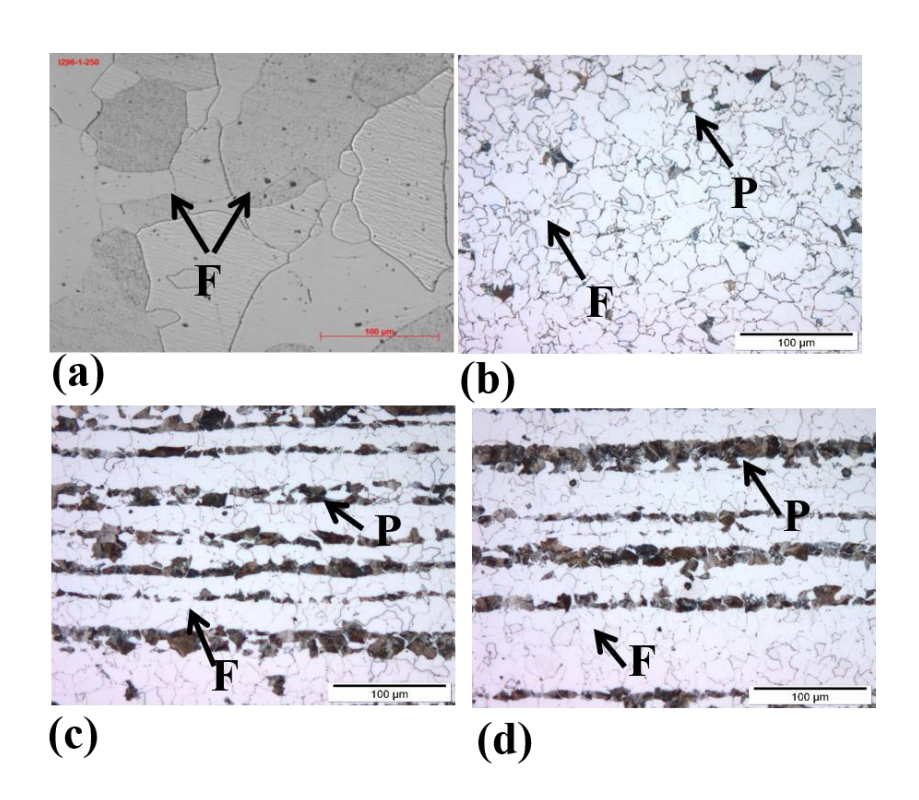


Figure 4-1 Hot rolled microstructures consisting of only ferrite in (a) Alloy 1 and ferrite pearlite phases, (b) Alloy 2, (c) Alloy 3 (d) Alloy 4

4.3.2 Microstructure evolution after 80% cold rolling

Cold rolled microstructures of all the four alloys are shown in Figure. 4-2, pancaked grains morphology has been observed in all the microstructures of four steel specimens. Alloy 1, steel consists of a single ferrite phase (grey) as indicated and shown in Figure. 4-2(a). In alloy 2-4,

the microstructure consists of two-phase, ferrite (dark grey) and pearlite (light grey) as in Figure. 4-2(b-d). In alloy 2-4 resulted in distinct differences in the microstructure, in terms of pearlite distribution, area fraction from hot rolling is still retained. In addition to that cold rolling resulted in differences in the morphology of cementite in pearlite. In alloy 2 as in Figure. 4-2(b) morphology of cementite in the pearlite colony is fragmented. In alloy 3/4 the pearlite is distributed in the form of a band and the morphology of cementite is lamellar.

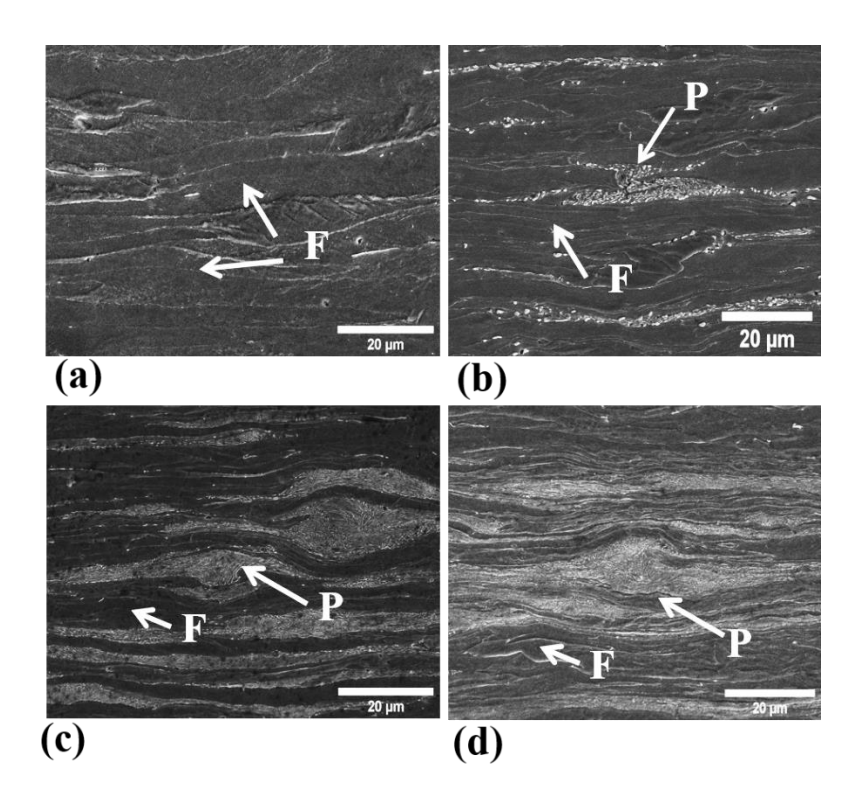


Figure 4-2 Cold rolled microstructures with ferrite (a) ULC and ferrite pearlite phases, (b) HSLA, (c) DP600 (d) DP600

4.3.3 KAM evolution after Cold rolling

Kernel average misorientation (KAM) criteria were used to study the evolution of misorientation and strain localization among single ferrite and ferrite pearlite structures in all the 80% cold rolled samples as shown in Figure 4-3. IQ combined with KAM maps obtained

from high-resolution EBSD mapping was used to distinguish the ferrite in alloy 1, ferrite-pearlite in alloy 2-4. The greyscale, image quality maps and their corresponding color coded KAM maps of ferrite in alloy 1 and ferrite-pearlite in alloy 2-4 are shown in Figure 4-3. KAM map shows the average misorientation of points with respect 5th nearest neighbor and a maximum of 5° misorientation. The color blue indicates a defect free region in the microstructure with misorientation of less than 1°, green color 1-2°, and yellow color 2-3°, and orange 3-4°, red 4-5°. A Higher KAM value represents the structure with higher defects and lattice distortion [21].

In cold rolled conditions, Figure 4-3(a) shows an image quality (IQ) map of only ferrite in alloy 1. The corresponding KAM map shows ferrite with misorientation 2-4° with green, yellow and orange colors. In alloy 2-4 consisting of both ferrite-pearlite microstructure as in Figure 4-3(b-d) shows both higher and low IQ. The lower IQ (dark color) represents pearlite and the higher IQ represents ferrite. The corresponding KAM map shows pearlite in red color having higher misorientation in the range of 4-5°. Whereas in the ferrite phase with higher IQ, the KAM map shows misorientation in the range of 2-4° in green, yellow and orange colors. In ferrite, it was observed that the misorientation spread (orientation gradient) inside and at the ferrite-ferrite grain boundary represented in yellow and orange colors in all the alloys 1-4. In alloys 2-4, it was observed that misorientation spread was higher at the ferrite/pearlite interfaces than inside the ferrite grains. In pearlite also observed the presence of orientation gradient.

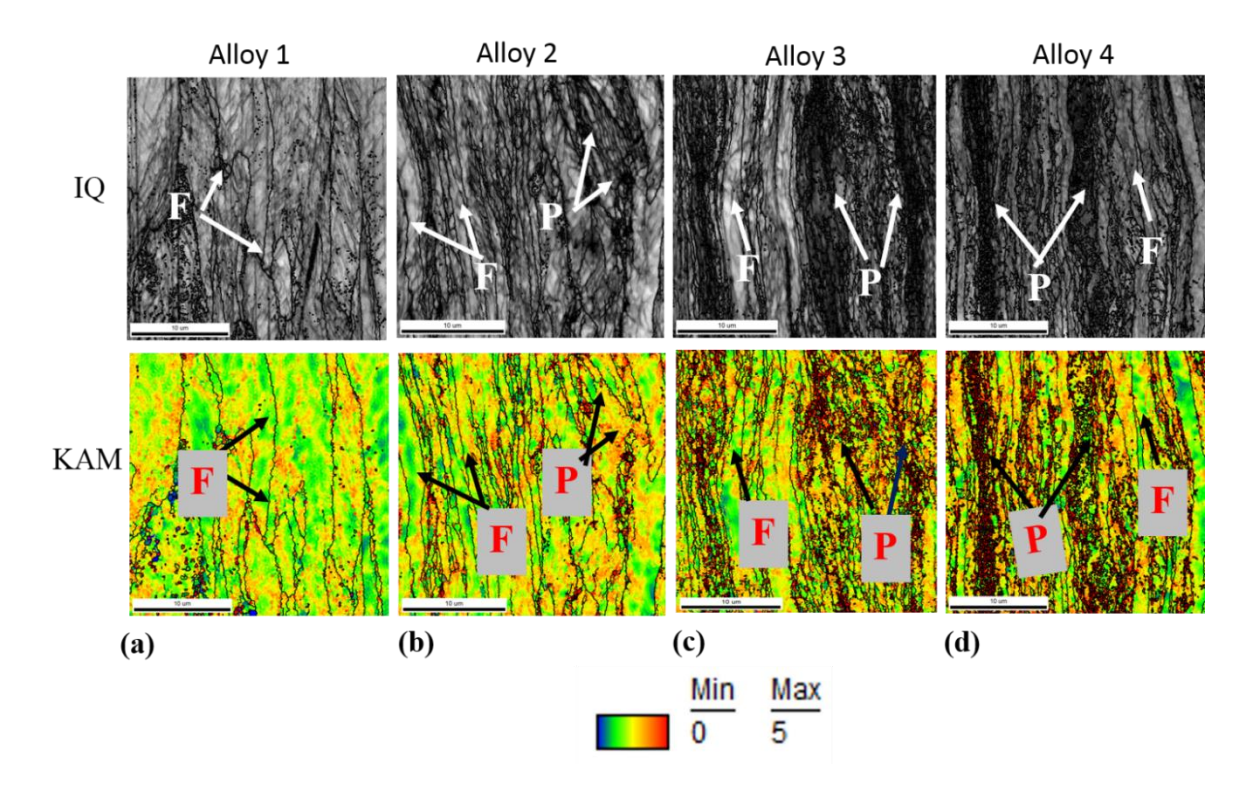


Figure 4-3 IQ and Kernel average misorientation (KAM) showing the evolution of local grain misorientation and strain distribution in cold rolled microstructures with ferrite in (a) Alloy 1 and ferrite-pearlite phases, (b) Alloy 2 (c) Alloy 3 (d) Alloy 4

4.3.4 Deconvolution of ferrite and pearlite after 80% Cold rolling

To extract the microstructural information of individual phase's both qualitatively and quantitatively, IQ maps obtained from EBSD were used to deconvolute the ferrite and pearlite as discussed in chapter 3. IQ and their corresponding deconvoluted map obtained from the IQ in all the 4 alloys is shown in Figure 4-4. In alloy 1, which consisted of a single ferrite phase with higher IQ, the corresponding deconvoluted map shows only ferrite (blue color) as shown in Figure 4-4(a). Whereas in alloys 2-4, which consisted of ferrite higher IQ and pearlite lower IQ (dark region) in IQ maps. The corresponding deconvoluted map shows, ferrite in (blue color) and pearlite (red color) as shown in Figure 4-4 (b-d). It was observed that a good spatial correlation exists in ferrite and pearlite by deconvolution when compared with IQ maps in alloys 2-4.

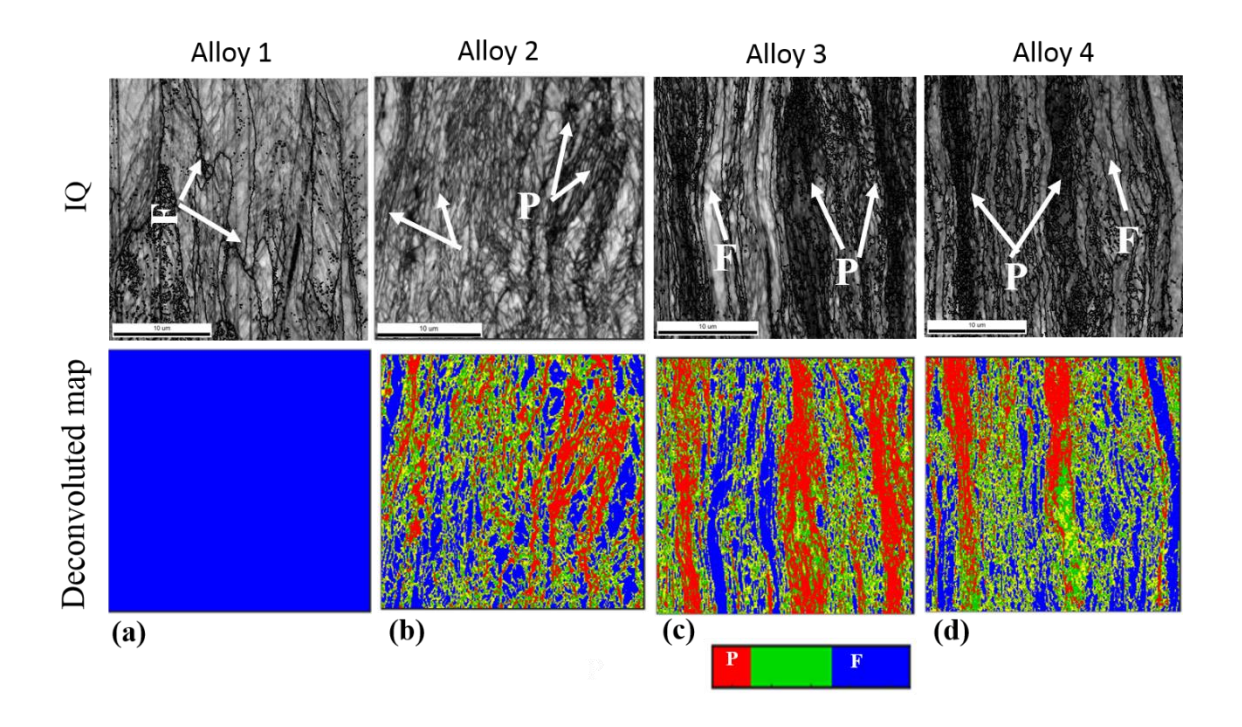


Figure 4-4 IQ and deconvoluted maps of cold rolled microstructures with ferrite in (a) Alloy 1 and ferrite-pearlite phases, (b) Alloy 2 (c) Alloy 3 (d) Alloy 4 banded.

4.3.5 KAM distribution of ferrite and pearlite

After deconvolution of ferrite and pearlite from IQ maps the KAM values of individual phases of ferrite and pearlite were extracted and plotted in distribution to see the microstructural changes in all alloys as shown in 4-5. In the case of ferrite, as shown in Figure 4-5(a), the lowest average KAM value was observed in alloy 1. Whereas in alloy 2-4 KAM value slightly increases and shifts peak towards right side i.e. higher KAM values in comparison to alloy 1. Whereas in the case of pearlite as shown in Figure 4-5(b), KAM distribution follows similar behavior in all the pearlite consisting of alloys 2-4 and did not show many differences in average KAM values.

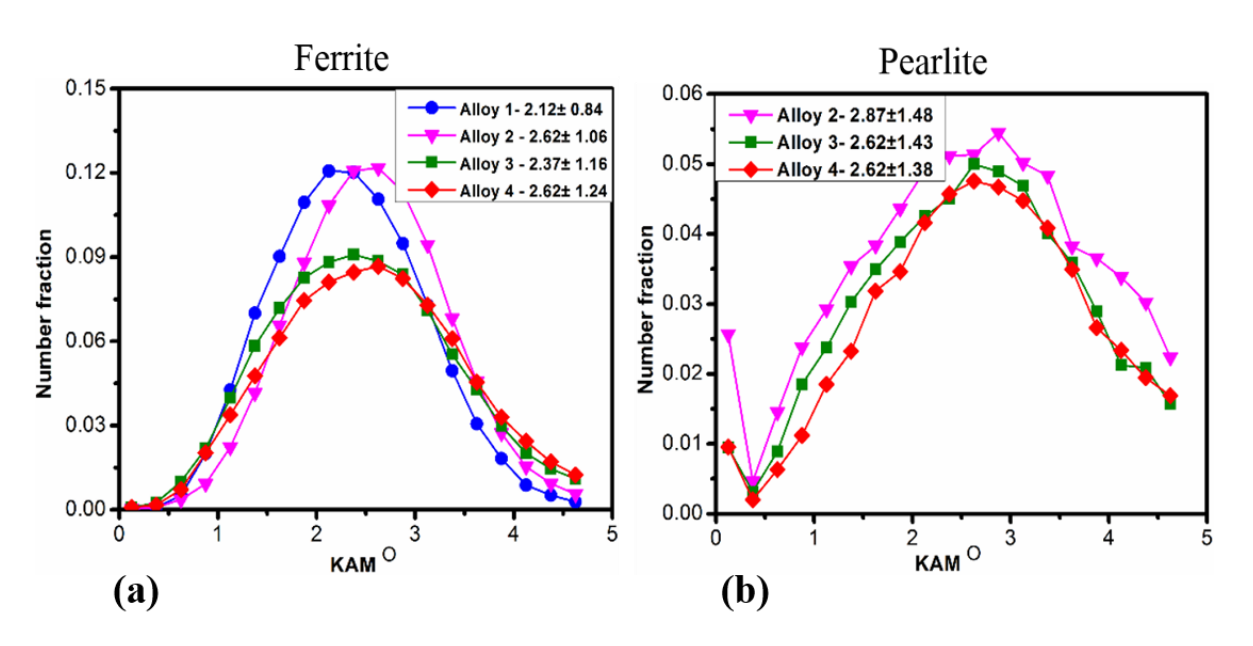


Figure 4-5 shows the KAM distribution of (a) ferrite and (b) pearlite after 80% cold rolling in Alloy 1, Alloy 2, Alloy 3, and Alloy 4.

4.3.6 MHV evolution after cold rolling

Figure 4-6 shows the hardness response of all 4 alloys. It was observed that alloy 1 which consisted of a single ferrite phase had the lowest hardness. In alloy 2 consisting of a non-banded pearlite structure, hardness slightly increases compared to alloy 1. Whereas in alloy 3-4 with banded pearlite, maximum hardness was observed in alloy 4 compared to alloy 3 and alloy 2.

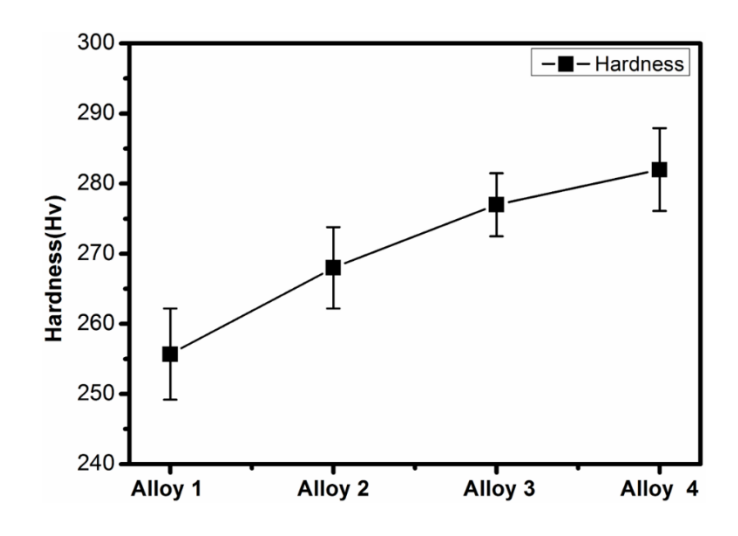


Figure 4-6 Hardness evolution after cold rolling in Alloy 1, Alloy 2, Alloy 3, Alloy 4

4.3.7 Nanoindentation hardness mapping after cold rolling

Figure.4-7 (a-b) shows the SEM micrographs with nanoindentation imprints and corresponding hardness maps of all the 4 alloys after 80% cold reduction. In alloy 1, which has only the ferrite phase, the corresponding hardness map shows mostly randomly distributed and ranges from 2 to 3.5 GPa. In contrast, in alloy 2-4, the SEM micrograph shows the presence of both ferrite and pearlite phases, the corresponding hardness map shows local variation in hardness in both ferrite and pearlite phases. Where deep blue cyan color corresponds to ferrite and the red color corresponds to pearlite. The hardness in the pearlite colony of the non-banded region is less in alloy 2 compared to the banded region in alloy 3-4. Also, the hardness of the pearlite in the banded region of alloy 4 is more than that of alloy 3 and alloy 2. It may be observed from all the maps that the mapping technique not only captures the hardness variation between ferrite and pearlite but also the variation in hardness between the banded in alloy 3/4and non-banded regions in alloy 2.

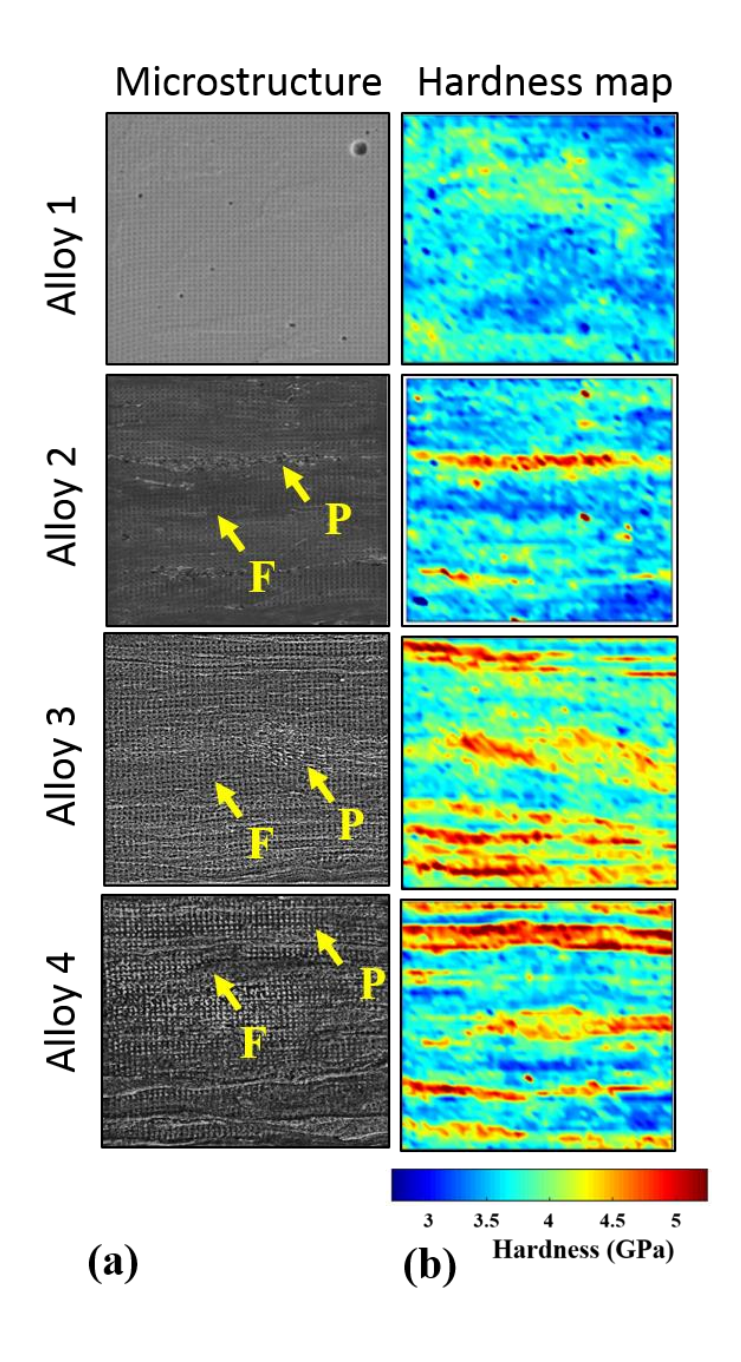


Figure 4-7 Shows (a) SEM micrographs and (b) hardness map 80% cold rolled microstructures with ferrite in alloy 1 and ferrite-pearlite phase's alloy 2, alloy 3, and alloy 4.

4.3.8 Deconvolution from Hardness maps

Figure.4-8 (a-b) shows the SEM micrographs with nanoindentation imprints and corresponding deconvoluted hardness map of ferrite and pearlite in all 4 alloys after 80% cold reduction. In alloy 1, which has only the ferrite phase, the corresponding phases map only

single ferrite with (blue color). Whereas alloys 2-4 consist of ferrite and pearlite as shown in Figure 4-8 (a). Corresponding deconvoluted maps in Figure 4-8(b), ferrite appears in blue and pearlite in red color. It was observed that a good spatial correlation exists between individual ferrite and pearlite phases features in SEM micrograph with the deconvoluted phase map

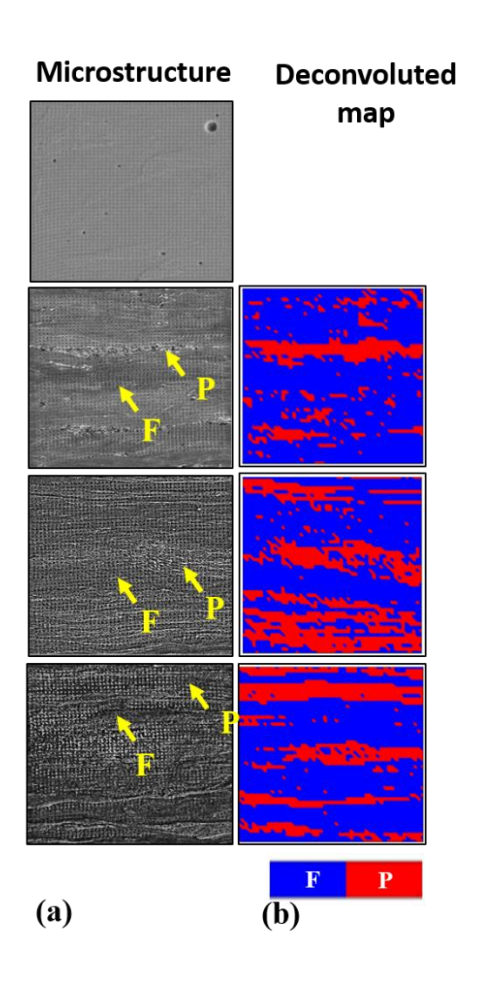


Figure 4-8 Showing (a) SEM micrographs and (b) deconvoluted maps in alloy 1 consisting of only ferrite and ferrite-pearlite phase's alloy 2, alloy 3, and alloy 4.

Hardness distribution of ferrite and pearlite after Cold rolling

It was well observed that a qualitative good spatial correlation exists between SEM micrograph, hardness map and deconvoluted phase map. To further have a deeper understanding of variation in properties in ferrite and pearlite in all the 4 alloys and hardness

histograms were plotted as shown in Figure 4-9. In the case of ferrite, as shown in Figure 4-9(a), the lowest hardness was observed in alloy 1, hardness peak slightly shifts towards the higher hardness for alloy 2, alloy 3 and alloy 4. In the case of pearlite as shown in Figure 4-9(b), the lowest hardness was observed in alloy 2, and the hardness peak shifts towards higher hardness in alloy 3 and alloy 4. It was observed that the variation in hardness in ferrite in all 4 alloys is very minimal. But hardness in pearlite shows significant variation.

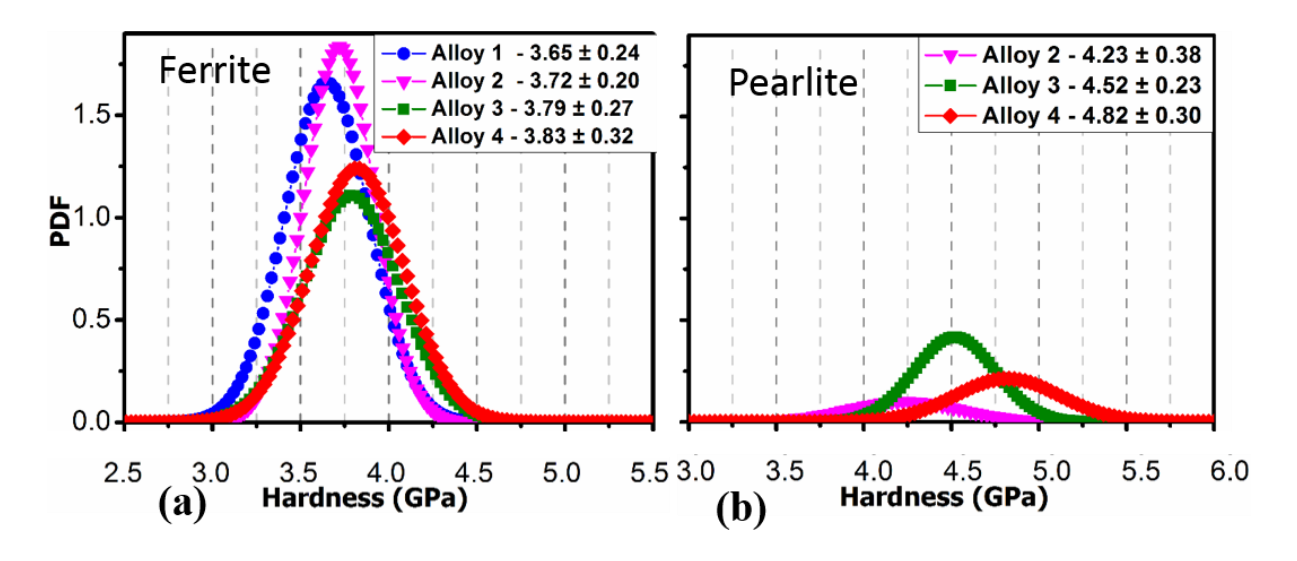


Figure 4-9 shows the hardness distribution of (a) ferrite and (b) pearlite of 80% cold rolled steel sheets in Alloy 1, Alloy 2, Alloy 3, Alloy 4

4.4 Discussions

In this section, two different aspects will be discussed, the role of alloy chemistry on the microstructure and properties evolution after cold rolling will be discussed. Further, insights on the role of individual phases (ferrite and pearlite) on structure and property correlation will be discussed.

4.4.1 Microstructure and properties evolution cold rolling

It was observed that microstructural evolution after hot rolling resulted in contrasting differences, alloy 1 resulted in single ferrite phases with coarse ferrite grains, and alloy 2-4 resulted in ferrite pearlite microstructure with fine ferrite grains. Alloys 2-4, also resulted in differences in pearlite area fraction, and distribution. These differences in the microstructural can be linked to the changes in alloy composition mainly C-Mn. In alloy 1, with the least amount of Carbon resulted in a single ferrite phase. An increase in Carbon causes decreases ferrite fraction and increases in area fraction of pearlite, its thickness as shown in Table 4.1, which consequently causes to increase in hardness in alloys 2-4 as shown in Figure 4-6. These results as overall in good agreement with the literature reported in [24,25] where increases in carbon results in increases in area fraction of pearlite and resulting in an increase in hardness in alloys 2-4. In alloy 2, a non-banded distribution of pearlite was observed and a banded distribution in alloy 3-4. The difference in distribution can be linked to the presence and the amount of manganese. Manganese causes segregation during solidification leading to banding in alloys 3 and 4 as reported by F.G. Caballero et al. [26]. An increase in manganese in alloys 3 and 4 is causing an increase in segregation during solidification and causing to increase in bandwidth of pearlite as shown in table 4.1. Subsequently, Cold rolling as shown in Figure 4-2, resulted in pancaked morphology in all four alloys and variation in morphology of cementite in pearlite. Alloy 2, resulted in the fragmented morphology of cementite in non-banded pearlite and lamellar morphology is retained in banded pearlite in alloys 3-4.

4.4.2 Role of pearlite on structure and property correlation in ferrite and pearlite.

Qualitatively KAM and nanoindentation mapping show good spatial correlation where, ferrite having higher IQ shows lower hardness and lower misorientation, pearlite having lower 1Q had higher hardness as in Figure 4-4 and 4-7. The local variation in misorientation by EBSD

and hardness by nanoindentation were also well captured after deconvolution in individual micro constituent's ferrite and pearlite as in Figure 4-5 and 4-9. To further get insights on the role of pearlite in the individual micro constituent's ferrite and pearlite after cold rolling. KAM misorientation and hardness changes in ferrite and pearlite obtained from deconvoluted data in Figure 4-5 and 4-9, were plotted as a function of pearlite fraction and is shown in Figure 4-10(a-b).

In the case of ferrite, as is shown in Figure 4-10(a), it was observed that increased pearlite fraction causes a slight increase in KAM misorientation and hardness in all four alloys 1-4. Hardness is representative of total dislocation density including statically stored dislocation (SSD) and geometry necessary dislocation (GND). Whereas KAM is representative of the distribution of dislocation density, mainly geometry necessary dislocation (GND). This suggests that a slight increase in KAM and hardness is mainly due to a slight increase in GND density. In the presence of this hard pearlite phase with soft ferrite, GNDs get piled up ferrite/ferrite and at the ferrite/pearlite boundaries, as GNDs cannot transmit across pearlite as observed in Figure 4-4. This makes the soft ferrite harder and increases the overall strength/hardness.

In the case of pearlite, as in Figure 4-10(b), an increase in pearlite fraction causes to hardness increase, whereas KAM doesn't show any differences in misorientation in pearlite consisting alloy 2-4. The reasons for the increase in hardness can be attributed to an increase in pearlite area fraction. As the increase in the amount of cementite causes to enhance the mechanical properties of the steel [10,25].

It was also observed that the broader peak in Figure 4-5 and 4-10 (large scatter in misorientation) in ferrite and pearlite in all the alloys 1-4, as shown in misorientation and hardness distribution, indicates inhomogeneous accommodation of strain. Many factors control the strain accommodation, such as ferrite grain size, orientation, and grain size, distribution of surrounding phases causes Peak broadening (scatter in misorientation)[16].

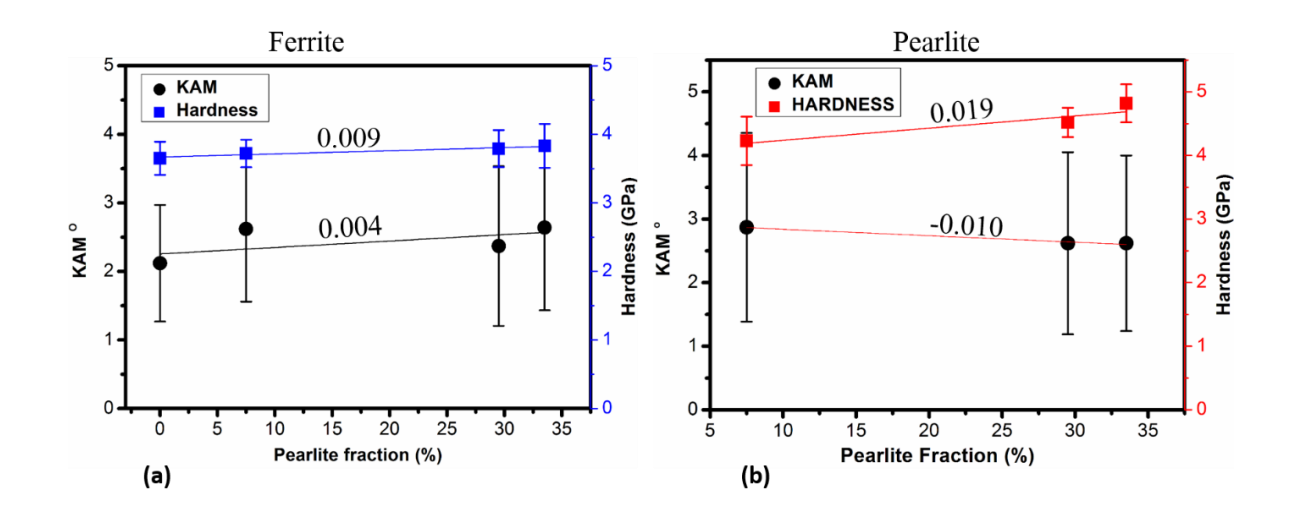


Figure 4-10 Role of pearlite on KAM misorientation and hardness in (a) ferrite and (b) pearlite after 80% cold rolling in alloy 1, alloy 2, alloy 3 and alloy 4.

4.5 Summary and conclusions

The present chapter focussed on microstructure and properties evolution after 80% cold rolling by varying C-Mn content in four different sheets of steel. It was observed increase in C-Mn content resulted in the difference in microstructure in terms of phase formation, its area fraction and distribution and the following conclusion can be drawn.

- 1. Alloy 1 with the least C-Mn shows a single ferrite phase.
- 2. Alloy 2-4, consisted of ferrite and pearlite microstructure, increasing Carbon resulted in an increase in pearlite fraction, increase in Mn content banded distribution of pearlite in alloy 3-4.

- 3. KAM evolution shows, strain localization inside the ferrite grains, at ferrite/ferrite boundaries and the ferrite/pearlite interfaces.
- 4. Micro Vickers hardness results show that the lowest hardness in alloy 1 consisting of only ferrite, in alloys 2-4, consisting of ferrite-pearlite hardness increases with increasing pearlite area fraction.
- 5. Nanoindentation shows higher hardness in pearlite regions compared to ferrite.

 Increases in pearlite fraction increase the hardness of pearlite in alloys 2-4.
- Deconvolution by K-means clustering algorithm was used successfully to extract the
 misorientation and hardness of ferrite and pearlite obtained from EBSD and
 nanoindentation mapping.
- 7. In alloys 1-4, ferrite phase, hardness, and KAM values are independent of pearlite fraction (almost zero slope).
- 8. In alloys 2-4, pearlite phase, hardness is dependent upon the pearlite fraction, whereas KAM is independent of the pearlite fraction.

References

- [1] C.C. Tasan, M. Diehl, D. Yan, M. Bechtold, F. Roters, L. Schemmann, C. Zheng, N. Peranio, D. Ponge, M. Koyama, K. Tsuzaki, D. Raabe, An Overview of Dual-Phase Steels: Advances in Microstructure-Oriented Processing and Micromechanically Guided Design, Annu. Rev. Mater. Res. 45 (2015) 391–431. https://doi.org/10.1146/annurev-matsci-070214-021103.
- [2] J. Galán, L. Samek, P. Verleysen, K. Verbeken, Y. Houbaert, Advanced high strength steels for automotive industry, Rev. Metal. 48 (2012) 118–131. https://doi.org/10.3989/revmetalm.1158.

- [3] M. Takahashi, Development of high strength steels for automobiles, Nippon Steel Tech. Rep. (2003) 2–7. https://doi.org/10.2320/materia.36.502.
- [4] M. Soleimani, A. Kalhor, H. Mirzadeh, Transformation-induced plasticity (TRIP) in advanced steels: A review, Mater. Sci. Eng. A. 795 (2020). https://doi.org/10.1016/j.msea.2020.140023.
- [5] P.S. Bate, J. Quinta da Fonseca, Texture development in the cold rolling of IF steel, Mater. Sci. Eng. A. 380 (2004) 365–377. https://doi.org/10.1016/j.msea.2004.04.007.
- [6] L.A.I. Kestens, H. Pirgazi, Texture formation in metal alloys with cubic crystal structures, Mater. Sci. Technol. (United Kingdom). 32 (2016) 1303–1315. https://doi.org/10.1080/02670836.2016.1231746.
- [7] H. Inagaki, Fundamental Aspect of Texture Formation in Low Carbon Steel, ISIJ Int. 34 (1994) 313–321. https://doi.org/10.2355/isijinternational.34.313.
- [8] R.K. Ray, J.J. Jonas, R.E. Hook, Cold rolling and annealing textures in low carbon and extra low carbon steels, 1994. https://doi.org/10.1179/imr.1994.39.4.129.
- [9] Microstructure and Texture in Steels, Microstruct. Texture Steels. (2009). https://doi.org/10.1007/978-1-84882-454-6.
- [10] T. Takahashi, D. Ponge, D. Raabe, Investigation of orientation gradients in pearlite in hypoeutectoid steel by use of orientation imaging microscopy, Steel Res. Int. 78 (2007) 38–44. https://doi.org/10.1002/srin.200705857.
- [11] F.M. Castro Cerda, L.A.I. Kestens, A. Monsalve, R.H. Petrov, The effect of ultrafast heating in cold-rolled low carbon steel: Recrystallization and texture evolution, Metals (Basel). 6 (2016). https://doi.org/10.3390/met6110288.
- [12] S. Janakiram, J. Gautam, P.S. Phani, L.A.I. Kestens, Microstructural and micro hardness variation during low temperature recovery annealing in C-Mn high strength Steels, J. Phys. Conf. Ser. 1270 (2019). https://doi.org/10.1088/1742-6596/1270/1/012017.
- [13] X. Wu, Y. Zhu, Heterogeneous materials: a new class of materials with unprecedented mechanical properties, Mater. Res. Lett. 5 (2017) 527–532.

- https://doi.org/10.1080/21663831.2017.1343208.
- [14] C. Tian, D. Ponge, L. Christiansen, C. Kirchlechner, On the mechanical heterogeneity in dual phase steel grades: Activation of slip systems and deformation of martensite in DP800, Acta Mater. 183 (2020) 274–284. https://doi.org/10.1016/j.actamat.2019.11.002.
- [15] J. Kadkhodapour, S. Schmauder, D. Raabe, S. Ziaei-Rad, U. Weber, M. Calcagnotto, Experimental and numerical study on geometrically necessary dislocations and non-homogeneous mechanical properties of the ferrite phase in dual phase steels, Acta Mater. 59 (2011) 4387–4394. https://doi.org/10.1016/j.actamat.2011.03.062.
- [16] M. Calcagnotto, D. Ponge, E. Demir, D. Raabe, Orientation gradients and geometrically necessary dislocations in ultrafine grained dual-phase steels studied by 2D and 3D EBSD, Mater. Sci. Eng. A. 527 (2010) 2738–2746. https://doi.org/10.1016/j.msea.2010.01.004.
- [17] R.R. Shen, V. Ström, P. Efsing, Spatial correlation between local misorientations and nanoindentation hardness in nickel-base alloy 690, Mater. Sci. Eng. A. 674 (2016) 171–177. https://doi.org/10.1016/j.msea.2016.07.123.
- [18] S.N. Kane, A. Mishra, A.K. Dutta, Preface: International Conference on Recent Trends in Physics (ICRTP 2016), J. Phys. Conf. Ser. 755 (2016). https://doi.org/10.1088/1742-6596/755/1/011001.
- [19] J. Gautam, A. Miroux, J. Moerman, L. Kestens, TNR dependent hot rolling microstructure and texture development in c-Mn dual phase and HSLA steels, Defect Diffus. Forum. 391 (2019) 120–127. https://doi.org/10.4028/www.scientific.net/DDF.391.120.
- [20] P. Sudharshan Phani, W.C. Oliver, A critical assessment of the effect of indentation spacing on the measurement of hardness and modulus using instrumented indentation testing, Mater. Des. 164 (2019) 1–10. https://doi.org/10.1016/j.matdes.2018.107563.
- [21] E.A. Ariza-Echeverri, M. Masoumi, A.S. Nishikawa, D.H. Mesa, A.E. Marquez-Rossy, A.P. Tschiptschin, Development of a new generation of quench and partitioning steels: Influence of processing parameters on texture, nanoindentation, and mechanical properties, Mater. Des. 186

- (2020). https://doi.org/10.1016/j.matdes.2019.108329.
- [22] B. Vignesh, W.C. Oliver, G.S. Kumar, P.S. Phani, Critical assessment of high speed nanoindentation mapping technique and data deconvolution on thermal barrier coatings, Mater. Des. 181 (2019). https://doi.org/10.1016/j.matdes.2019.108084.
- [23] S. Journal, R. Statistical, S. Series, C.A. Statistics, Algorithm AS 136: A K-Means Clustering Algorithm Author (s): J. A. Hartigan and M. A. Wong Published by: Blackwell Publishing for the Royal Statistical Society Stable URL: http://www.jstor.org/stable/2346830, 28 (2009) 100–108.
- [24] L. Zhou, J. Liu, X.J. Hao, M. Strangwood, A.J. Peyton, C.L. Davis, Quantification of the phase fraction in steel using an electromagnetic sensor, NDT E Int. 67 (2014) 31–35. https://doi.org/10.1016/j.ndteint.2014.06.007.
- [25] C.M. Bae, C.S. Lee, W.J. Nam, Effect of carbon content on mechanical properties of fully pearlitic steels, Mater. Sci. Technol. 18 (2002) 1317–1321. https://doi.org/10.1179/026708302225007556.
- [26] F.G. Caballero, A. García-Junceda, C. Capdevila, C.G. De Andrés, Evolution of microstructural banding during the manufacturing process of dual phase steels, Mater. Trans. 47 (2006) 2269–2276. https://doi.org/10.2320/matertrans.47.2269.

Chapter 5

Insights on early recovery kinetics at 300 °C 5

In this chapter, we investigate the role of pearlite on static recovery kinetics of 80% cold-rolled steel sheets at annealing temperatures at 300 °C. As a part of thermomechanical processing, all the steel sheets were cold rolled to 80 percent, then low-temperature annealing process in the recovery regime. We have chosen steels with varying carbon content, resulting in different compositions of the pearlite. Certain minor modifications to the composition also resulted in minor changes in the morphology of pearlite. In addition to this, we have also selected a ULC steel that is composed of single phase ferrite without pearlite. These aspects provide a good platform to systematically explore the effect of pearlite on the early recovery kinetics during thermomechanical processing, i.e. in the early stages of the annealing treatment.

5.1 Introduction

A wide variety of AHSS such as HSLA, DP, TRIP steels is materials of choice for structural parts employed in the car industry as a result of their mix of mechanical properties (specifically an optimum balance of strength vs ductility), which helps in weight reduction and increase in safety and performance [1–6]. Precise mechanical properties of these steels are tailored by understanding the microstructural aspects during thermomechanical processing involving hot rolling, cold rolling and annealing (recovery recrystallization and phase transformation). To date, extensive studies have been carried out mainly in the intercritical annealing region of initial ferrite-pearlite cold rolled steels [1,4,6]. whereby complex metallurgical phenomena

may occur concurrently such as recovery, recrystallization, grain growth of ferrite grains, carbon diffusion, austenite nucleation and growth, etc [4,6]. However, the recovery of the initial ferrite-pearlite cold rolled structure has comparatively received less attention. The above-mentioned metallurgical phenomena are inherently interlinked with each processing stage during thermomechanical processing. It is quite challenging to isolate the role of each phenomenon during the intercritical annealing due to interacting processes, which may influence the microstructure and properties ensuing from the entire process. Recently, present authors [7] have studied the effect of the banded morphology of pearlite in HSS and observed hardness increase from cold rolled state before the onset of recovery and recrystallization. During recovery annealing [8,9] dissolution of carbon from cementite in pearlite shows temperature-dependent hardness changes in ferrite and pearlite consisting of AHSS. However, the role of pearlite on hardness kinetics during recovery annealing in different grades of HSS is not yet fully understood. The importance of a precise understanding of ferrite recovery in the cold rolled ferrite/pearlite structure is that it may potentially alter the microstructure at the beginning of the recrystallization and intercritical annealing process. Investigating the role of pearlite in different HSS has important implications in fine-tuning the thermomechanical processing like heating rate or soaking time or temperature of the intercritical annealing treatment, or may even lead to a better alloy design in terms of chemical composition. Recovery in ferrite-containing steels, like ELC [10] and ULC [11]has been well studied. In ELC steels[10] and it is reported that at low temperatures annealing below 500 °C hardness is insensitive to annealing time. Microstructural examination revealed that deformed arrangements of grain are still present. Magnetic testing was carried out to a higher degree of

resolution to investigate the recovery phenomena. It was observed that coercive field Hc,

decreases progressively with time in the annealing temperature range 300-400 °C suggesting dislocation annihilation drives the recovery, as the coercive field is directly related to dislocation density[10]. EBSD investigation revealed that stored energy is distributed heterogeneously in cold rolled state, the recovery rate was higher in γ gamma fiber compared to α fiber in other orientations [10]. In ULC steels[11], recovery was assessed by hardness and magnetic coercivity (Hc), at lower temperatures (350 to 520 °C) recovery progresses by dislocation annihilation.

Recovery in fully pearlitic steels ultra-high strength steels (UHSS) [12–14] the presence of cementite complicates the recovery of ferrite. Prior work suggests in pearlitic steels [12], ferrite recovery starts with agglomeration and annihilation of vacancy, vacancy clusters are surrounded by carbon atoms, dislocation in ferrite is stabilized by the carbon atoms, where a negligible change in dislocations is observed below 250 °C. All the above structural changes lead to an increase in strength. In C-Mn steels [15] The recovery of ferrite is explored, and it was discovered that activation energy and activation volume for the recovery process change with temperature, but not with strain and strain rate. The activation energy is near to dislocation core diffusion at low temperatures (150-300 °C). During recovery, the micro-mechanism kinetics are thermodynamically irreversible transformations and influenced by many factors such as chemical composition [16], thermomechanical parameters [16,17] degree of rolling reduction [18], the temperature of annealing [10,15], annealing soaking time and solute content [19–21]. Such recovery kinetics in HSS consisting of ferrite-pearlite microstructure, in different grades of HSS steels has often been ignored and not well understood.

Unlike recrystallization and phase transformation investigating recovery is quite challenging with (electron-) microscopy exclusively, due to subtle changes in the microstructural features.

Therefore, recovery was investigated by complementary techniques such as magnetic NDT [10] or TEP [22] resistivity[23] hardness and yield strength [10,24].

The microhardness technique is simple and yet powerful, especially in investigating recovery in single phase steels [10]. However, in the case of HSS, the microhardness cannot give the entire picture in distinguishing between ferrite and pearlite. This makes it very complicated to thoroughly understand recovery in HSS with micro Vickers hardness. In this regard, this chapter proposes to provide key insights into early recovery of AHSS steel by measuring the mechanical properties at the microstructure level ($\sim 1~\mu m$) and establishing the structure and property correlation at that scale by coupling with EBSD and nanoindentation. In addition, a TEM investigation is also carried out for the selected cases to provide a comprehensive understanding of what drives recovery in HSS.

5.2 Experimental procedure:

5.2.1 Composition and processing:

Table 3.1 in chapter 3 lists the composition of four different steel sheets with varying C-Mn content used in the present study. All the four cold rolled steel sheets were recovery annealed in a muffle furnace at 300 °C for 30, 60, 120, 300 minutes of soaking time, followed by furnace cooling till room temperature. Mechanical polishing was carried out on SiC papers, followed by coarse alumina polishing and vibratory polishing for 8 hr with fine colloidal silica of 50 nm.

5.2.2 Characterization and mechanical testing:

High-resolution EBSD mapping was performed with an SEM of type FEI NOVA NANOSEM 450, with an accelerating voltage of 20 kV, at a working distance of 15mm and step size 80 nm with a hexagonal grid on 26 µm x 26 µm area. The data set obtained from the EBSD map was used to identify and partition ferrite-pearlite regions based on the image quality (IQ) of

the diffraction pattern as reported in [26]. Kernel average misorientation (KAM), obtained from EBSD was used to measure the local misorientation at the subgrain scale in ferrite and pearlite. As KAM measures the misorientation between the center of the pixel and its neighbor, in the present case KAM was calculated with 5th neighbour and a tolerance limit of 5° misorientation. The microstructural changes from cold rolled to recovery annealed in ferrite and pearlite are qualitatively and quantitatively assessed by KAM maps and their distribution is shown and correlated with the hardness changes. TEM observations were carried out on JEOL 2100 with a focus on the ferrite and pearlite region in the cold rolled and annealed samples.

Microhardness and nanoindentation measurements were performed on these well-polished samples. Micro Vickers hardness measurements were performed using a Tenuis Olsen FH 006 series machine on all the cold-rolled and annealed specimens with a Load of 500 gram and 20 s dwell time. Nanoindentation mapping was performed using a commercially available nanoindenter iMicro® with an InForce50 actuator from Nanomechanics Inc. (now KLA Corporation), Oak Ridge, USA. Multiple large indentation maps with 2500 indents per map on a 50 μ m x 50 μ m area were collected using the NanoBlitz3D high-speed mapping technique. An indentation spacing of 1 μ m was maintained and the load was changed such that the indentation depth was 100 nm or lower, which results in a minimum spacing to depth ratio of 10, as per the recommendations of Sudharshan Phani et al [27].

5.3 Results

5.3.1 Microstructural evolution by SEM

Microstructural changes after annealing at 300 °C for 30,60,120 and 300 min of soaking time in four different grades of cold rolled steels are shown in Figure 5-1(a-d). Where, alloy 1.

Consists of a single ferrite phase as in Figure 5-1(a) and alloys 2-4 consist, of ferrite (in grey) and pearlite appears in white as shown in Figure 5-1(b-d). In alloy 1, the cold rolled microstructure is retained even after annealing at 300 °C for 300 min of soaking time. In alloy 2-4, also ferrite and pearlite did not show any significant differences even after annealing at 300 °C for 300 min of soaking time and retaining its initial cold rolled condition.

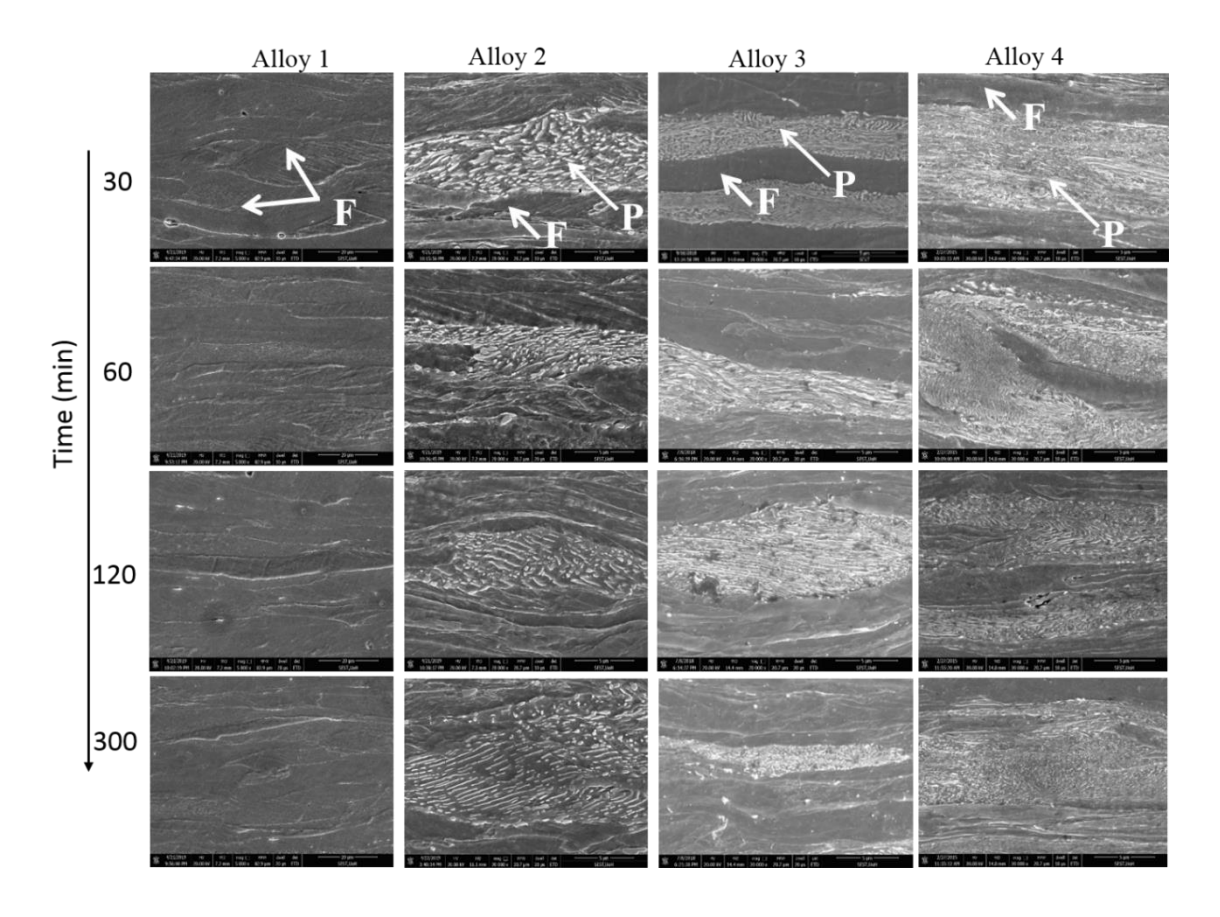


Figure 5-1 Shows microstructural changes after recovery annealing at 300° for 30, 60,120 and 300 min of soaking time in (a) Alloy 1, and ferrite pearlite phases, (b) Alloy 2, (c) Alloy 3 (d) Alloy 4 [28]

F-ferrite, P-pearlite

5.3.2 KAM evolution

To further provide microstructural insights at the substructure level, KAM maps were obtained from EBSD. Ferrite consisting alloy 1 and ferrite-pearlite consisting alloy 2-4 will be compared to demonstrate the effect of pearlite on the substructure evolution during annealing at 300 °C

for different soaking times are shown in Figure. 5-2. In chapter 4, the identification of ferrite and pearlite were well presented by combining IQ, KAM maps after cold rolling in Figure 4-2. It was well demonstrated that the higher IQ and lower KAM values are indicative of the ferrite phase both in alloys 1 and alloy 2-4; conversely, the lower IQ and higher KAM value correspond to pearlite in alloy 2-4. This chapter only presents the color-coded KAM map on annealing at 300 °C for different soaking times as shown in Figure. 5-2. The color blue indicates the strain-free regions in the microstructure with a misorientation of less than 1°, while a red represents the structure with higher lattice distortion \geq 4-5 ° [29].

On annealing at 300°C for 300 min, the cold-rolled elongated grains are is still retained in both alloy 1 and alloys 2-4 as shown in Figure 5-2. In Alloy 1, the misorientation in ferrite almost remains similar for 30-60 min of soaking time. Further increasing time after 120 min misorientation decreases inside the grains and starts to appear blue indicating recovery. Alloys 2-4, show slight changes in misorientation inside and at the grain boundaries in both ferrite and pearlite regions compared to the cold-rolled state, indicating some microstructural changes.

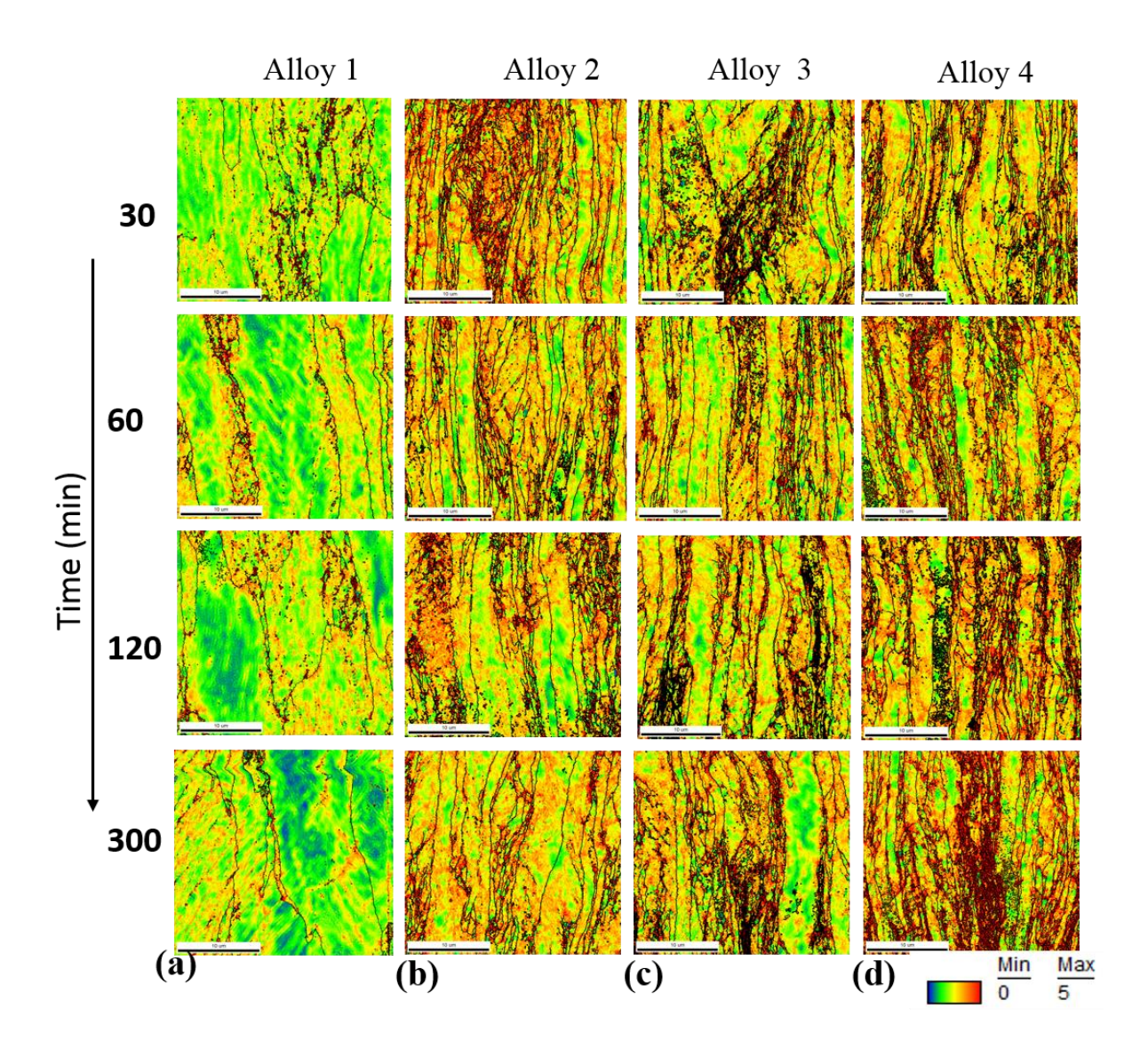


Figure 5-2 Kernel average misorientation (KAM) changes after recovery annealing at 300° for 30, 60,120 and 300 min of soaking time in (a) Alloy 1, and ferrite pearlite phases, (b) Alloy 2, (c) Alloy 3 (d) Alloy 4

5.3.3 KAM distribution

To quantify the microstructural changes presented in the KAM maps shown in Figure. 5-2, histograms of the KAM misorientation are plotted in the individual phases ferrite and pearlite. The changes in KAM distribution from cold rolled to recovery annealed condition at 300°C for 30, 60, 120 and 300 min of soaking time are shown in Figure.5-3 for all 4 alloys.

In the ferrite alloy 1, the average KAM remains similar to cold rolled conditions even after annealing at 300 °C up to 300 min of soaking time; it was observed that at 300 min of soaking time KAM distribution starts shifting towards the left side indicating the onset of recovery. Contrastingly, in the ferrite/pearlite alloys 2, 3 and 4, the KAM distribution of the ferrite phase slightly shifts to the right side towards a higher KAM value as compared to the cold-rolled state indicating an increase of short-range orientation gradients. It was also observed that increasing the soaking time in these alloys did not produce any significant shift in the KAM distribution of the ferrite phase. In the case of pearlite, in alloy 2- 4, the KAM distribution shows a slight shift into higher KAM values compared to the cold-rolled state indicating an increase in short-range orientation gradients. Varying the soaking time resulted in slight changes in KAM. Up to 60 min of soaking time KAM value increases and then starts to decrease. It was observed that KAM remain higher or similar to cold rolled state.

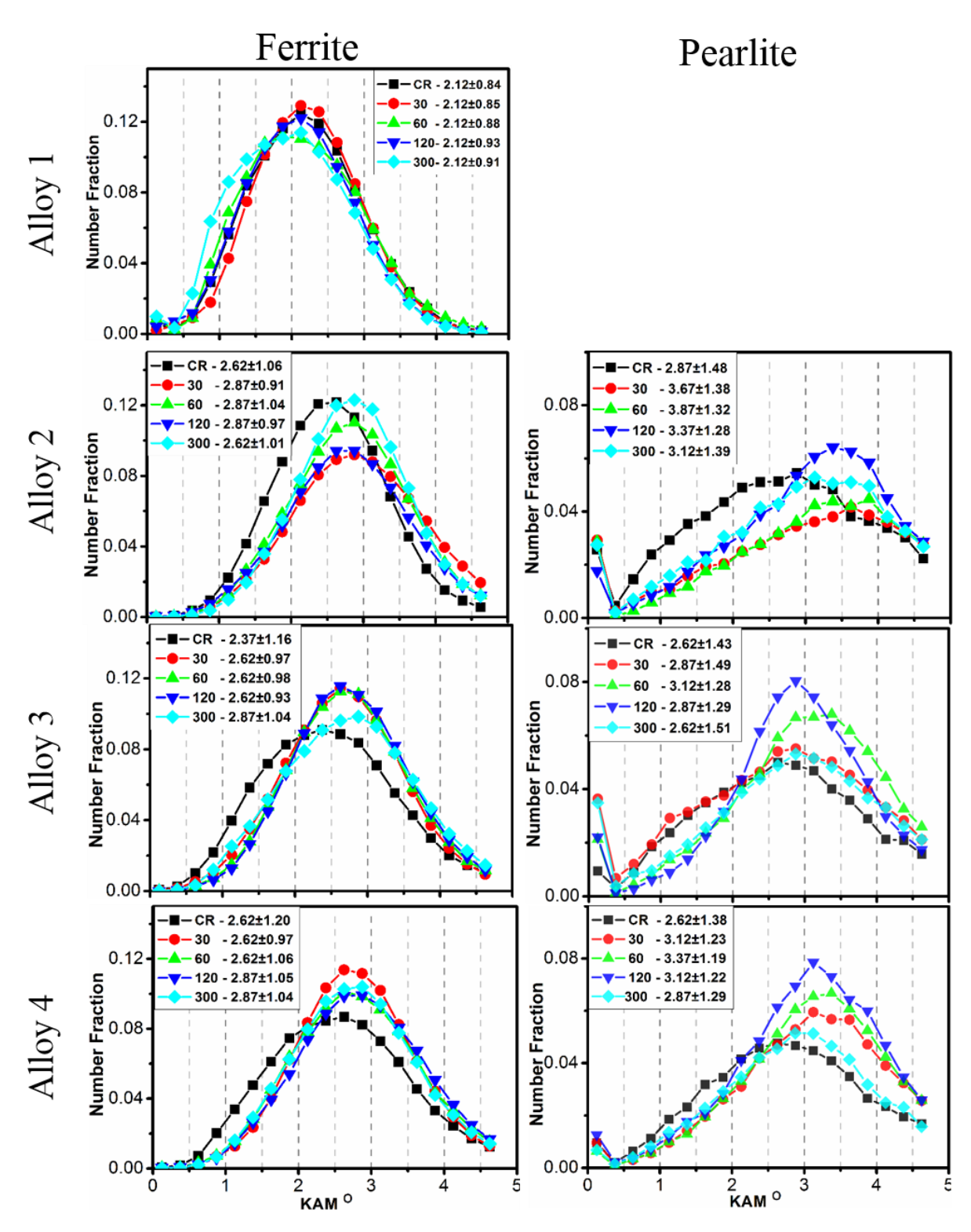


Figure 5-3 Kernel average misorientation (KAM) distribution of ferrite and pearlite from cold rolled to recovery annealed at 300 °C at a different soaking time in alloy 1, alloy 2, alloy 3, and alloy 4

5.3.4 TEM analysis

To characterize the microstructure at a nanometre length scale TEM investigation was carried out on alloy 3 as a representative material having both ferrite and pearlite phases. The TEM micrographs show the microstructural evolution from cold rolled to recovery annealed at 300 °C for 30 and 300 min in both the ferrite and pearlite phases, as shown in Figure. 5-4(a-c) and Figure. 5-4(d-f), respectively. The bulk ferrite phase of the cold rolled sample, as shown in Figure 5-4(a), exhibits a cellular structure with thick cell boundaries due to accumulation and entanglement of dislocations as expected for cold-rolled structure. Upon annealing at 300 °C for 30 min, as in Figure 5-4 (b-c), the microstructure shows dislocation rearranging into perfect cell and the cell boundaries are sharpening gradually leading to sub grain formation. In addition, clusters of carbide precipitates on sub boundaries (yellow dotted arrow) can be observed at soaking time to 300 min in Figure. 5-4(c). The microstructural evolution of the pearlitic phase consisting of cementite and ferrite is shown in Figure 5-4(d-f). It is observed that dislocations are accumulation in pearlitic ferrite and interface of ferrite cementite, a typical cold rolled structure appears as shown in Figure 5-4(d). Upon annealing, cementite appears diffused indicated in (white arrow) and a higher amount of dislocation clouds are still present as shown in Figure 5-4(e). Increasing the soaking time to 300 min cementite further diffuses and causes thinning as compared to 30 min of soaking time and dislocation clouds are still present.

In summary, it was observed that annealing at 300 °C for 30 min results in rearrangement of dislocation by subgrain formation in ferrite and cementite starts diffusing in pearlite. Further increasing the soaking time to 300 min results in clustering/precipitation of carbides in sub boundaries in ferrite and in pearlite cementite lamellae further diffuses and causes thinning.

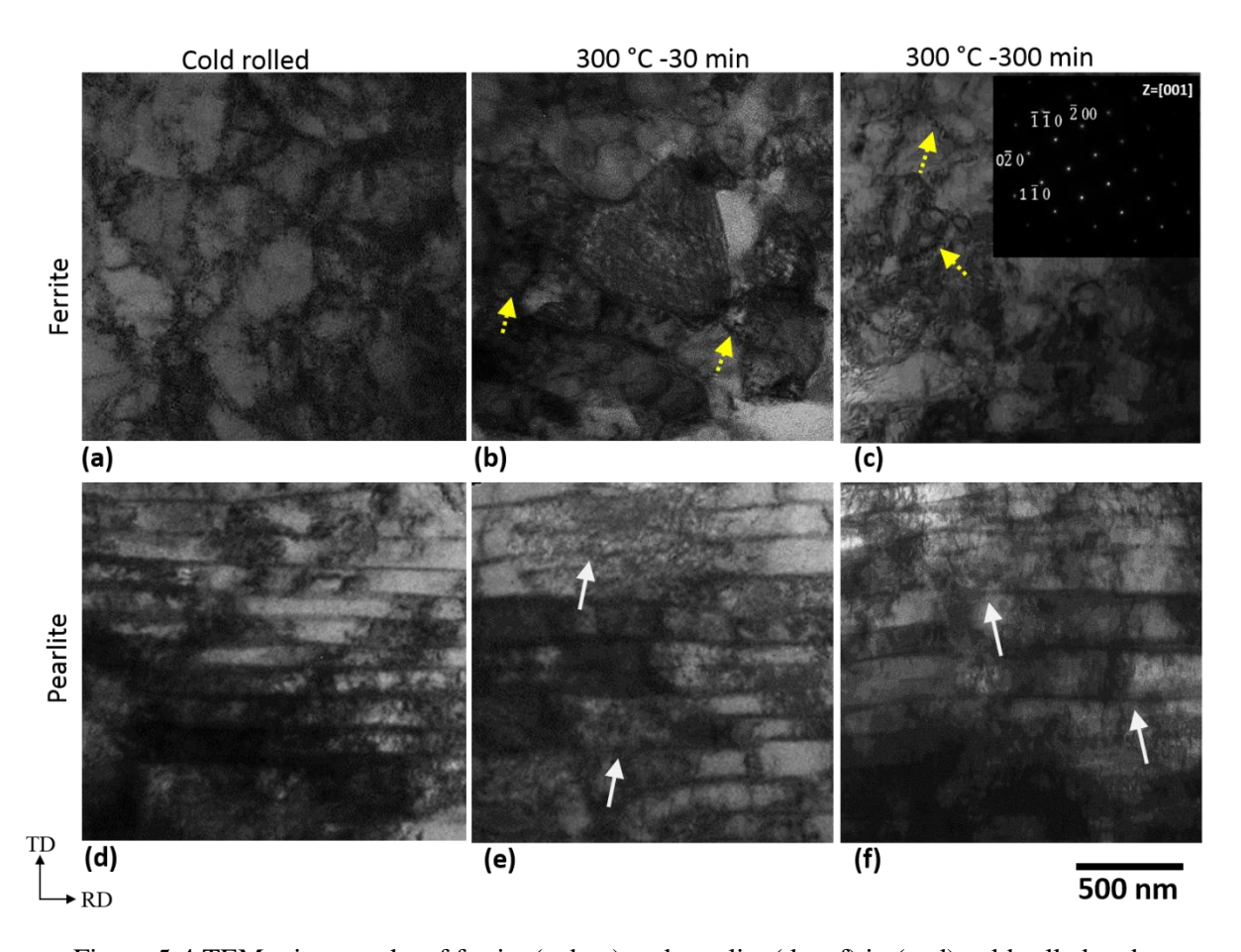


Figure 5-4 TEM micrographs of ferrite (a, b, c) and pearlite (d, e, f) in (a, d) cold rolled and subsequently recovery annealed at 300 $^{\circ}$ C for (b, e) 30 min and (c, f) 300 min of soaking time. Images in ferrite and pearlite were acquired along the z = [001] axis.

5.3.5 Micro hardness

Figure. 5-5 shows the Vickers hardness response as a function of soaking time for different alloys at 300 °C for 30, 60, 120 and 300 min of soaking time. During annealing at 300 °C alloy 1 for a short soaking time of 30 min sustains the hardness of the cold rolled state and then slightly decreases with increasing soaking time. In alloys 2, 3 and 4 the hardness increases and

remains above the cold rolled condition even after 300 min of soaking time. In alloy 2, with non-banded pearlite structure, the hardness slightly increases after 30 min annealing and saturates subsequently. Whereas in alloy 3 with a banded pearlite microstructure, with the increase in soaking time the hardness continues to increase. Conversely, in alloy 4, with an equally banded pearlite microstructure, the hardness increases and reaches a maximum after 120 min and then slightly decrease after 300 min of soaking time, though the hardness remains above the initial cold-rolled condition.

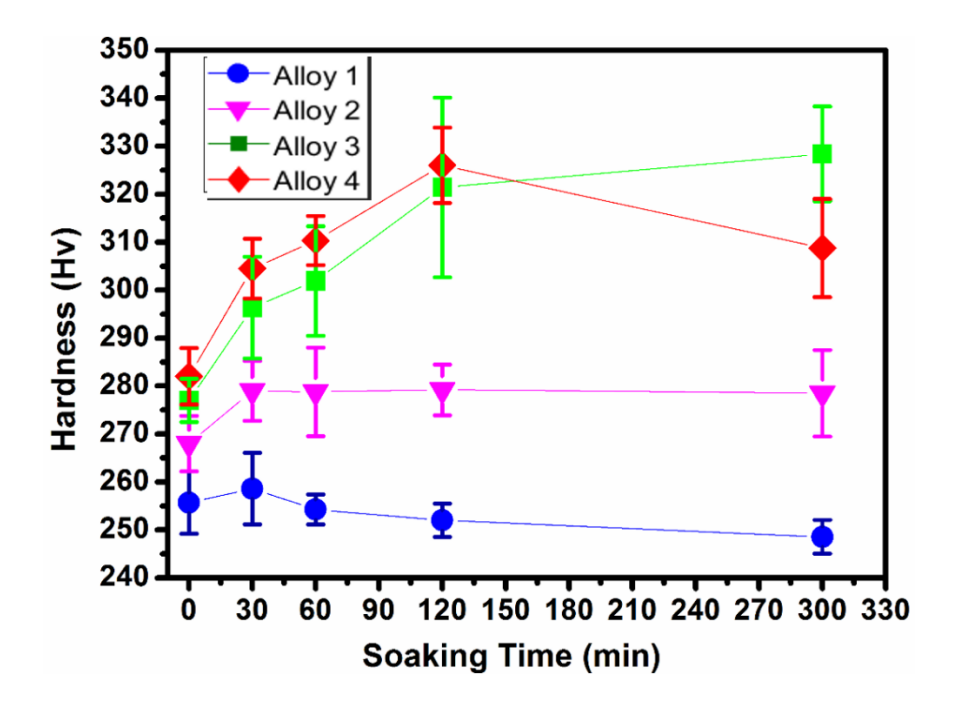


Figure 5-5 Micro Vickers hardness as a function of soaking time after recovery annealing at 300 °C for 30, 60, 120,300 min of soaking time in Alloy 1, Alloy 2, Alloy 3 and Alloy 4 [28].

Hardness at 0 min refers to the cold-rolled state.

5.3.6 Nanoindentation mapping

The idents of the micro Vickers results shown in the previous section exhibit a length scale $(25*25~\mu m)$ that is larger than the pearlite band. To explore the local behavior of micro constituents (ferrite, pearlite) at the micrometer length scale, high speed-high resolution nanoindentation mapping is performed on all the materials after 30 min of annealing at 300

°C, as shown in Figure 5-6. In a previous chapter, an excellent correlation between the microstructure and the corresponding hardness map was obtained in the cold-rolled condition of all the alloys. Here we show the hardness maps for all the materials with varying pearlite content starting from alloy 1 (0 % pearlite) to alloy 4 (33.5 %).

In the cold-rolled condition for ferrite alloy 1, the hardness is mostly randomly distributed and ranges from 2 to 4 GPa. In contrast, in ferrite-pearlite alloys 2-4 the hardness in the cold rolled condition shows more local variations corresponding to the two phases for both the non-banded and banded regions. The hardness in the pearlite colony of the non-banded region is less compared to the banded region. Also, the hardness of the pearlite in the banded region of alloy 4 is more than that of alloy 3. After recovery annealing at 300 °C for 30 min, the hardness of alloy 1 does not show any variation compared to the cold-rolled condition. In the case of alloys 2-4 the hardness of both pearlite and ferrite phases increases compared to cold rolled conditions. The hardness increases are higher in both ferrite and pearlite phases in the band structured alloys 3/4 compared to non-banded alloy 2.

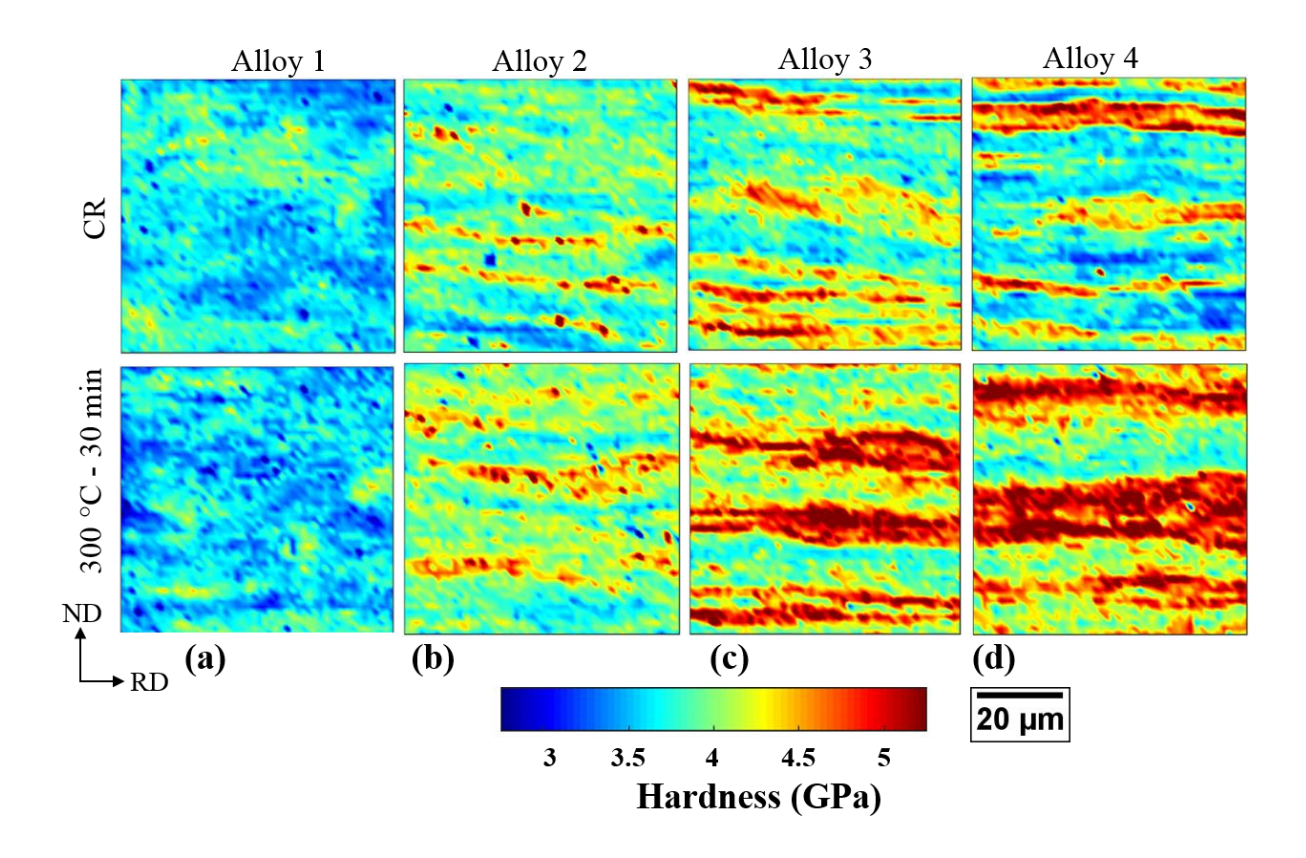


Figure 5-6 Nanoindentation hardness mapping of alloy 1, alloy 2, alloy 3/4 in cold rolled state and after recovery annealing at 300 °C for 30 min.

5.3.7 Hardness of ferrite and pearlite

Quantitative hardness Probability Density Function (PDF)'s of both ferrite and pearlite phases are shown in Figure 5-7. The shift in the peak position from cold rolled to recovery annealed condition at 300 and 500 °C for 30 min are tracked. The average peak values and the corresponding standard deviation of each material at a given condition are reported in the legend of Figure 5 (top right).

In the cold rolled state, in the ferrite phase, the lowest hardness was observed in alloy 1; the hardness peak slightly shifts towards a higher value for alloys 2, 3 and 4. For the pearlite phase, the lowest hardness was observed in alloy 2, whereas the hardness peak shifts towards higher

values in alloy 3 and alloy 4. On annealing at 300 °C, the hardness of the ferrite phase of alloy 1 steel remains similar to the cold-rolled state, whereas in alloys 2, 3 and 4 the hardness peak shifts towards the right side indicative of a hardness increase in comparison to cold rolled state. A similar peak shift to higher values was observed in the pearlite phase of alloys 2, 3 and 4. Both for the ferrite and pearlite phase, it was observed that the peak shift was more pronounced in alloy 4 as compared to alloys 2 and 3. This aspect will be revisited in the discussion section in terms of the pearlite fraction and defect density.

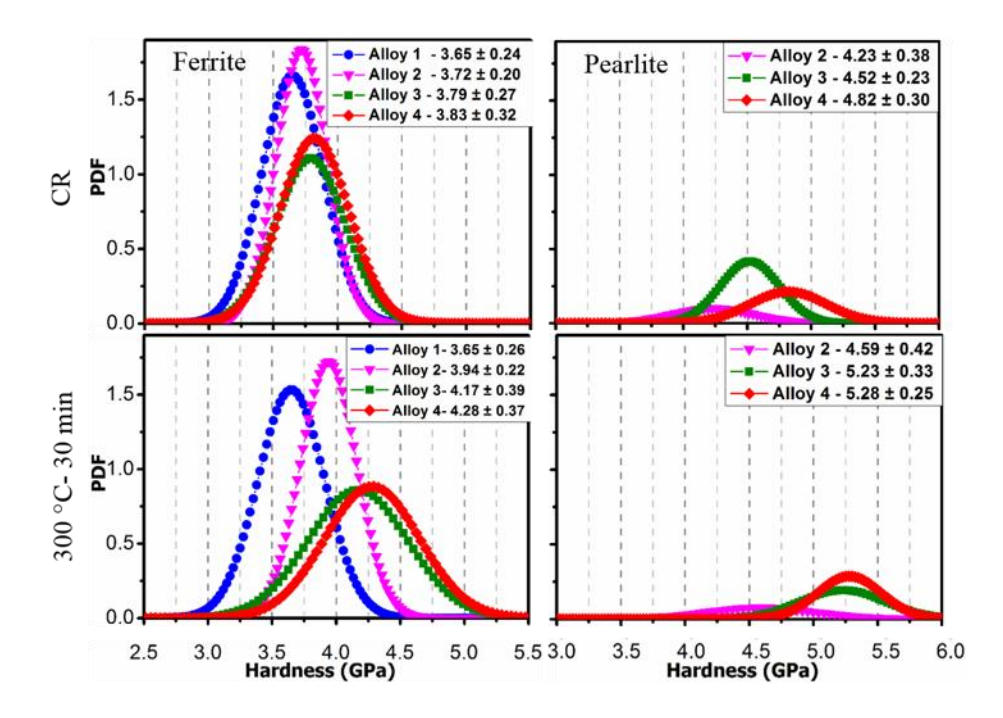


Figure 5-7 Hardness histograms of ferrite and pearlite in alloy 1, alloy 2, alloy 3/4 in cold rolled state and after recovery annealing at 300 °C for 30 min.

5.4 Discussion

In this section, insights from combining the results of microscopy, nanoindentation and simple models for kinetics will be provided to present a comprehensive picture of what drives the kinetics or the dominant mechanisms at 300 °C. Mainly, hardness increases during annealing at 300 °C and the associated microstructural changes will be discussed. The occurring

processes are evaluated by empirical kinetic laws to identify the mechanisms taking place at 300 °C. Further, insights on the role of individual phases (ferrite and pearlite) during hardness increases and decreases kinetics will be discussed.

5.4.1 Recovery kinetics

In this section, we present the hardness kinetics and the associated driving mechanisms will be discussed. As observed from micro Vickers hardness tests in Figure.5-5, ferrite-pearlite consisting steels show the hardness changes at 300 °C, and are also dependent on soaking time. Kinetics models such as Cottrell atmosphere formation at 300 °C are quantitatively assessed as shown in Figure.5-8. Hardness changes deduced in Cottrell models are combined effects of both ferrite and pearlite.

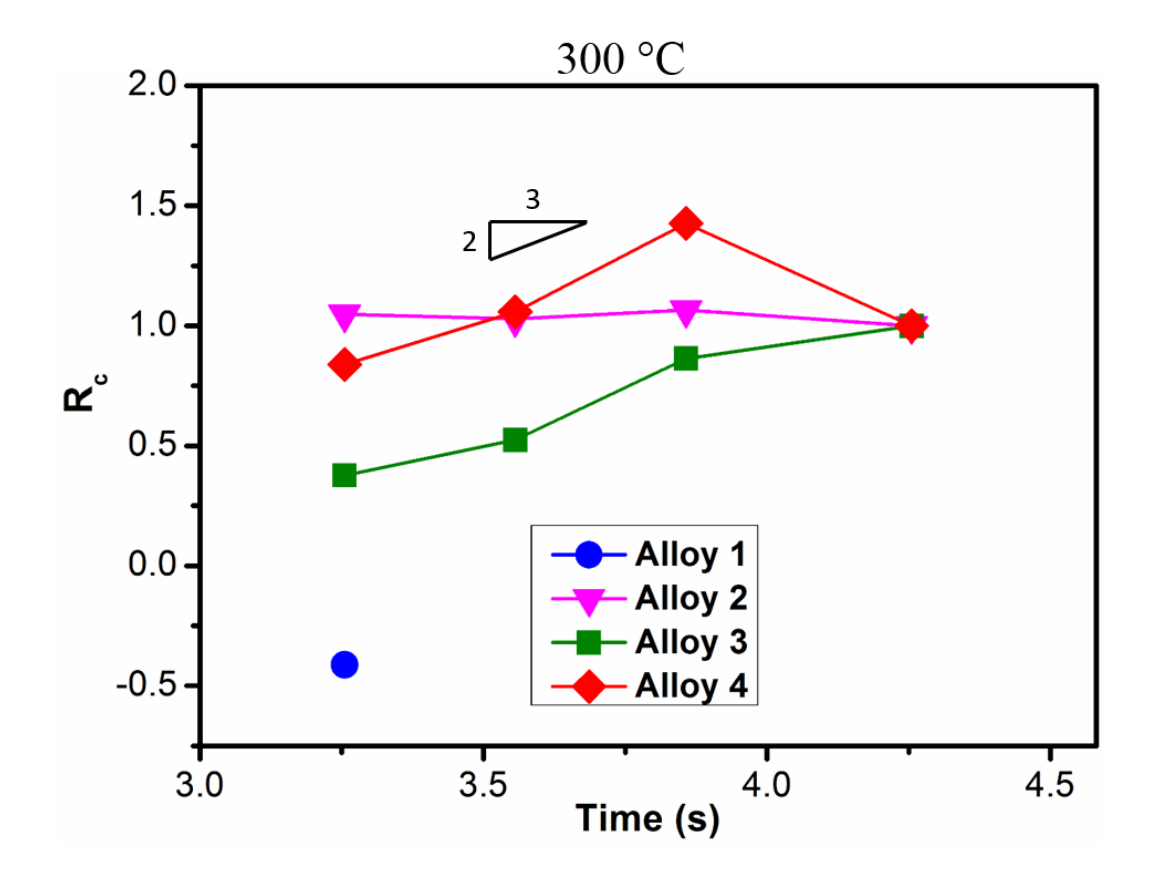


Figure 5-8 the fractional change in hardness as a function of time at 300 °C

As we have observed hardness increases on annealing at 300 °C, the magnitude of hardness increase varied with different pearlite fractions (alloy chemistry) and soaking time. Hardness varying with pearlite content will be addressed and further insights will be present in section 5.4.2. Here this section will only deal with Hardness varying with soaking time. It is reported by the present authors [8] that the hardness of alloy 3 increases due to Cottrell formation. The detailed mechanism of Cottrell formation in next section 5.4.2. To show the atomistic interaction mechanisms responsible for such hardness increase behavior hardness results are deduced to Cottrell and Bilby equation [30].

Cottrell formation is given by

$$\frac{N(t)}{N_c} = \frac{3}{2} n_o \lambda V_{dis} t^{2/3},\tag{1}$$

where N(t) is the number of carbon atoms per unit volume diffusing to dislocations during a time duration of t, N_s is the dislocation density, n_o is the initial carbon concentration, λ is the slip distance, $V_{dis} = 2(\pi/2)^{1/3}(AD/KT)^{2/3}$ with D being the diffusion coefficient of carbon in ferrite, k the Boltzmann constant, A the parameter for the magnitude of the interaction between carbon and dislocation and T the absolute temperature. It may be noted that the above equation is a simple model mostly applicable during the early stages of Cottrell atmosphere formation and has several assumptions as detailed in Zhao et al, However, for a first order estimate, the degree of Cottrell atmosphere formation at a given temperature, alloy chemistry and dislocation density, is found to be proportional to a time exponent of 2/3. Cottrell and Bilby [33] also proposed that the degree of atmosphere formation given by Eq. (1), can be assumed to be proportional to the fractional change in hardness (R_c), i.e.,

$$R_c = \frac{H_t - H_o}{H_m - H_o} \propto \frac{N(t)}{N_S},\tag{2}$$

where H_t is the hardness after annealing treatment for a specified time, H_o is the initial hardness, and H_m is the maximum hardness change after prolonged treatment. From Eq. (1) and Eq. (2) it can be observed that the fractional change in hardness is proportional to a time exponent of 2/3 for a given alloy.

Using Eq (1), the applicability of the Cottrell kinetics was assessed by plotting the fractional change in the hardness as a function of time in the log-log plot as shown in Figure.5-8. As it can be seen that alloys 3 and 4 obey with reasonable accuracy the linear behavior with a slope close to 2/3 on the log-log plot, indicating that Cottrell formation might be the dominant mechanism. Interestingly, alloy 2 does not follow such behavior. Though hardness increases in alloy 2, the kinetics do not follow the Cottrell kinetics; the reason for this will be discussed in section 4.2. Literature report [31,32] shows that the $t^{2/3}$ exponent is attributed to Cottrell formation by carbon pinning the dislocation. AK De et al. [31,33] has reported that any deviation from 2/3 is generally associated with a change in the precipitation mechanism of carbon on dislocation or in the matrix; cf. infra section 5.4.2.

5.4.2 Role of pearlite on recovery kinetics at 300 °C.

As we have observed hardness increases due to Cottrell formation, to further see what mechanisms drive those kinetics? To address this issue, we have obtained deconvoluted data from nanoindentation as shown in Figure. 5-7. The average hardness was plotted as a function of pearlite fraction as shown in Figure. 5-9 (a-b) for both ferrite and pearlite, whereby the pearlite fractions were obtained from table 3.1. In the cold rolled condition as shown in Figure. 5-9(a-b), the hardness of the bulk ferrite is independent of pearlite fraction with almost near zero slope as expected. Conversely, the pearlite hardness increases with increasing pearlite area fraction [34]. In contrast, during annealing at 300 °C for 30 min, alloy 1 remains similar

to the cold rolled state, whereas, in alloy 2, alloy 3/4 the hardness of ferrite and pearlite increases from cold rolled state and hardness increases with increasing pearlite fraction. These results suggest pearlite is playing a major role in hardness kinetics and the magnitude of hardness increase also depends on the pearlite fraction. Interestingly, in alloy 1 the hardness remains similar to the cold rolled state, whereby also the KAM distribution remains similar to cold rolled state, cf. Figure. 5-3. This indicates that in the absence of a pearlite phase the ferrite matrix remains invariant after annealing treatment. In pearlite alloy 2-4, results suggest that hardness increases both in ferrite and pearlite. The KAM distribution in Figure.5-3 shows a slight shift in KAM value towards the right side indicating hardening in presence of pearlite. The TEM analysis as shown in Figure 9(e) unveils that in pearlite the cementite appears diffused and causes thinning, but a high amount of dislocations is still retained. During annealing, cementite redissolves in pearlite by the cementite-dislocation interaction mechanism, where dissolution /or dissociation of carbon from cementite takes place and causes diffused appearance. The binding energy of the carbon atom and dislocation in the ferrite phases is higher than between the carbon and iron atoms in cementite [14,35,36]. The dissociation or dissolution of carbon from cementite locks the dislocations and leads to Cottrell formation in both bulk ferrite and pearlite, causing a hardness increase as reported by the author elsewhere [8,36].

However, in ferrite TEM analysis in Figure. 5-4(b) rearrangement of dislocation into causes sharpening of cell/sub boundaries during annealing is observed as a typical recovery signature on annealing. Whereas nanoindentation map and hardness histogram show hardness increase in ferrite as in Figures. 5-6 and 5-7. These results suggest that concurrently recovery by dislocation rearrangement and Cottrell takes place in ferrite, where Cottrell is more dominant.

These changes might be causing a slight increase and shift in the distribution of KAM in ferrite and pearlite in Figure 5-3. De Jeer et al. [37] Have observed a similar kind of increase in misorientation and shift towards the higher value during tempering of stainless steel. The explanation for increased misorientation is due to recovery taking place in bulk and dislocations glide and escape to the surface either locked by carbon or piled up at the subsurface.

The present results in Figure 5-9(a-b) in the case of alloy 2-4, the hardness increases with an increase in pearlite fraction. These results attribute that increasing the pearlite fraction might have led to a higher amount of carbon dissolution from cementite and caused to increase in carbon content on dislocation in pearlite ferrite and bulk ferrite causing a higher hardness increase. Gridney et al. [36] reported that cementite dissolution and blocking of dislocation decide the extent of mechanical property of cold-rolled steels. The present results are in good agreement with that. Also, in pearlitic steels, it is well reported that increased carbon content in pearlitic ferrite causes solid solution hardening and thus is contributing to an increase in strength [13,38]. The present results are in good agreement with the literature [13,38], whereby Cottrell atmosphere formation is added by an increase in carbon content is leading to solid solution hardening. The presence of a higher amount of solute in pearlitic ferrite, and ferrite in alloy 3/4 in comparison to alloy 2 might be the reason for the higher hardness increase. In alloy 2, due to the presence of less amount of pearlite(8%) and also microalloying element Nb, which has higher affinitive towards carbon, it might reduce the amount of carbon in solution [39] might have caused less hardness increase in comparison to alloy 3/4. Also, the presence of Nb might have caused the deviation in $t^{2/3}$ Cottrell kinetics in alloy 2.

In alloy 3/4 with an increasing soaking time, the present results TEM analysis Figure.5-4, in both ferrite and pearlite show a higher amount of dislocation are still retained after annealing at 300 °C for 300 min. However, in pearlite in Figure. 5-4(d-f) shows cementite starts diffusing and causes thinning. Whereas in ferrite, increasing soaking time carbon clustering/precipitation in ferrite observed as shown in Figure 5-4(c). These results attribute that carbon diffused from cementite might cluster and grow preferentially along with the dislocation as these provide a path for rapid diffusion and consequently cause clustering/precipitation in ferrite causing to increase in hardness and follow $t^{2/3}$ kinetics. These results are in good agreement with the results reported in DP steels during bake hardening where in that case additional carbon in ferrite is being supplied by the tempering of martensite [32].

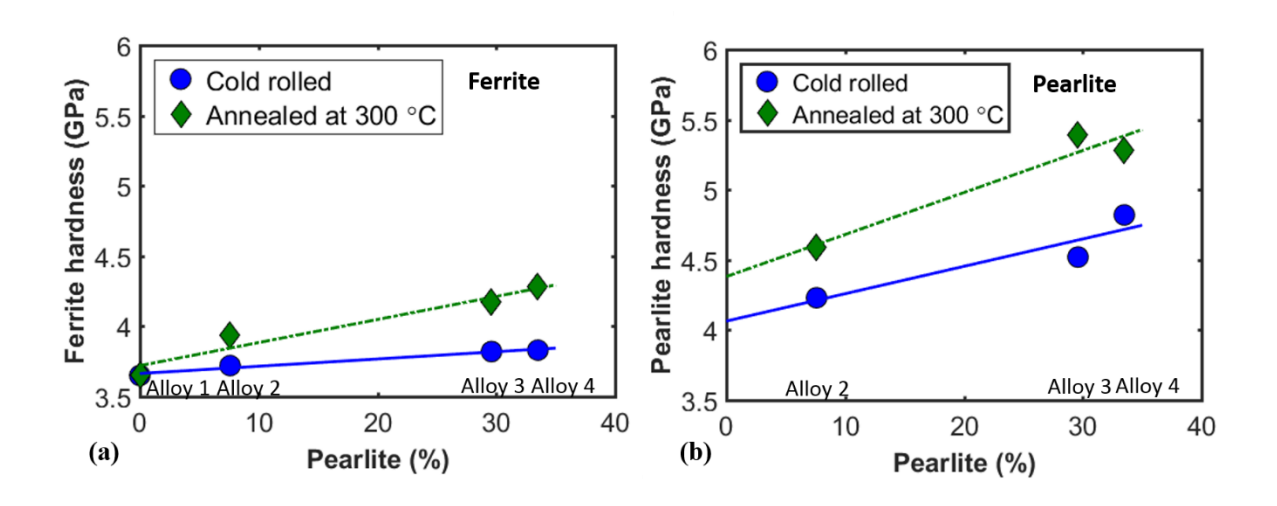


Figure 5-9 Hardness in (a) bulk ferrite and (b) pearlite as a function of pearlite fraction after cold rolling and recovery annealing at 300 °C for 30 min

5.5 Summary and conclusions

The present chapter focuses on early recovery kinetics of 80% cold-rolled steel sheets consisting of ferrite-pearlite in three different AHSS in comparison to alloy 1 consisting of only ferrite. Mainly pearlite fraction and its distribution were varied to investigate the role of

pearlite at annealing temperatures 300 °C for various soaking times. In the single ferrite phase, alloy 1 recovery slow and sluggish recovery takes place at 300 °C. Whereas in the presence of pearlite in alloy 2, alloy 3/4 shows hardness increase kinetics at 300 °C. Using complementary techniques such as nanoindentation and electron microscopy with EBSD and TEM gave a better understanding and insights on the driving force for recovery kinetics. The reasons for the same are well summarized and the following conclusions can be drawn:

- 1. In alloy 1 consisting of the single ferrite phase, MHv shows hardness decreases indicating recovery, and further confirmed by KAM maps
- 2. Whereas the presence of pearlite in alloy 2, alloy 3, and alloy 4, shows a hardness increase from cold rolled condition at 300 °C. Hardness increases, varied with pearlite fraction and soaking time. In alloy 2, hardness increases and saturates with time. In alloys, 3-4 hardness increases with increasing time.
- Nanoindentation mapping and histograms confirm hardness increases in ferrite and pearlite
- 4. KAM maps and distribution in alloy 2-4, show a slight increase in misorientation in both ferrite and pearlite.
- 5. TEM results in alloy 3, reveal that in ferrite phases, sharpening of cell/sub boundaries due to rearrangements of dislocation and with increasing soaking time clustering of carbon/carbides on sub boundaries. In pearlite thinning of cementite is observed with increasing soaking time.

- 6. Hardness increases from cold rolled condition due to the dissolution of carbon from cementite leading to Cottrell formation in both ferrite and pearlite phases as confirmed by Nanoindentation mapping and hardness histograms.
- 7. Hardness increases with soaking time were modeled using the Cottrell equation and the kinetics suggest in alloy 3, and alloy 4 consisting of higher pearlite fraction and banded distribution follow $t^{2/3}$ the Cottrell kinetics. Whereas alloy 2, deviates from $t^{2/3}$ Cottrell kinetics.
- 8. In alloy 2, the deviation of $t^{2/3}$ kinetics might be due to the lower area fraction of pearlite and also due to the presence of microalloying elements Nb.
- 9. In alloys 3 and alloy 4, the presence of a higher fraction of pearlite, continuous dissolution of carbon from cementite promotes clustering of carbon/carbides on dislocation and follow $t^{2/3}$ Cottrell kinetics
- 10. On annealing at 300 °C, hardness increase kinetics is mainly driven by pearlite fraction.
- 11. An increase in pearlite fraction increases, an increase in the amount of free carbon available for Cottrell formation and consequently leads to an increase in the solute content on dislocation causing the higher amount of hardness increase in both ferrite and pearlite.
- 12. On annealing at 300 °C, dislocation rearrangement leading to a sharpening of cell boundaries in ferrite was observed from TEM investigation. However, nanoindentation maps show a hardness increase. Suggesting that concurrently recovery by dislocation rearrangement and Cottrell formation takes place, Cottrell being more dominant and causing hardness increase in alloys 2-4.

References

- [1] J. Teixeira, M. Moreno, S.Y.P. Allain, C. Oberbillig, G. Geandier, F. Bonnet, Intercritical annealing of cold-rolled ferrite-pearlite steel: Microstructure evolutions and phase transformation kinetics, Acta Mater. 212 (2021). https://doi.org/10.1016/j.actamat.2021.116920.
- [2] C. Zheng, D. Raabe, Interaction between recrystallization and phase transformation during intercritical annealing in a cold-rolled dual-phase steel: A cellular automaton model, Acta Mater. 61 (2013) 5504–5517. https://doi.org/10.1016/j.actamat.2013.05.040.
- [3] M. Calcagnotto, Y. Adachi, D. Ponge, D. Raabe, Deformation and fracture mechanisms in fine- and ultrafine-grained ferrite/martensite dual-phase steels and the effect of aging, Acta Mater. 59 (2011) 658–670. https://doi.org/10.1016/j.actamat.2010.10.002.
- [4] N. Peranio, Y.J. Li, F. Roters, D. Raabe, Microstructure and texture evolution in dual-phase steels: Competition between recovery, recrystallization, and phase transformation, Mater. Sci. Eng. A. 527 (2010) 4161–4168. https://doi.org/10.1016/j.msea.2010.03.028.
- [5] M. Soleimani, A. Kalhor, H. Mirzadeh, Transformation-induced plasticity (TRIP) in advanced steels: A review, Mater. Sci. Eng. A. 795 (2020). https://doi.org/10.1016/j.msea.2020.140023.
- [6] C.C. Tasan, M. Diehl, D. Yan, M. Bechtold, F. Roters, L. Schemmann, C. Zheng, N. Peranio, D. Ponge, M. Koyama, K. Tsuzaki, D. Raabe, An Overview of Dual-Phase Steels: Advances in Microstructure-Oriented Processing and Micromechanically Guided Design, Annu. Rev. Mater. Res. 45 (2015) 391–431. https://doi.org/10.1146/annurev-matsci-070214-021103.
- [7] S. Janakiram, J. Gautam, L.A.I. Kestens, Effect of pearlite morphology on recrystallization behaviour in cold rolled high strength automotive steel sheets, J. Phys. Conf. Ser. 1270 (2019). https://doi.org/10.1088/1742-6596/1270/1/012015.
- [8] S. Janakiram, P.S. Phani, G. Ummethala, S.K. Malladi, J. Gautam, L.A.I. Kestens, New insights on recovery and early recrystallization of ferrite-pearlite banded cold rolled high strength steels by high speed nanoindentation mapping, Scr. Mater. 194 (2021) 113676. https://doi.org/10.1016/j.scriptamat.2020.113676.
- [9] S. Janakiram, J. Gautam, P.S. Phani, L.A.I. Kestens, Microstructural and micro hardness variation during low temperature recovery annealing in C-Mn high strength Steels, in: J. Phys.

- Conf. Ser., 2019. https://doi.org/10.1088/1742-6596/1270/1/012017.
- [10] A. Martínez-de-Guerenu, F. Arizti, M. Díaz-Fuentes, I. Gutiérrez, Recovery during annealing in a cold rolled low carbon steel. Part I: Kinetics and microstructural characterization, Acta Mater. 52 (2004) 3657–3664. https://doi.org/10.1016/j.actamat.2004.04.019.
- [11] S. Dutta, A.K. Panda, A. Mitra, S. Chatterjee, R.K. Roy, Microstructural evolution, recovery and recrystallization kinetics of isothermally annealed ultra low carbon steel Microstructural evolution, recovery and recrystallization kinetics of isothermally annealed ultra low carbon steel, (2020).
- [12] Y.Z. Chen, G. Csiszár, J. Cizek, X.H. Shi, C. Borchers, Y.J. Li, F. Liu, R. Kirchheim, Defect Recovery in Severely Deformed Ferrite Lamellae During Annealing and Its Impact on the Softening of Cold-Drawn Pearlitic Steel Wires, Metall. Mater. Trans. A Phys. Metall. Mater. Sci. 47 (2016) 726–738. https://doi.org/10.1007/s11661-015-3263-z.
- [13] J. Takahashi, M. Kosaka, K. Kawakami, T. Tarui, Change in carbon state by low-temperature aging in heavily drawn pearlitic steel wires, Acta Mater. 60 (2012) 387–395. https://doi.org/10.1016/j.actamat.2011.09.014.
- [14] Y.J. Li, P. Choi, S. Goto, C. Borchers, D. Raabe, R. Kirchheim, Evolution of strength and microstructure during annealing of heavily cold-drawn 6.3 GPa hypereutectoid pearlitic steel wire, Acta Mater. 60 (2012) 4005–4016. https://doi.org/10.1016/j.actamat.2012.03.006.
- [15] A. Smith, H. Luo, D.N. Hanlon, J. Sietsma, S. Van Der Zwaag, Recovery processes in the ferrite phase in C-Mn steel, ISIJ Int. 44 (2004) 1188–1194. https://doi.org/10.2355/isijinternational.44.1188.
- [16] R.K. Ray, B. Hutchinson, C. Ghosh, "Back-annealing" of cold rolled steels through recovery and/or partial recrystallisation, Int. Mater. Rev. 56 (2011) 73–97. https://doi.org/10.1179/095066010X12646898728444.
- [17] D. Raabe, Recovery and Recrystallization: Phenomena, Physics, Models, Simulation, Fifth Edit, Elsevier B.V., 2014. https://doi.org/10.1016/B978-0-444-53770-6.00023-X.
- [18] Influence of Cold Drawing, (2006) 1–10.
- [19] B. Kim, D. San-Martin, P.E.J. Rivera-Díaz-del-Castillo, Modelling recovery kinetics in high-strength martensitic steels, Philos. Mag. Lett. 97 (2017) 280–286. https://doi.org/10.1080/09500839.2017.1342048.
- [20] L. Backe, Modeling the effect of solute drag on recovery and recrystallization during hot

- deformation of Nb microalloyed steels, ISIJ Int. 50 (2010) 239–247. https://doi.org/10.2355/isijinternational.50.239.
- [21] F.J. Humphreys, M. Hatherly, Chapter 6 RECOVERY AFTER, Recryst. Relat. Annealing Phenom. (1963) 211–213.
- [22] J.P. Ferrer, T. De Cock, C. Capdevila, F. García Caballero, C. García de Andrés, Comparison of the annealing behaviour between cold and warm rolled ELC steels by thermoelectric power measurements, Acta Mater. 55 (2007) 2075–2083. https://doi.org/10.1016/j.actamat.2006.11.010.
- [23] S. Takaki, J. Fuss, H. Kugler, U. Dedek, H. Schultz, Resistivity Recovery of High Purity and Carbon Doped Iron Following Low Temperature Electron Irradiation., Radiat. Eff. 79 (1983) 87–122. https://doi.org/10.1080/00337578308207398.
- [24] S. Dutta, V. Rajinikanth, A.K. Panda, A. Mitra, S. Chatterjee, R.K. Roy, Effect of Annealing Treatment on Mechanical and Magnetic Softening Behaviors of Cold Rolled Interstitial-Free Steel, J. Mater. Eng. Perform. 28 (2019) 2228–2236. https://doi.org/10.1007/s11665-019-03953-z.
- [25] J. Gautam, A. Miroux, J. Moerman, L. Kestens, TNR dependent hot rolling microstructure and texture development in c-Mn dual phase and HSLA steels, Defect Diffus. Forum. 391 (2019) 120–127. https://doi.org/10.4028/www.scientific.net/DDF.391.120.
- [26] J. Wu, P.J. Wray, C.I. Garcia, M. Hua, A.J. Deardo, Image quality analysis: A new method of characterizing microstructures, ISIJ Int. 45 (2005) 254–262. https://doi.org/10.2355/isijinternational.45.254.
- [27] P. Sudharshan Phani, W.C. Oliver, A critical assessment of the effect of indentation spacing on the measurement of hardness and modulus using instrumented indentation testing, Mater. Des. 164 (2019) 1–10. https://doi.org/10.1016/j.matdes.2018.107563.
- [28] S. Janakiram, J. Gautam, P.S. Phani, L.A.I. Kestens, Microstructural and micro hardness variation during low temperature recovery annealing in C-Mn high strength Steels, J. Phys. Conf. Ser. 1270 (2019). https://doi.org/10.1088/1742-6596/1270/1/012017.
- [29] E.A. Ariza-Echeverri, M. Masoumi, A.S. Nishikawa, D.H. Mesa, A.E. Marquez-Rossy, A.P. Tschiptschin, Development of a new generation of quench and partitioning steels: Influence of processing parameters on texture, nanoindentation, and mechanical properties, Mater. Des. 186 (2020) 108329. https://doi.org/10.1016/j.matdes.2019.108329.

- [30] A.H. Cottrell, B.A. Bilby, Dislocation theory of yielding and strain ageing of iron, Proc. Phys. Soc. Sect. A. 62 (1949) 49–62. https://doi.org/10.1088/0370-1298/62/1/308.
- [31] A.K. De, B.C. De Cooman, S. Vandeputte, Kinetics of strain aging in bake hardening ultra low carbon steel-a comparison with low carbon steel, J. Mater. Eng. Perform. 10 (2001) 567–575. https://doi.org/10.1361/105994901770344719.
- [32] T. Waterschoot, B.C. De Cooman, A.K. De, S. Vandeputte, Static strain aging phenomena in cold-rolled dual-phase steels, Metall. Mater. Trans. A. 34 (2003) 781–791. https://doi.org/10.1007/s11661-003-0113-1.
- [33] A.K. De, S. Vandeputte, B.C. De Cooman, Kinetics of low temperature precipitation in a ULC-bake hardening steel, Scr. Mater. 44 (2001) 695–700. https://doi.org/10.1016/S1359-6462(00)00638-2.
- [34] T. Takahashi, D. Ponge, D. Raabe, Investigation of orientation gradients in pearlite in hypoeutectoid steel by use of orientation imaging microscopy, Steel Res. Int. 78 (2007) 38–44. https://doi.org/10.1002/srin.200705857.
- [35] J. Takahashi, M. Kosaka, K. Kawakami, T. Tarui, Change in carbon state by low-temperature aging in heavily drawn pearlitic steel wires, Acta Mater. 60 (2012) 387–395. https://doi.org/10.1016/j.actamat.2011.09.014.
- [36] N, Mossbauer Effect in Deformed Fe-C Alloys, 201 (1975) 201–210.
- [37] L.T.H. De Jeer, V. Ocelík, J.T.M. De Hosson, Dynamics of tempering processes in stainless steel, WIT Trans. Eng. Sci. 116 (2017) 187–193. https://doi.org/10.2495/MC170191.
- [38] Y.J. Li, P. Choi, C. Borchers, S. Westerkamp, S. Goto, D. Raabe, R. Kirchheim, Atomic-scale mechanisms of deformation-induced cementite decomposition in pearlite, Acta Mater. 59 (2011) 3965–3977. https://doi.org/10.1016/j.actamat.2011.03.022.
- [39] L.M. Storozheva, K. Éscher, R. Bode, K. Hulka, D.A. Burko, Effect of niobium and coiling and annealing temperatures on the microstructure, mechanical properties, and bake hardening of ultralow-carbon steels for the automotive industry, Met. Sci. Heat Treat. 44 (2002) 102–107. https://doi.org/10.1023/A:1019666003371.

Chapter 6

Recovery kinetics at 500 °C

6

In this chapter, we investigate the role of pearlite on static recovery kinetics of 80% cold-rolled steels sheets at annealing temperatures at 500 °C. As a part of thermomechanical processing, all the steel sheets were cold rolled to 80% followed by an annealing process in the recovery regime at 500 °C. We have chosen steels with varying carbon content, resulting in different compositions of the pearlite. Certain minor modifications to the composition also resulted in minor changes in the morphology of pearlite. In addition to this, we have also selected a ULC steel that is composed of single phase ferrite without pearlite. These aspects provide a good platform to systematically explore the effect of pearlite on the early recovery kinetics during thermomechanical processing, i.e. in the recovery stages of the annealing treatment.

6.1 Introduction

Recovery in ferrite containing steels, like ELC [1] and ULC [2] has been well studied. In ELC steels [1] it reported that above 500 °C, hardness significantly drops. Coercive filed Hc shows important drop for short annealing time in the temperature range 450-500 °C. Followed by a continuous decrease with over time and saturation. Microstructural investigation revealed that in γ fiber sharpening of the cell boundaries and evolving into a subgrain structure [1].in ULC steels [2] hardness measurements and microstructural investigation revealed that recrystallization dominates from 550,580 and 600 °C. The recovery and recrystallization of

stored energy follow the progress of softening by increasing high angle boundary and decreasing KAM value with ($< 1^{\circ}$) [2].

Recovery in fully pearlitic steels ultra-high strength steels(UHSS) [3–5] the presence of cementite complicates the recovery of ferrite. Prior work suggests in pearlitic steels [3], At temperatures above 250 °C, the combined effect of dislocation recovery and cementite spherodization causes pronounced softening by coarsening of the dislocation substructure. In C-Mn steels [6] the recovery of ferrite is explored, and it was discovered that activation energy and activation volume for the recovery process change with temperature, but not with strain and strain rate. Activation energy is near to lattice self-diffusion at higher temperatures (450-600 °C). However, what mechanism drives such recovery and their associated microstructural changes in individual phases with varying pearlite is not addressed

6.2 Experimental procedure:

6.2.1 Composition and processing:

Table 3.1 in chapter 3 lists the composition of four different steel sheets with varying C-Mn content used in the present study. All the four cold rolled steel sheets were recovery annealed in a muffle furnace at 500 °C for 30, 60, 120, 300 minutes of soaking time, followed by furnace cooling till room temperature. Mechanical polishing was carried out on SiC papers, followed by coarse alumina polishing and vibratory polishing for 8 hr with fine colloidal silica of 50 nm.

6.2.2 Characterization and mechanical testing:

Microstructural characterization was carried out on High-resolution EBSD mapping was performed with an SEM of type FEI NOVA NANOSEM 450, with an accelerating voltage of 20 kV, at a working distance of 15mm and step size 80 nm with a hexagonal grid on 26 μm x 26 μm area. Kernel average misorientation (KAM), obtained from EBSD was used to measure

the local misorientation at the subgrain scale in ferrite and pearlite. TEM observations were carried out on JEOL 2100 with a focus on the ferrite and pearlite region in the cold rolled and annealed at 500°C for 30, 300 min samples.

Mechanical testing was carried out using a micro Vickers hardness tester on all annealed at 500°C for different soaking times (30,60,120,300 min). Whereas nanoindentation mapping was carried out only on 30 min of soaking time sample. The parameters used for mechanical testing are described in detail in chapter 3.

6.3 Results

6.3.1 Microstructural evolution with SEM

The microstructural changes on annealing at 500°C for 30, 60, 120, 300 min of soaking time in four different alloys are shown in Figure. 6-1. In Alloy 1, recrystallization of ferrite takes after 30 min of soaking time, as indicated by the circle in Figure 6-1(a) and continues to increase with an increase in soaking time. In alloy 2 and alloy 3, for the first 30 min of soaking time, but with an increase in soaking time, the cementite in pearlite undergoes fragmentation induced spherodization and continues to spherodized with soaking time. After 300 min of soaking time, ferrite retains its cold rolled structure and cementite in pearlite completely spherodizes. In alloy 4, the lamellar cementite structure spheroidizes inside the pearlite colonies from the first 30 min soaking time and continues with an increase in time. In ferrite, at 300 min it was observed that the coarsening of ferrite grains takes place as indicated by the blue dotted arrow.

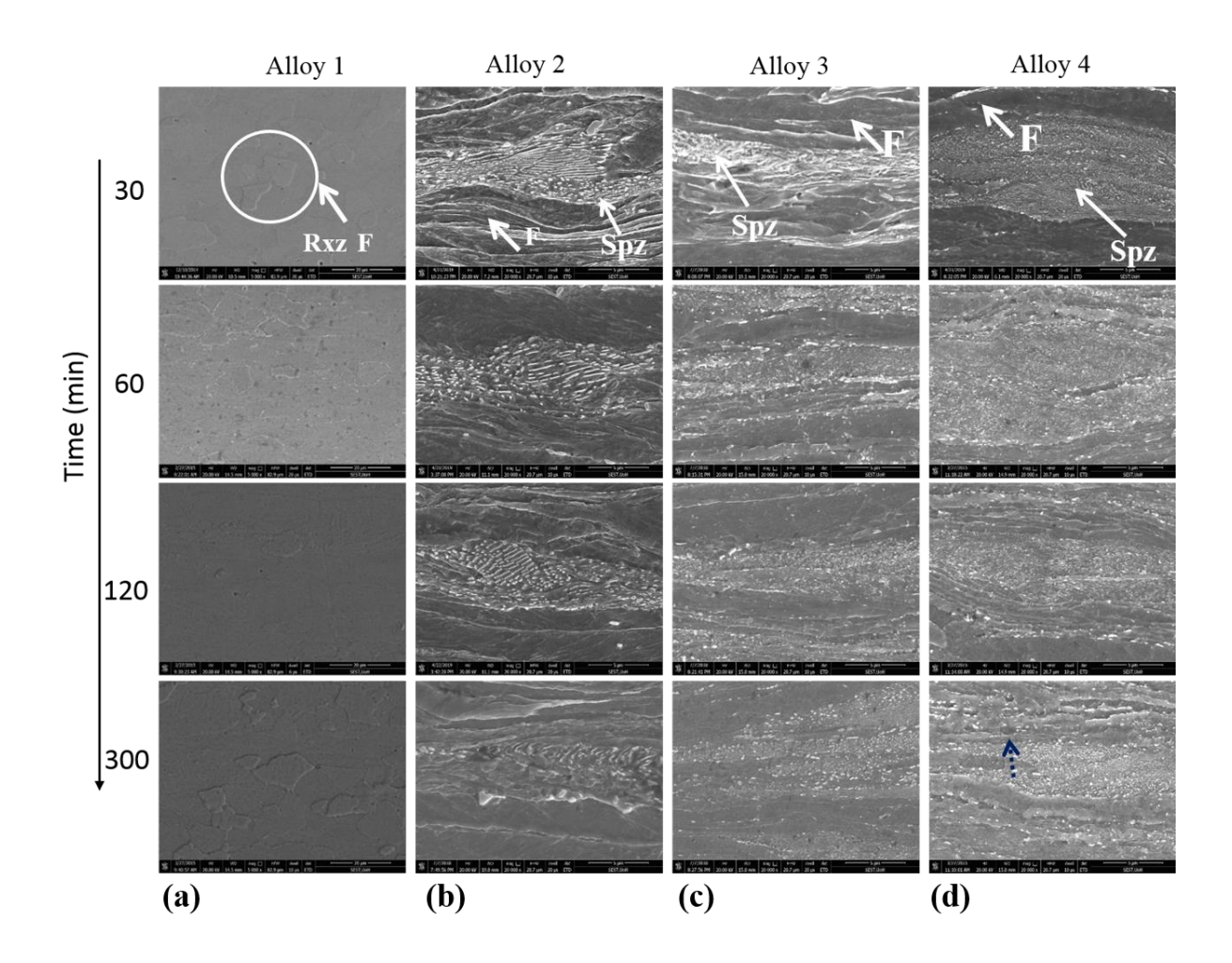


Figure 6-1 SEM microstructural changes after recovery annealing at 300° for 30, 60,120 and 300 min of soaking time in (a) Alloy 1, and ferrite pearlite phases, (b) Alloy 2, (c) Alloy 3 (d) Alloy 4 [8] F-ferrite,

6.3.2 Kernel average misorientation (KAM) evolution

To further provide microstructural insights at the substructure level, we will look into the KAM maps obtained from EBSD on annealing at a temperature of 500 °C in all four alloys as shown in Figure 6-2(a-d).

In alloy 1, the KAM map as in Figure 6-2(a) shows the blue colored region that appears causing to decrease in KAM misorientation and is an indication of significant recovery and onset of ferrite recrystallization. With increasing soaking time, the fraction of the blue colored region

increases as shown in the KAM map in Figure. 6-2(a) indicating an increase in the fraction of recrystallized ferrite grains. Contrastingly, in alloy 2-4, the KAM map in Figure 6.2(b-d) still reveals the presence of deformed grains. The KAM map shows an increase in green-bluish regions in ferrite and pearlite which suggest a misorientation decrease and the onset of the recovery process and continues to increase with soaking time. On further increasing the soaking time up to 300 min in alloy 3-4, the KAM map shows the blue strain-free region in ferrite, attributed to the growth of subgrain and an expansion of green colored regions showing a further decrease in misorientation in Figure. 6-2 (c-d). However, such changes were absent in alloy 2.

In summary, on annealing at 500 °C significant differences and sub-structural changes such as partial recrystallization and recovery of ferrite in alloy 1. Whereas in alloys 2-4, in ferrite, sub grain coarsening and a decrease in misorientation in ferrite and pearlite are observed.

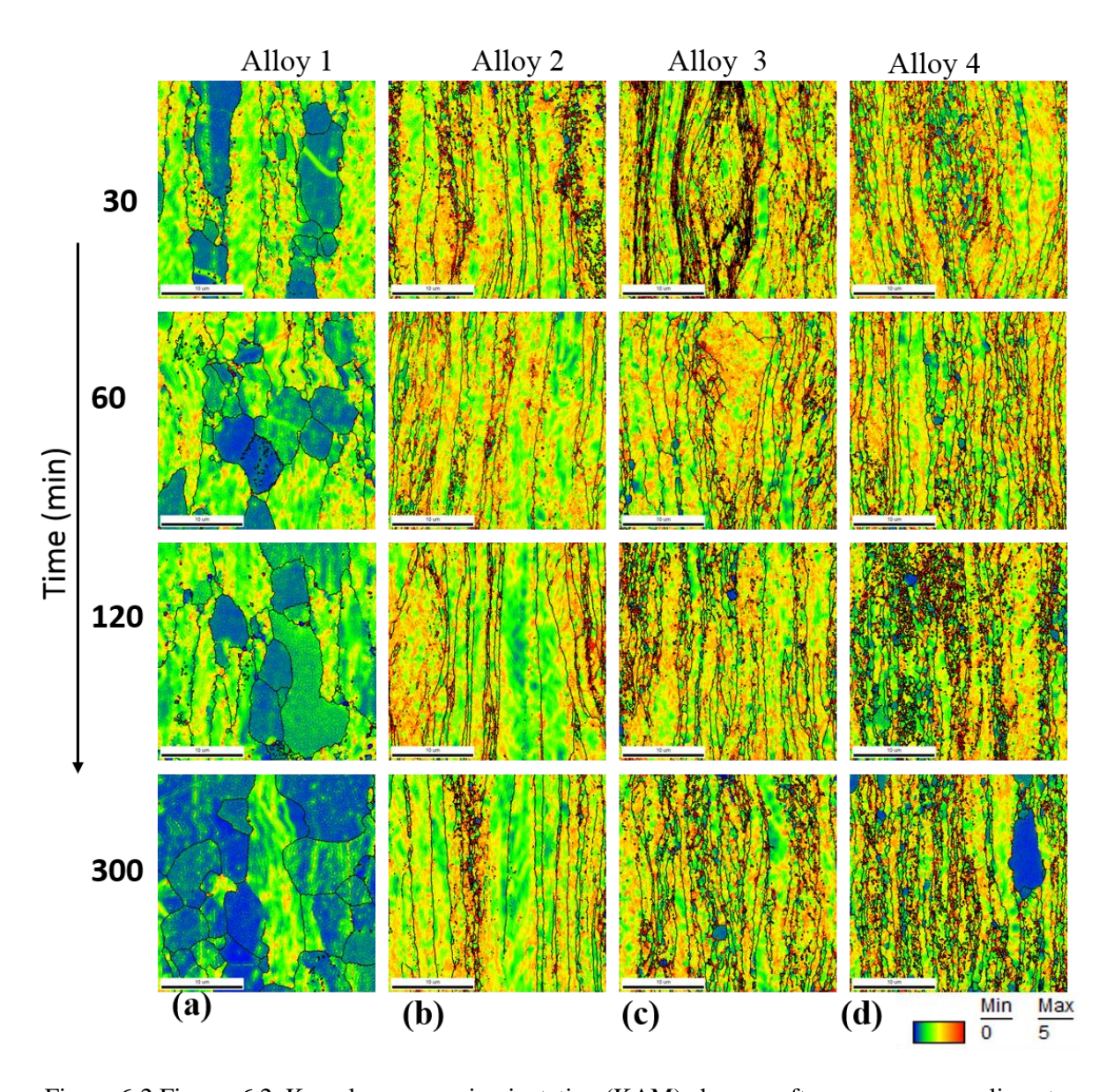


Figure 6-2 Figure. 6.2. Kernel average misorientation (KAM) changes after recovery annealing at 300° for 30, 60,120 and 300 min of soaking time in (a) Alloy 1, and ferrite pearlite phases, (b) Alloy 2, (c) Alloy 3 (d) Alloy 4

6.3.3 KAM distribution of ferrite and pearlite

The changes in KAM distribution from cold rolled to recovery annealed condition at 500 °C for 30, 60, 120 and 300 min soaking are shown in Figure. 6-3 for all four alloys. In the ferrite alloy 1, the KAM distribution shows a significant shift towards a lower KAM value with the increase in soaking time. This significant shift is mainly due to partial recrystallization of

ferrite grains as shown in Figure 6-2. The recrystallized volume fraction extends with increasing soaking time which produces a further decrease of KAM values. For alloys 2, 3 and 4, in contrast to alloy 1, after annealing of 30 min the KAM distribution of the ferrite phase remains similar to the cold rolled state. Upon further increasing the soaking time the KAM distribution of the ferrite phase slightly starts shifting towards the lower values indicative of recovery. The recovery process is slower in alloy 3 compared to alloys 2 and 4.

For the pearlite phase of alloys 2, 3 and 4, the KAM distributions remain similar to the ones observed after the recovery annealing at 300 °C, suggesting that recovery is still more retarded in the pearlitic ferrite as compared to bulk ferrite. In alloy 3 and alloy 4 slowly with increases in time at 300 min and 120-300 min respectively KAM distribution shits towards lower KAM values indicating a recovery process.

In summary, alloy 1 undergoes partial recrystallization and hence the KAM distribution significantly shifts towards the lower values. Conversely, in alloys 2, 3 and 4, the ferrite phase KAM distribution remains similar to cold rolled state at the first 30 min and then slightly shifts towards a lower KAM value indicating a recovery in ferrite. In the pearlite phase, the KAM distribution remains similar to the distribution observed after recovery annealing at 300 °C and not much change has been observed in alloy 2 indicating the recovery is further retarded at 500 °C, whereas in alloy 3/4, KAM distribution shifts towards a lower value at 120-300 min of soaking time indicating a recovery in pearlitic ferrite.

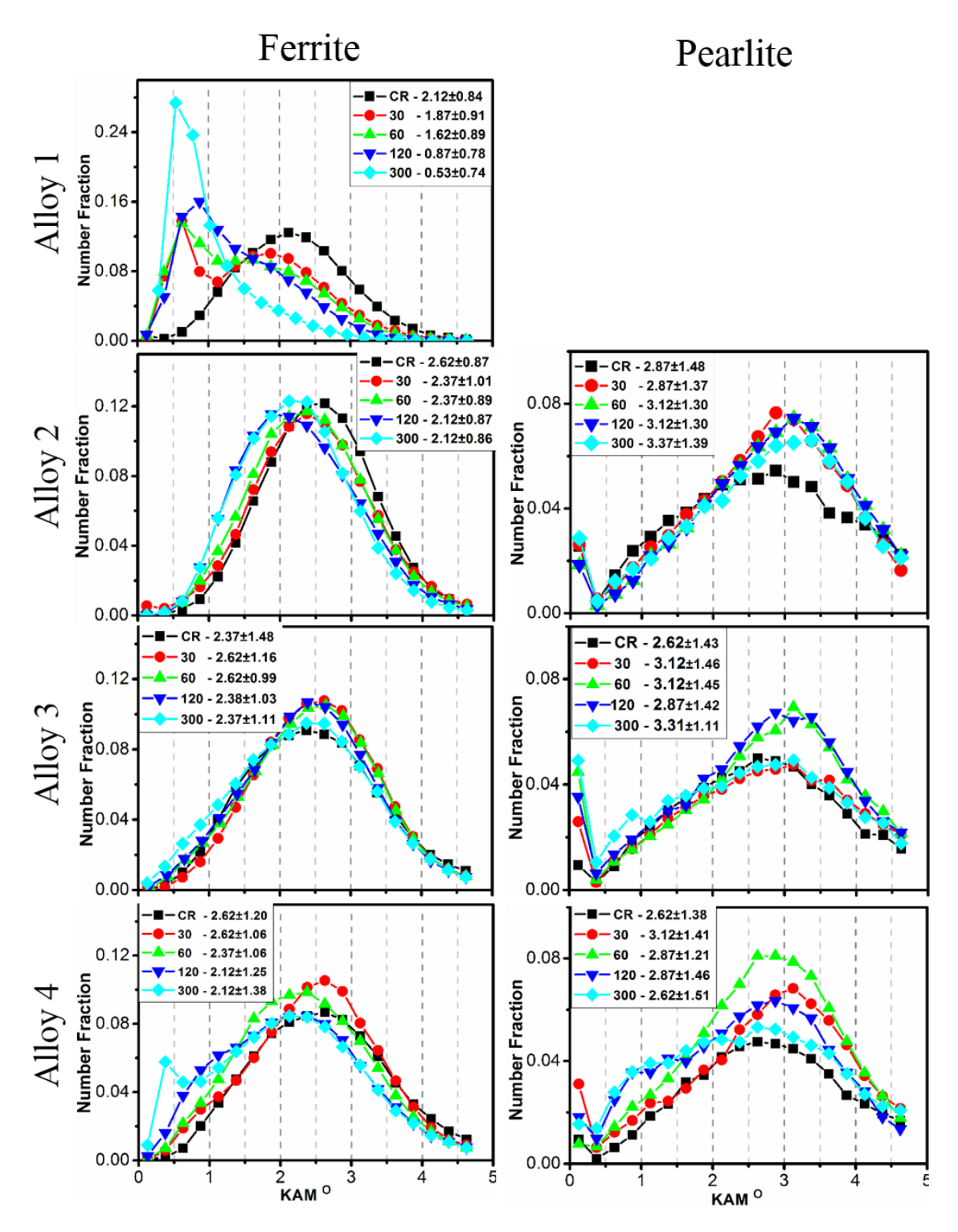


Figure 6-3 Kernel average misorientation (KAM) distribution of ferrite and pearlite from cold rolled to recovery annealed at $300\,^{\circ}\text{C}$ at a different soaking time in alloy 1, alloy 2, alloy 3, and alloy 4

6.3.4 TEM analysis

TEM micrographs show microstructural evolution from cold rolled to recovery annealed at 500 °C in both ferrite Figure 6-4(a-c) and pearlite Figure 6-4(d-f). Upon annealing for 30 min in ferrite as in Figure 6-4(b) shows annihilation of dislocation inside the sub boundaries, however, the dislocations are still present at sub boundaries. Also, fine carbides are present inside and on sub boundaries as indicated by an arrow. Increasing the soaking time to 300 min shows a decrease in dislocation at sub boundaries and the presence of fine carbides still pinning these sub boundaries as indicated with a dotted arrow in Figure 6-4(c). In the case of pearlite, on annealing for 30 min cementite gets fragmented and dislocation starts to decrease in pearlitic ferrite as shown in Figure 6-4(e). Further increasing the soaking time to 300 min cementite is completely replaced by fine particles indicating fully spherodization of cementite and dislocation rearrange into sub boundaries and fine carbides are pining these sub boundaries in pearlite ferrite as shown in Figure 6-4 (f).

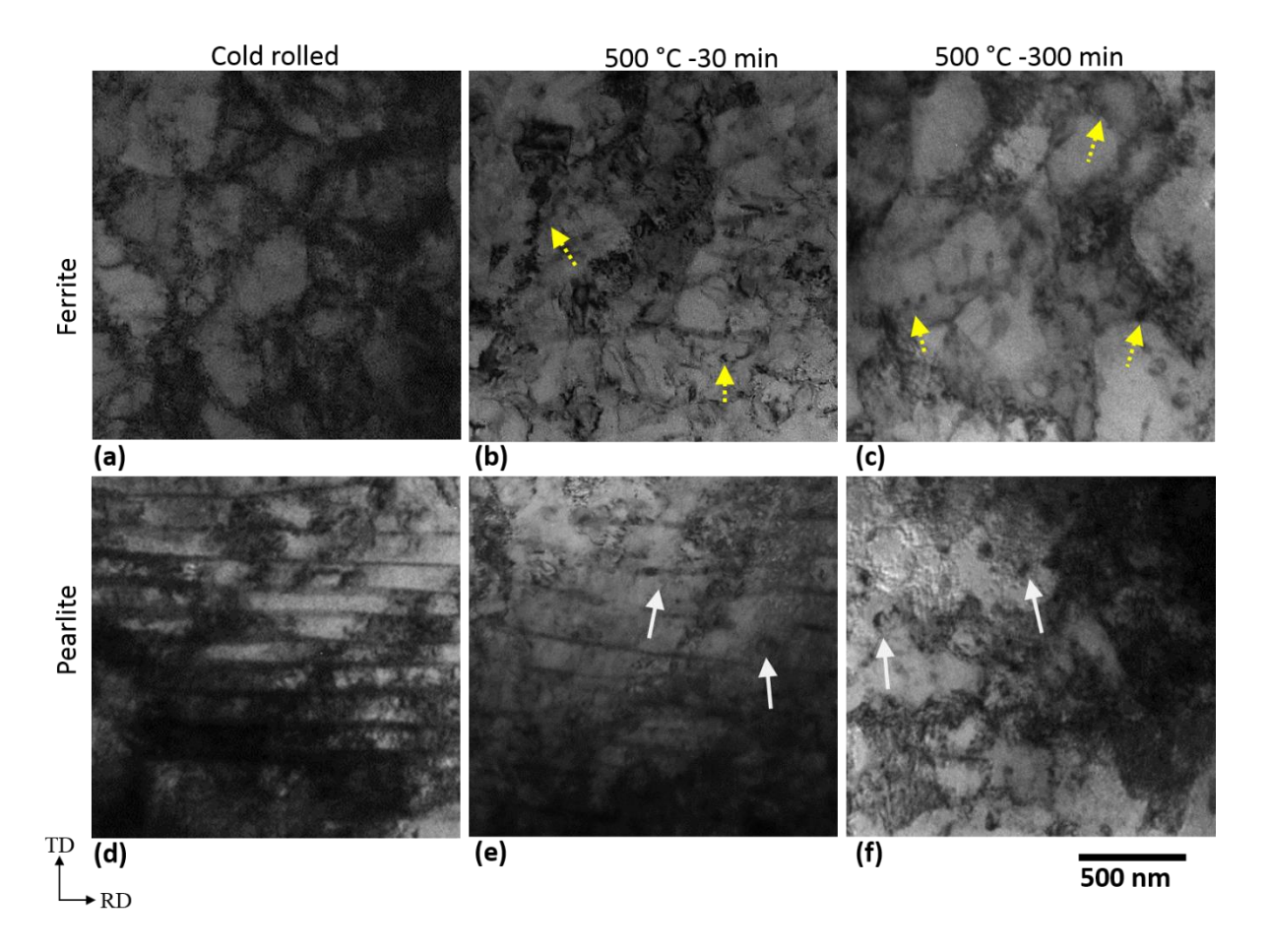


Figure 6-4 TEM micrographs of ferrite (a, b, c) and pearlite (d, e, f) in (a, d) cold rolling and subsequently recovery annealed at 500 °C for (b, e) 30 min and (c, f) 300 min of soaking time. Images in ferrite and pearlite were acquired along the z = [001] axis.

6.3.5 Micro Vickers hardness evolution

Upon increasing the annealing temperature to 500 °C for 30, 60, 120 and 300 min of soaking time, the hardness response as a function of soaking time is shown in Figure 6-5. Unlike the hardness response at 300 °C, the hardness decreases with soaking time. Figure 6-5 shows that hardness decrease is more pronounced in alloy 1 compared to other alloys, which show a similar trend. These results indicate that different mechanisms are acting in the single ferrite phase alloy 1 as compared to the dual phase alloys 2, 3 and 4. It is also interesting to observe that the hardness increase varied with soaking time and pearlite fraction at 300 °C. However,

at 500 °C the three pearlitic alloys follow a similar trend of hardness decrease with increasing soaking time.

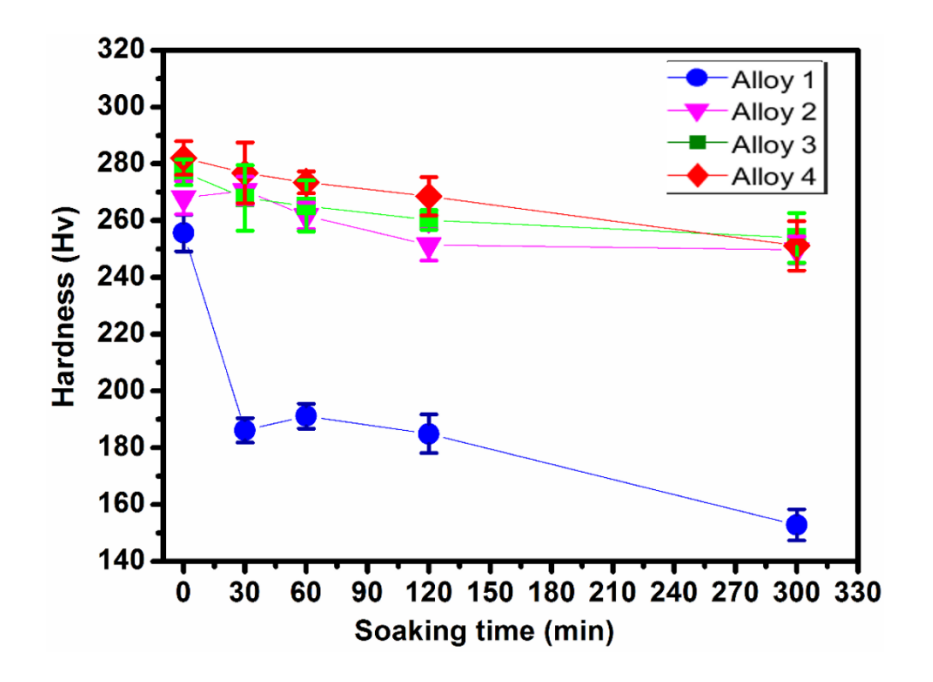


Figure 6-5 Micro Vickers hardness as a function of soaking time after recovery annealing at 500 °C for 30, 60, 120,300 min of soaking time in Alloy 2, Alloy 3 and Alloy 4 [8]. Hardness at 0 min refers to the cold-rolled state.

6.3.6 Nanoindentation mapping

To explore the local behavior of micro constituents (ferrite, pearlite) at the micrometer length scale, high speed-high resolution nanoindentation mapping is performed on all the materials after 30 min of annealing at 500 °C, as shown in Figure. 6-6. In a previous chapter, an excellent correlation between the microstructure and the corresponding hardness map was obtained in the cold-rolled condition of all the alloys.

In the cold-rolled condition for ferrite alloy 1, the hardness is mostly randomly distributed and ranges from 2 to 4 GPa. In contrast, in ferrite-pearlite alloys 2-4 the hardness in the cold rolled

condition shows more local variations corresponding to the two phases for both the non-banded and banded regions. The hardness in the pearlite colony of the non-banded region is less compared to the banded region. Also, the hardness of the pearlite in the banded region of alloy 4 is more than that of alloy 3. An increase in annealing temperature to 500 °C results in an overall drop in hardness to below that of the cold-rolled state in the case of alloy 1. In contrast, for alloys 2 and 3 the hardness of ferrite almost reverts to the cold-rolled state, whereas in the pearlite region the hardness decreases compared to the cold-rolled state. In alloy 4 the hardness decreases in both ferrite and pearlite phases compared to the initial state.

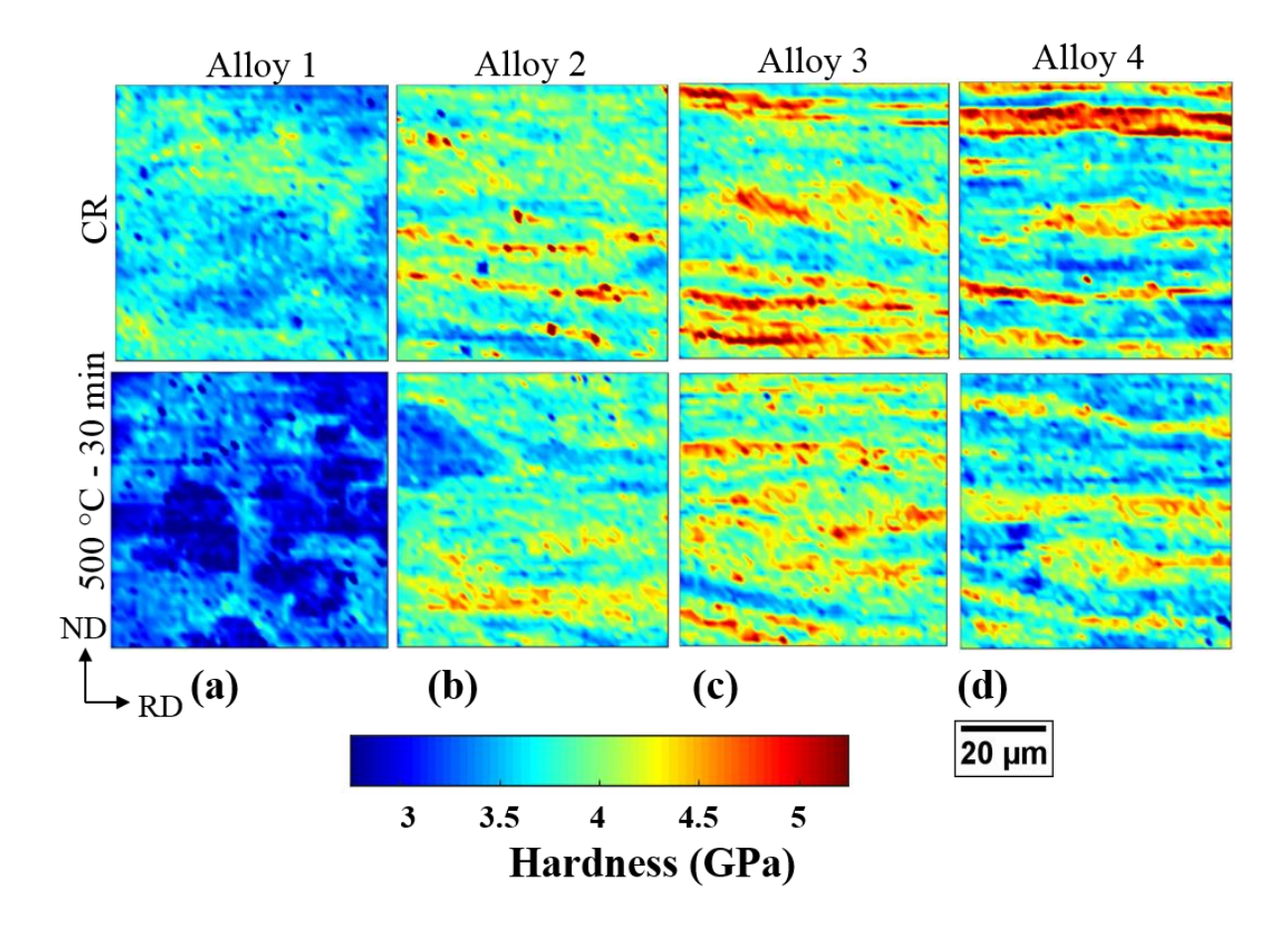


Figure 6-6 Nanoindentation hardness mapping of alloy 1, alloy 2, alloy 3/4 in cold rolled state and after recovery annealing at 300-500 °C for 30 min.

6.3.7 Hardness distribution of ferrite and pearlite

Quantitative hardness Probability Density Function (PDF)'s of both ferrite and pearlite phases are shown in Figure 6-7. The shift in the peak position from cold rolled to recovery annealed condition at 500 °C for 30 min is tracked. The average peak values and the corresponding standard deviation of each material at a given condition are reported in the legend of Figure 6-7 (top right).

In the cold rolled state, in the ferrite phase, the lowest hardness was observed in alloy 1; the hardness peak slightly shifts towards a higher value for alloys 2, 3 and 4. For the pearlite phase, the lowest hardness was observed in alloy 2, whereas the hardness peak shifts towards higher values in alloy 3 and alloy 4.

On annealing at 500°C, the ferrite phase of alloy 1 shows a significant hardness decrease with reference to the cold-rolled state, whereas in alloys 2 and 3 the ferrite hardness remains similar to the cold-rolled state. In alloy 4, the ferrite hardness slightly decreases as compared to the cold rolled state. In the pearlite phase, the hardness in alloy 2 remains similar to the cold-rolled state, whereas in alloys 3 and 4 the hardness decreases compared to the cold-rolled state. The pearlite hardness peak shift in alloy 4 is higher than in alloy 3. It is also interesting to observe that on annealing at 300 °C the standard deviation increases, reflecting the increase in peak width, particularly in the ferrite phase. This aspect will be revisited in the discussion section 6.4.2 in terms of the pearlite fraction and defect density.

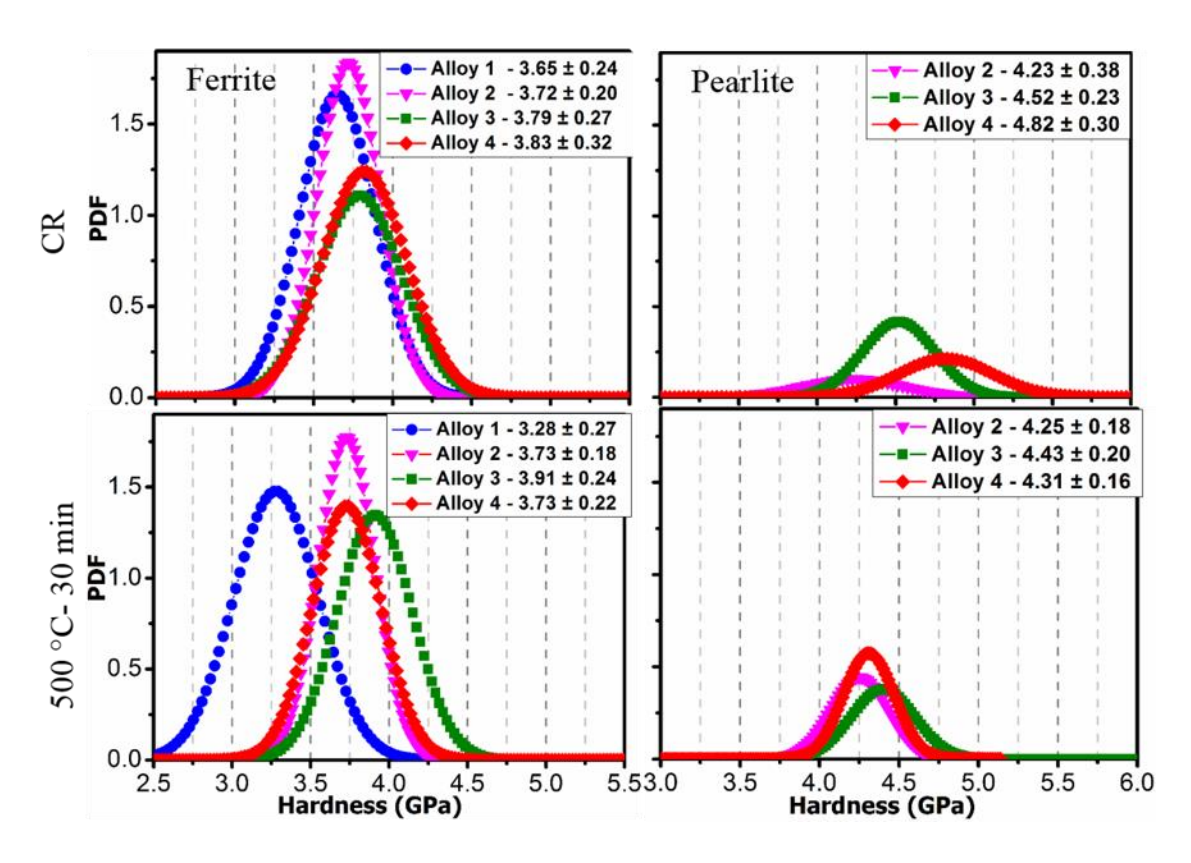


Figure 6-7 Hardness histograms of ferrite and pearlite in alloy 1, alloy 2, alloy 3/4 in cold rolled state and after recovery annealing at 500 °C for 30 min.

6.4 Discussion

In this section, insights from combining the results of microscopy, nanoindentation and simple models for kinetics will be provided to present a comprehensive picture of what drives the kinetics or the dominant mechanisms at 500 °C. Mainly, hardness decrease during annealing at 500 °C and the associated microstructural changes will be discussed. The occurring processes are evaluated by empirical kinetic laws to identify the mechanisms taking place at 500 °C. Further, insights on the role of individual phases (ferrite and pearlite) during hardness increases and decreases kinetics will be discussed.

6.4.1 Recovery kinetics

In this section, we present the hardness kinetics and the associated driving mechanisms will be discussed. As observed from micro Vickers hardness tests in Figure 7-5, ferrite-pearlite consisting steels shows the hardness changes at 500 °C, and are also dependent on soaking time. Results suggest different mechanisms are operating with temperature. Different kinetics models khulmann dislocation annihilation are quantitatively assessed and 500 °C as shown in Figure 6.8 Hardness changes deduced in this model are combined effect of both ferrite and pearlite.

On increasing the annealing temperature to 500 °C as shown in Figure 6-5, the hardness decrease is different in alloy 1 compared to alloys 2, 3 and 4. Surprisingly, in alloys 2, 3 and 4, the hardness decrease shows a similar trend with an increase in soaking time. These results indicate that different mechanisms are acting in the single ferrite phase alloy 1 and the ferrite/pearlite alloys 2-4. It is well known that the thermally activated processes result in a hardness decrease during recovery. KAM maps and TEM analysis, cf. Figures. 6.2 and 6.4, confirm that dislocation annihilation, cementite fragmentation induced spherodization in pearlite, subboundary formation, subboundary growth and carbide precipitation have been observed. All these structural changes during annealing at 500 °C have produced recovery (hardness decrease) as shown in SEM micrographs in Figure 6.1 and KAM maps in Figure 6.2. To assess the recovery process quantitatively a simple recovery model by Kuhlmann is being used.

According to Kuhlmann's empirical recovery relationship, recovery-related property change is inversely proportional to annealing time. [9].

$$\frac{d\sigma}{dt} = -\text{c.} \exp\left(\frac{Q_o - \sigma\Omega}{RT}\right)$$
 Equation (1)

Where c_o is a pre-exponential constant, Q_o is the activation energy, R is the gas constant and Ω is the activation volume. From integration of Eq. (1) at a constant temperature, it can be shown that the decrease in strength due to recovery ($\Delta \sigma = \sigma - \sigma_o$), can be written as

$$\Delta \sigma = -\frac{RT}{\Omega} ln(1 + \alpha t),$$
 Equation (2)

Where $\alpha = \frac{c_o RT}{\Omega} exp\left(-\frac{Q_o - \sigma_o \Omega}{RT}\right)$, may be treated as an integration constant in spite of having a weak dependence on initial strength and temperature. Assuming a constant constraint factor to relate hardness to flow stress, the change in hardness will have a similar functional dependence and can be written as

$$\Delta H = H_t - H_o = -\frac{RT}{\Omega} ln(1 + \alpha t),$$
 Equation (3)

From the equation, the fractional change in strength (hardness) is proportional to the logarithmic of $(1+\alpha t)$. The fractional change in hardness as a function of this parameter is shown in Figure 6-8.

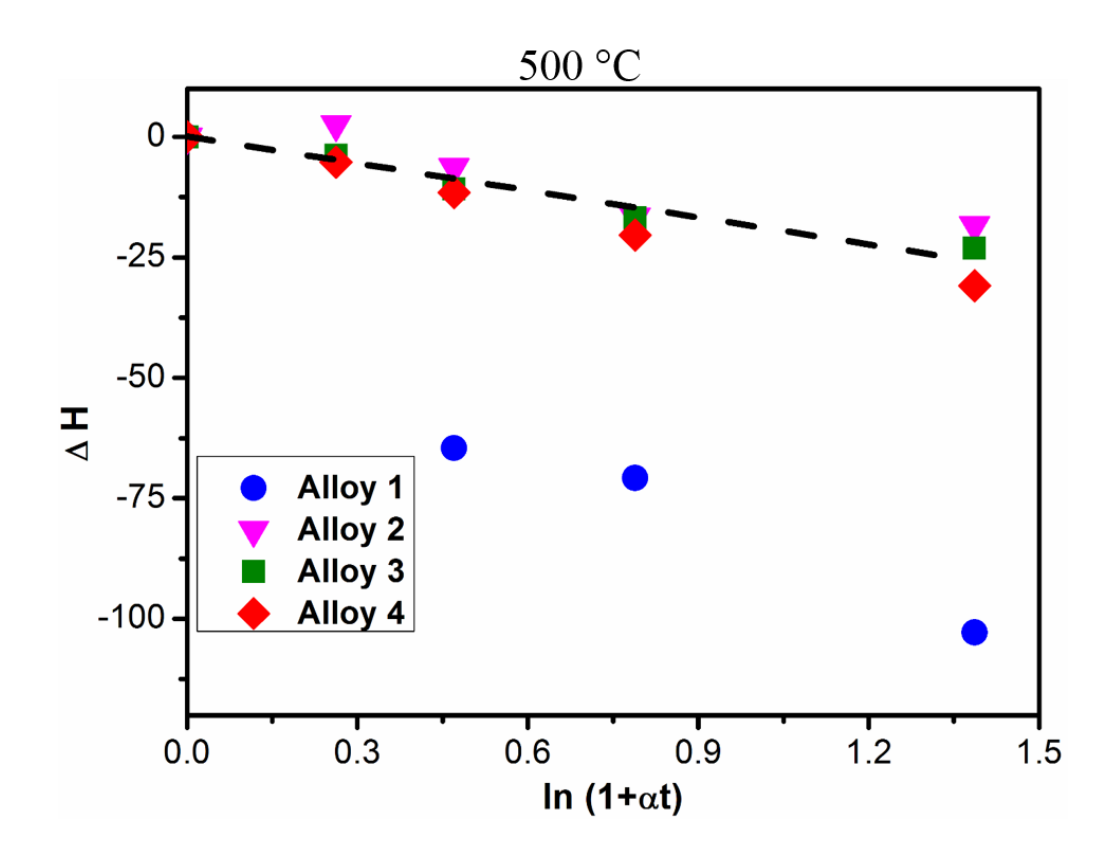


Figure 6-8. The fractional change in hardness ΔH as a function of log (1+ αt) at 500 °C

It can be seen that all the HSS consisting of a ferrite/pearlite microstructure (alloy 2, 3 and 4) nearly exhibit a similar response to the best fit (dotted line) as shown in Figure.6-8. It was found that the dotted line agrees well with a simple thermally activated model with a value $\alpha = 0.074$ (1/s). These results indicate that the single dominant thermally activated mechanism (process) that drives the recovery. Interestingly, alloy 1 chooses a different response which is confirmed to be the onset of recrystallization as shown on the KAM map in Figure. 6-2. The structural changes observed in alloy 1, are completely absent in the ferrite-pearlite alloys 2, 3 and 4 suggesting the absence of recrystallization. Despite having different prior processing histories the hardness decrease is similar, the reason for this will be discussed and further insights will be provided in the next section.

In the above paragraphs hardness, increase/decrease was assessed by analyzing kinetic evolutions with varying soaking times. However, the role of pearlite on hardness increase/decrease in individual phases of alloy 2, alloy 3/4 could not be explained. At 500 °C the hardness decrease in alloys 2, 3 and 4 is rather sluggish indicative of retarded recovery, whereas alloy 1 recrystallizes. To get more detailed insights into the behavior of individual phases properties must be assessed and correlated with structural changes.

6.4.2 Role of pearlite on recovery kinetics at 500 °C.

As we have observed hardness decrease by thermally activated process and follow khulmann recovery kinetics, what is drives those kinetics is not known? To assess that we use deconvoluted data obtained from nanoindentation as reported in Figure. 6-7, to further show the insights in the individual phases. The hardness of ferrite and pearlite was plotted as a function of the pearlite fraction as shown in Figure.6-9. On annealing at 500 °C at 30 min in ferrite as shown in Figure 6-9(a), hardness in alloy 1 significantly decreases below the cold rolled state. Whereas in pearlite consisting of alloy 2, alloy 3/4, hardness reaches back to the cold-rolled state as shown by the best fit line with varying pearlite fraction. The data point of alloy 1 was disregarded to get the best fit in the case of ferrite at 500 °C. These results suggest the recovery is being retarded in ferrite due to the presence of pearlite. KAM distribution in Figure. 6-3, further confirms retardation of recovery as the distribution remains similar to the cold-rolled even after annealing. TEM analysis in Figure 6-4(b), shows the annihilation of dislocations inside the sub boundaries and the presence of dislocation at sub boundaries it was also observed that carbon was clustered and few fine carbides were present inside/on sub boundaries.

At 500 °C, due to an increase in annealing temperature higher amount of carbon might have entered the ferrite matrix. Shin et al [10] reported that carbon might redistribute and precipitate as carbides on sub boundaries/dislocations and grain boundaries causing the retardation of recovery these results agree well with the present TEM observation in Figure 6-4(b). These might be causing retardation of recovery and migration of grain boundary the present results are in good agreement with TEM analysis reported by Song et al [11].

whereas in the case of pearlite as shown in Figure 6-9 (b), increasing pearlite content results in a decrease in hardness below the cold rolled state for alloy 3/4 sheets of steel. This result indicates that recovery is initiated in the pearlite. TEM analysis in Figure 6-4(e), confirms that cementite fragmentation induced spherodization and dislocation annihilation in the pearlitic ferrite to lead to the overall recovery of pearlite in alloy 4, hardness decreases are higher in pearlite compared to alloy 3 and alloy 2, the reason for the same might be due to an increase in the rate of spherodization, due to the presence of the highest amount of cementite and defects. The reasons for increases in the rate of spherodization are also well discussed and reported in [11]. It is reasoned that self-diffusion of iron increases with increasing carbon content, it is thus expected that steels with higher carbon (in present case alloy 4) have a higher recovery rate [12,13]. This could be the reason for also that the hardness decrease is higher in both ferrite and pearlite of alloy 4 in comparison to alloy 3 and alloy 2. However, KAM distribution remains similar to annealing at 300 °C as in shown Figure. 6-3. These results suggest that suggests that the recovery in pearlitic ferrite is still retarded, this might be due to the presence of carbon in solution and rearrangements or carbon/carbides on dislocation.

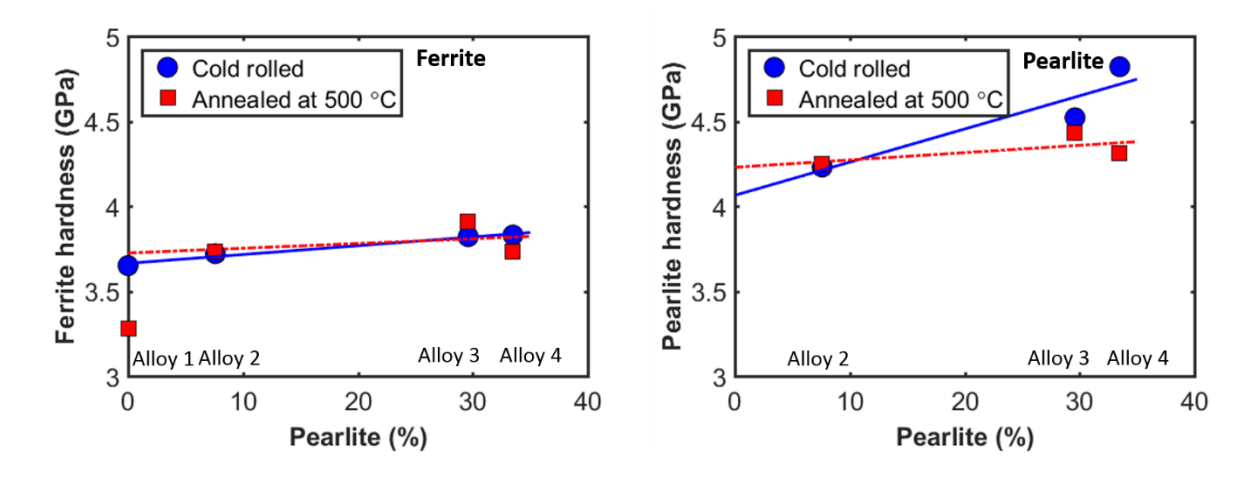


Figure 6-9 . Hardness of (a) bulk ferrite and (b) pearlite as a function of pearlite fraction after cold rolling and recovery annealing at 500 °C for 30 min

6.5 Summary and conclusions

The present chapter focuses on static recovery kinetics of 80% cold-rolled steel sheets consisting of ferrite-pearlite in three different HSS in comparison to alloy 1 consisting of only ferrite. Mainly pearlite fraction and its distribution were varied to investigate the role of pearlite annealing temperatures 500 °C for various soaking times. In the single ferrite phase, alloy 1 recovery and recrystallization dominated at 500 °C. Whereas in the presence of pearlite in alloy 2, alloy 3/4 shows recovery is slower and sluggish kinetics at 500 °C. Using complementary techniques such as nanoindentation and electron microscopy with EBSD and TEM gave a better understanding and insights into the driving force for such temperature-dependent recovery kinetics. The reasons for the same are well summarized and the following conclusions can be drawn:

 In the single ferrite phase, alloy 1 recovery, and recrystallization dominated as confirmed from KAM maps and distribution, causing a significant decrease in hardness.

- 2. Whereas the presence of pearlite in alloy 2, alloy 3, and alloy 4 shows hardness decreases with time, hardness decreases follow a similar trend in all ferrite-pearlite consisting steels, showing is slower and sluggish kinetics at 500 °C.
- 3. Nanoindentation and hardness distribution in alloy 2-4, confirm hardness decreases in pearlite, whereas in ferrite it remains similar to the cold rolled state.
- 4. KAM distribution in alloy 2-4, misorientation decrease with time indicating a recovery in ferrite. In pearlite misorientation decreases after 60 min of soaking time.
- 5. TEM, analysis in alloy 3 shows, dislocation annihilation and pinning of the sub boundaries by fine carbides in ferrite. In pearlite, dislocation annihilation and fragmentation-induced spherodization take place.
- 6. Recovery dominates by the thermally activated process leading to structural changes such as spherodization cementite, dislocation annihilation and subgrain growth.
- 7. In alloys 2-4, Recovery kinetics suggest that fractional change in property is inversely proportional to temperature and the logarithmic time and follows Khulmanns models.
- 8. All the ferrite-pearlite consisting recovery follows a similar trend in decreasing hardness. Recovery is initiated in pearlite mainly by fragmentation-induced spherodization. Whereas recovery in ferrite is being retarded mainly due to pinning the dislocation and sub boundaries by carbides causing retardation.

References

- [1] A. Martínez-de-Guerenu, F. Arizti, M. Díaz-Fuentes, I. Gutiérrez, Recovery during annealing in a cold rolled low carbon steel. Part I: Kinetics and microstructural characterization, Acta Mater. 52 (2004) 3657–3664. https://doi.org/10.1016/j.actamat.2004.04.019.
- [2] S. Dutta, A.K. Panda, A. Mitra, S. Chatterjee, R.K. Roy, Microstructural evolution, recovery and recrystallization kinetics of isothermally annealed ultra low carbon steel Microstructural evolution, recovery and recrystallization kinetics of isothermally annealed ultra low carbon steel, (2020).

- [3] Y.Z. Chen, G. Csiszár, J. Cizek, X.H. Shi, C. Borchers, Y.J. Li, F. Liu, R. Kirchheim, Defect Recovery in Severely Deformed Ferrite Lamellae During Annealing and Its Impact on the Softening of Cold-Drawn Pearlitic Steel Wires, Metall. Mater. Trans. A Phys. Metall. Mater. Sci. 47 (2016) 726–738. https://doi.org/10.1007/s11661-015-3263-z.
- [4] J. Takahashi, M. Kosaka, K. Kawakami, T. Tarui, Change in carbon state by low-temperature aging in heavily drawn pearlitic steel wires, Acta Mater. 60 (2012) 387–395. https://doi.org/10.1016/j.actamat.2011.09.014.
- [5] Y.J. Li, P. Choi, S. Goto, C. Borchers, D. Raabe, R. Kirchheim, Evolution of strength and microstructure during annealing of heavily cold-drawn 6.3 GPa hypereutectoid pearlitic steel wire, Acta Mater. 60 (2012) 4005–4016. https://doi.org/10.1016/j.actamat.2012.03.006.
- [6] A. Smith, H. Luo, D.N. Hanlon, J. Sietsma, S. Van Der Zwaag, Recovery processes in the ferrite phase in C-Mn steel, ISIJ Int. 44 (2004) 1188–1194. https://doi.org/10.2355/isijinternational.44.1188.
- [7] J. Gautam, A. Miroux, J. Moerman, L. Kestens, TNR dependent hot rolling microstructure and texture development in c-Mn dual phase and HSLA steels, Defect Diffus. Forum. 391 (2019) 120–127. https://doi.org/10.4028/www.scientific.net/DDF.391.120.
- [8] S. Janakiram, J. Gautam, P.S. Phani, L.A.I. Kestens, Microstructural and micro hardness variation during low temperature recovery annealing in C-Mn high strength Steels, J. Phys. Conf. Ser. 1270 (2019). https://doi.org/10.1088/1742-6596/1270/1/012017.
- [9] E. Nes, Recovery revisited, Acta Metall. Mater. 43 (1995) 2189–2207. https://doi.org/10.1016/0956-7151(94)00409-9.
- [10] D.H. Shin, Y.S. Kim, E.J. Lavernia, Formation of fine cementite precipitates by static annealing of equal-channel angular pressed low-carbon steels, Acta Mater. 49 (2001) 2387–2393. https://doi.org/10.1016/S1359-6454(01)00165-3.
- [11] R. Song, D. Ponge, D. Raabe, R. Kaspar, Microstructure and crystallographic texture of an ultrafine grained C-Mn steel and their evolution during warm deformation and annealing, Acta Mater. 53 (2005) 845–858. https://doi.org/10.1016/j.actamat.2004.10.051.
- [12] H. Beladi, P.D. Hodgson, Effect of carbon content on the recrystallization kinetics of Nbsteels, Scr. Mater. 56 (2007) 1059–1062. https://doi.org/10.1016/j.scriptamat.2007.02.029.
- [13] H.W. Mead, C.E. Birchenall, Self-Diffusion of Iron In Austenite, Jom. 8 (1956) 1336–1339. https://doi.org/10.1007/bf03377878.

Chapter 7

Partial recrystallization annealing at 700 $^{\circ}\text{C}$

7

Partial recrystallization annealing was performed on the three different cold rolled AHSS with varying pearlite content, at 700 °C for a different soaking time followed by water quenching to arrest the recrystallization. Annealing at 700 °C resulted in boundary mobility causing recrystallization of ferrite. In this chapter, the ability to capture the local difference in hardness has been demonstrated on recrystallized and recovered ferrite. A more comprehensive work involving mapping different alloys at the same recrystallization fraction has to be carried out to get a much better understanding of the three alloys. To establish structure-property correlation, microscopy and nanoindentation were performed in a similar region on partial recrystallization in three different AHSS.

7.1 Introduction

Due to the balance of high strength and good formability, the automobile industry is paying close attention to AHSS' lightweight vehicle design, which reduces weight and improves fuel economy. [1–4]. The microstructure of these steels consists of a dual phase soft ductile ferrite matrix embedded with hard martensite islands [1,2,4]. Dual-phase microstructures are generated by reheating the initial ferrite-pearlite cold rolled microstructure in the intercritical annealing temperature, to form austenite/ferrite matrix which is later quenched to attain DP microstructure. To date, extensive studies have been carried out mainly in the intercritical annealing region of initial ferrite-pearlite cold rolled steels [1,4,5]. whereby complex

metallurgical phenomena may occur concurrently such as recovery, recrystallization, grain growth of ferrite grains, carbon diffusion, austenite nucleation and growth, etc [1,4]. However, the recrystallization of the initial ferrite-pearlite cold rolled structure has comparatively received less attention. The above-mentioned metallurgical phenomena are inherently interlinked with each processing stage during thermomechanical processing. It is quite challenging to isolate the role of each phenomenon during the intercritical annealing due to interacting processes, which may influence the microstructure and properties ensuing from the entire process. In chapter 5, it was observed that during recovery at low-temperature concurrent recovery by rearrangement to defects leading sharpening of cell boundaries, carbon defect interaction causing to increase in hardness. Whereas in chapter 6, recovery by cementite spherodization and pinning of sub boundaries by carbides causes sluggish recovery causing to decrease in hardness has been observed. However, in addition to the above processes, recrystallization results in grain boundary mobility.

Hutchinson et al.[6] Has reported that during recrystallization, simultaneously carbon dissolution from cementite and recrystallization of ferrite takes place. Peranio et al. [4] have reported that annealing below intercritical annealing temperature results in competition between recovery and recrystallization. Ghiabakloo et al. [7] have reported a hardness increase before the onset of recrystallization in ferrite pearlite low carbon steel after severe plastic deformation. Hardness increase was mainly due to carbon dissolution from cementite precipitates in ferrite. All the above literature suggests during recrystallization concurrently or simultaneously complex local interactions between diffusion of carbon, recovery and recrystallization of ferrite phenomena take place. Despite these significant findings and their

potential practical application, further investigation of such local interaction phenomena, and their impact on the final microstructure and properties annealed on recrystallization is required.

7.2 Experimental details

In this study, only alloy 2, alloy 3, and alloy 4 were used and the chemical composition is listed in Table 3.1. All the three steel sheets were initially hot rolled above the austenite recrystallization temperature followed by coiling at the pearlite start temperature to obtain a ferrite- pearlite microstructure [8]. These sheets were further cold rolled to 80% reduction.

To investigate and establish the structure-property correlation on boundary mobility, interrupted annealing was carried out at 700 °C, for 10, 20, 30, 60, 90, 120, 150, 180, 300 and 420 seconds of soaking time. Micro Vickers hardness tests were performed on the cold rolled and annealed samples at 700 °C as reported in chapter 3 section 3.6.1. The results obtained after micro Vickers hardness tests after cold rolled and annealing at 700 °C for the various soaking time in all the three alloys is shown in Figure 7-1(a-b). The corresponding changes in the microstructure on annealing are shown in Figure 7-2(a-c). Hardness changes as a function of soaking time are shown in Figure 7-1(a), and the percentage change in hardness was plotted as a function of soaking time as shown in Figure 7-1(b). On annealing at 700 °C, hardness changes showed characteristic differences, surprisingly it increases for the first 10 s and then decreases. The dotted line in Figure 7-1(b), is marked to show the time taken in each alloy to reach back to the cold rolled state. The hardness increases for the first 10 s of soaking time on annealing as in Figure 7-1(a-b). The corresponding microstructure in Figure 7-2 doesn't show any change in both ferrite and pearlite in alloys 2, 3, 4 and retains its cold rolled structure. In alloy 4, on increasing the soaking time to 20-30 s of, significant hardness drops take place in alloy 4, mainly due to boundary mobility i.e, recrystallization of ferrite as shown in Figure 7-

2 (c). Whereas the hardness decrease was slower and sluggish in alloys 2, and 3 compared to alloy 4. In Figure 7-2(b), it can be observed that above the dotted line hardness decrease slower and sluggish whereas below line hardness decrease is much faster. The corresponding microstructure above and below the dotted line is shown in Figure 7-2 Above the dotted line in Figure 7-1(b) in alloys 2 and 3 it takes about 180-120 s, the corresponding microstructure in Figure 7-2 (a-b) shows the presence of fine recrystallized ferrite grains due to boundary mobility, recovered ferrite and pearlite. Below the dotted line in Figure 7-2(b), the corresponding microstructure suggests that in alloy 2-3 an additional above-mentioned process, recrystallization of ferrite i.e, boundary mobility is dominating. To further investigate the microstructure-property correlation during the boundary mobility response, and provide insights, nanoindentation and electron microscopy were performed in a similar region on selected samples. Three samples were chosen such that the boundary mobility response and simultaneously recovery and cementite spherodization in pearlite can be captured. Three samples from each material were chosen below the dotted line, namely alloy 4 soaked for 30 seconds, alloy 3 takes 180 and alloy 2 takes 300 seconds.

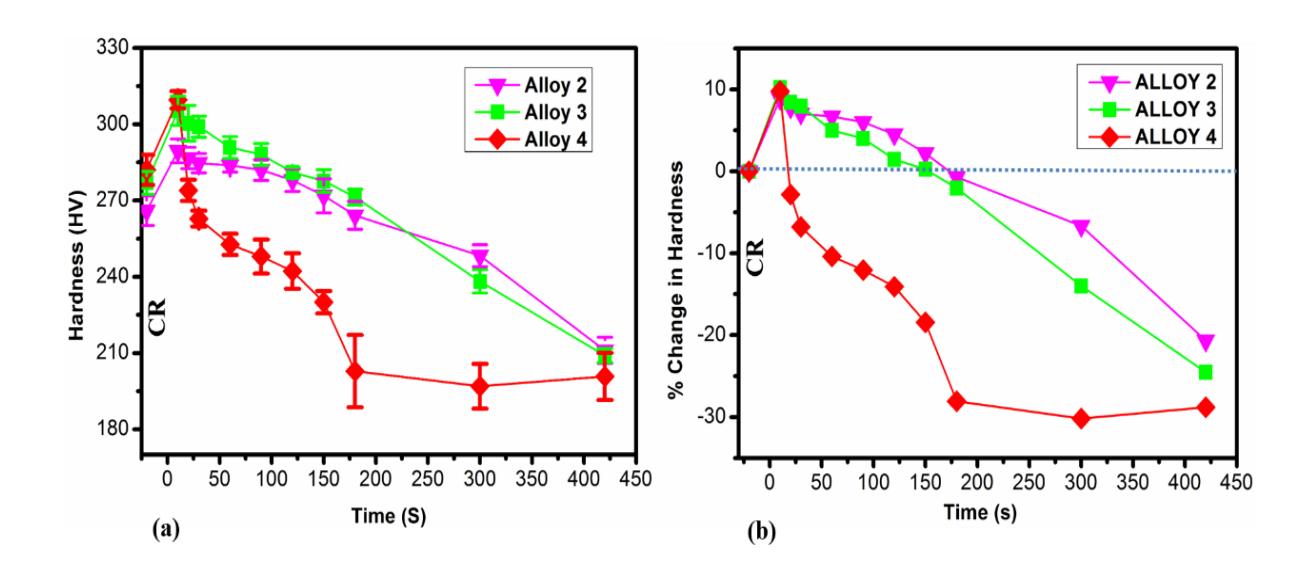


Figure 7-1 shows hardness changes as a function of soaking time (a) and percentage changes in hardness as a function of soaking time (b) in alloy 2, alloy 3, and alloy 4 on annealing at 700 °C.

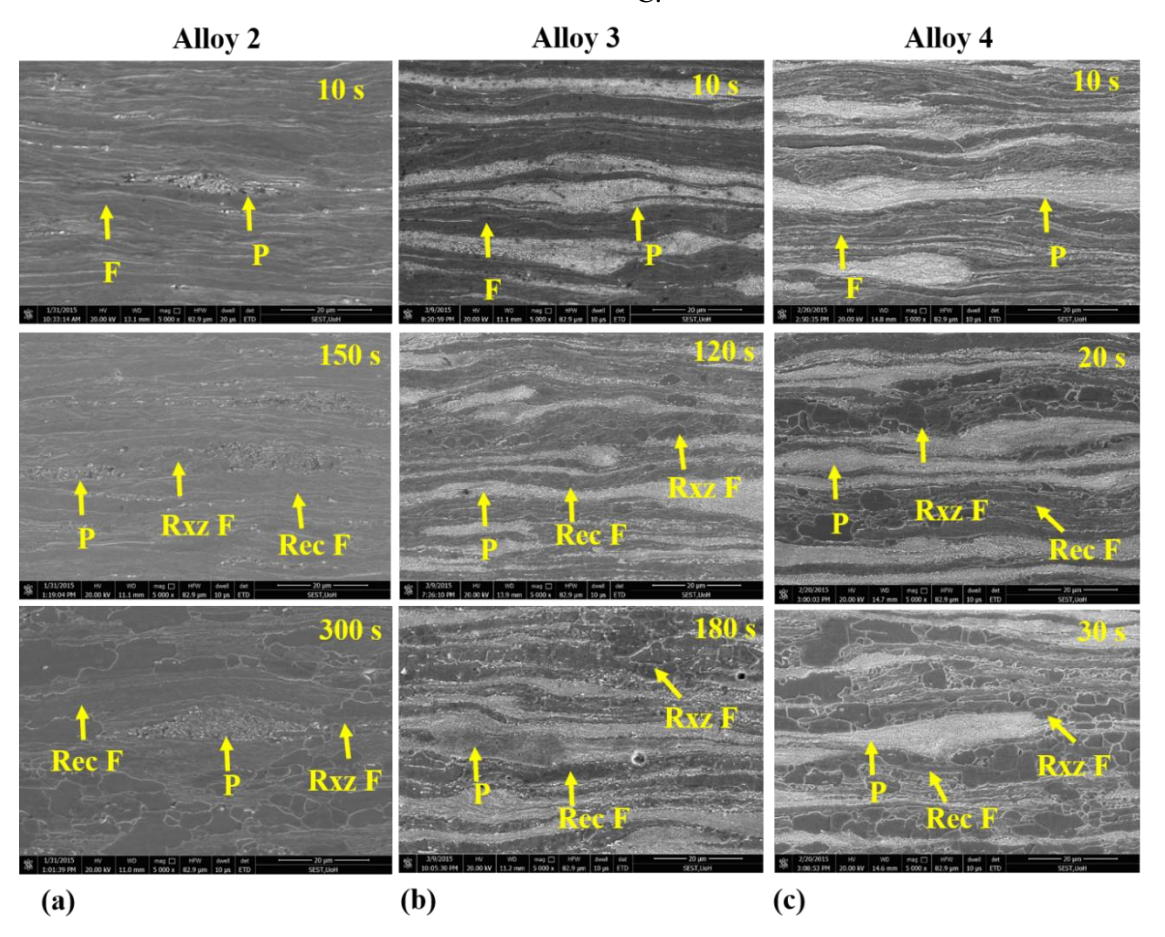


Figure 7-2 Microstructural changes on partial recrystallization annealing at 700 °C for the various soaking time in (a) alloy 2 (b) alloy 3 (c) alloy 4

7.3 Results

7.3.1 Microstructural evolution by SEM

Scanning electron micrographs of alloys 2, 3 and 4 showing changes in ferrite and pearlite in Figure 7-3 (a-c), and high-resolution inserts of only pearlite in 7-3 (d-f). Figure 7-3(a-c), shows the presence of recrystallized ferrite, recovered ferrite still having deformed arrangements and pearlite. High-resolution inserts in Figure 7-3 (d-f) show that in the three alloys cementite is spherodized. The pearlite appears to be fully spherodized in alloys 2 and 3 in comparison to alloy 4.

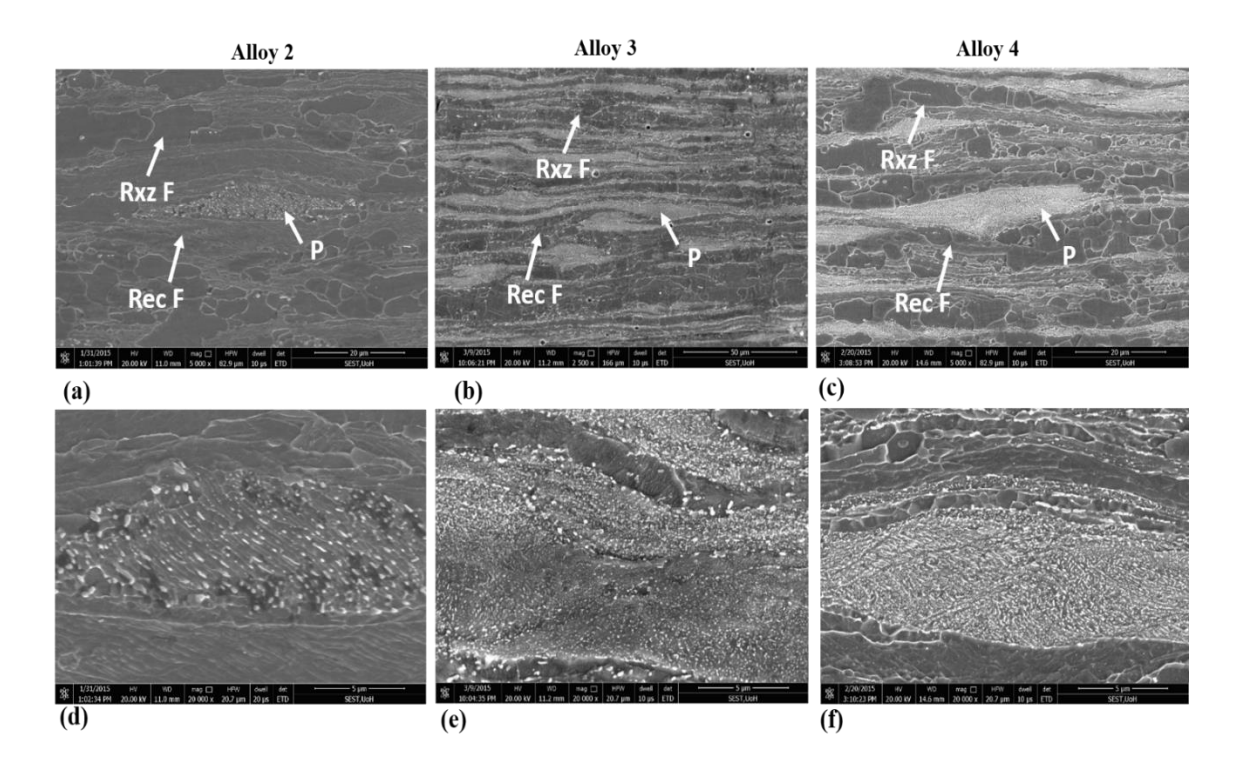


Figure 7-3 SEM showing changes in ferrite and pearlite in (a, b, c) and only pearlite in (d, e, f) of alloy 2, alloy 3 and alloy 4

7.3.2 KAM evolution after annealing at 700°C

To partition recrystallized, recovered ferrite and pearlite from EBSD data, IQ and KAM maps were obtained in all three alloys as shown in Figure 7-4 (a-b). IQ map shows the presence of new recrystallized ferrite grain surrounded by high angle boundary, recovered ferrite retains the deformed arrangements of grain and pearlite has the lowest IQ as in Figure 7-4 (a). The corresponding KAM maps in Figure 7-4(b) show recrystallized ferrite in blue color having less than 1-degree misorientation [10]. It was observed that recrystallized ferrite fraction varied in all the three alloys, where alloy 2 consisted of 18%, alloy 3 consists of 13% and alloy 4 only consisted of almost 12%. In alloy 2, alloy 3 and alloy 4, where boundary mobility takes place but the grain still appears in green color with misorientation in the range of 1-2 degrees. These results suggest recrystallization is being retarded or still in progress and these grains are still in the recovered state and not fully recrystallized even after boundary mobility takes place the reasons for the same will be discussed in the discussion section 7.4.

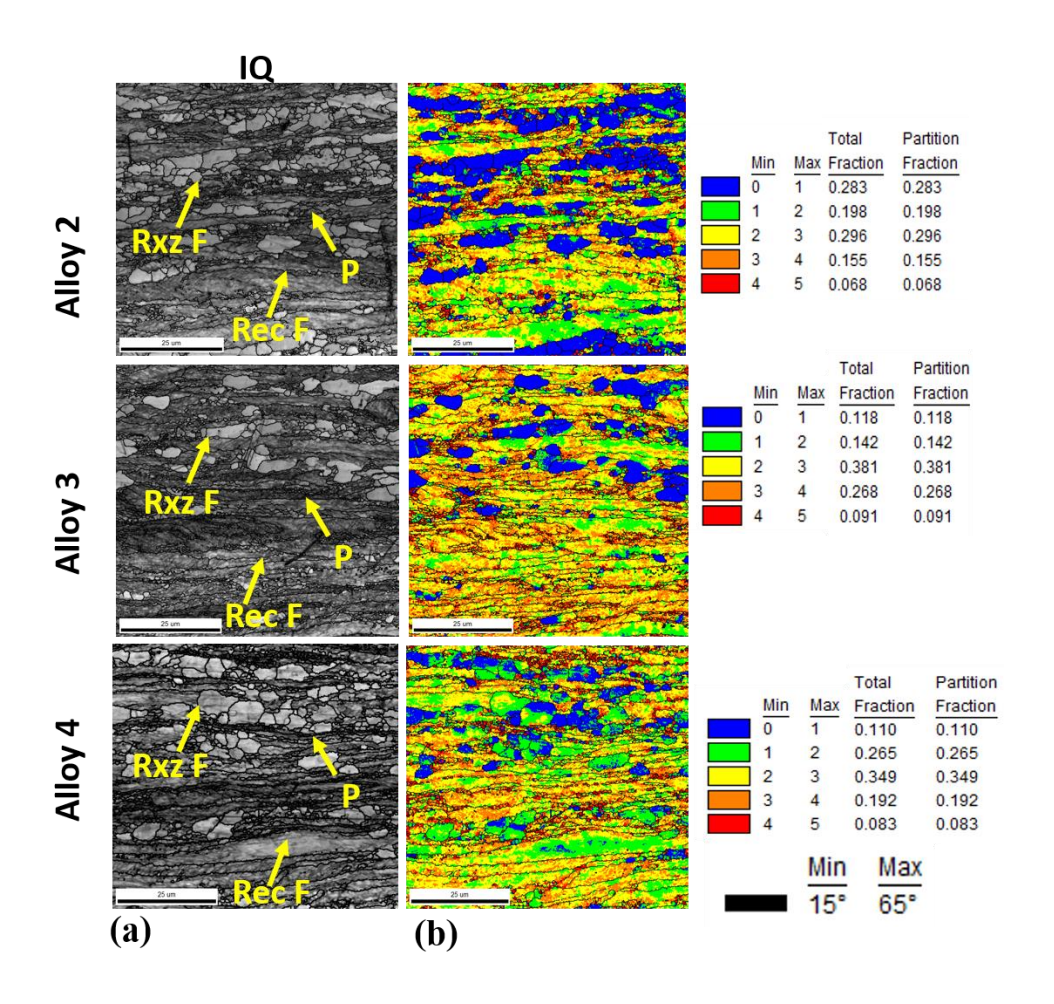


Figure 7-4 shows microstructural changes after annealing at 700° (a) IQ and (b) KAM maps in alloy 2, alloy 3, alloy 4

Rxz-F recrystallized ferrite, Rec-F recovered ferrite, P-pearlite

7.3.3 Nanoindentation mapping

The IQ and hardness maps obtained from EBSD, and nanoindentation hardness mapping in all the three alloys are shown in Figure 7-5 (a-c). The IQ maps as in Figure 7-5(a) show the presence of recrystallized, recovered ferrite and pearlite. The corresponding hardness map is shown in Figure 7-5 (b), hardness map was overlaid by a grain boundary map obtained from EBSD to trace the boundary migration and associated local changes in hardness as shown in Figure 7-5 (c). The hardness maps in Figure 7-5(b) capture the difference in recrystallized, recovered ferrite and pearlite regions at this length scale, with hardness ranging from 3 to 5.5

GPa. A qualitative good agreement has been observed in IQ and hardness map with grain boundary overlay as in Figure 7-5(a-c). The higher IQ with light grey color in Figure 7-5(a) represents recrystallized ferrite and the corresponding hardness map captures well as shown in Figure 7-5(b) in deep blue color. The recovered ferrite in the IQ map shows a deformed arrangement of grain and the corresponding hardness maps captures well and are shown in cyan color. The dark color with lower IQ represents pearlite, shown in yellow/red color in the corresponding hardness map. The difference between the recrystallized, recovered ferrite and pearlite was well captured by nanoindentation mapping. The local hardness difference in recrystallized, recovered ferrite and pearlite across all the three alloys was also observed qualitatively from hardness maps as in Figure 7-5(a-c).

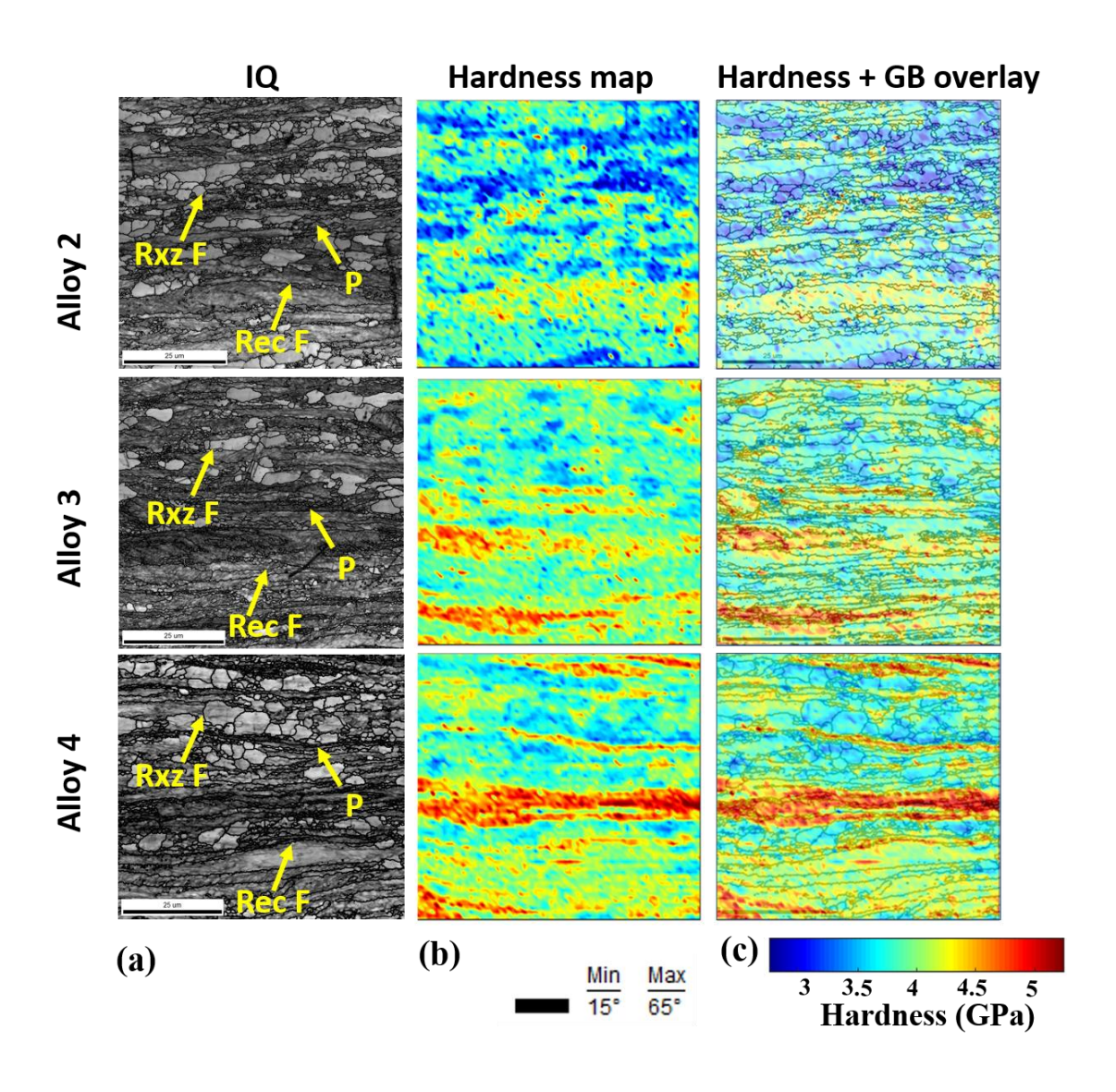


Figure 7-5 shows microstructure and corresponding hardness changes in (a) IQ map, (b) hardness map (c) hardness map overlaid by grain boundary map after annealing 700°C in alloy 1, alloy 2, and alloy 3.

Rxz-F recrystallized ferrite, Rec-F recovered ferrite, P-pearlite

7.3.4 Deconvolution from hardness map

Figure 7-6(a-b) shows IQ maps obtained from EBSD and corresponding deconvoluted maps obtained from hardness maps and overlaid by grain boundary map. IQ maps show the presence of recrystallized, recovered ferrite and pearlite in all three alloys as in Figure 7-6(a). Corresponding deconvoluted maps in Figure 7-6(b), show recrystallized ferrite in blue color,

recovered ferrite in green color and pearlite in red color. It was observed that a good spatial correlation exists between individual phase constituents in IQ and deconvoluted maps.

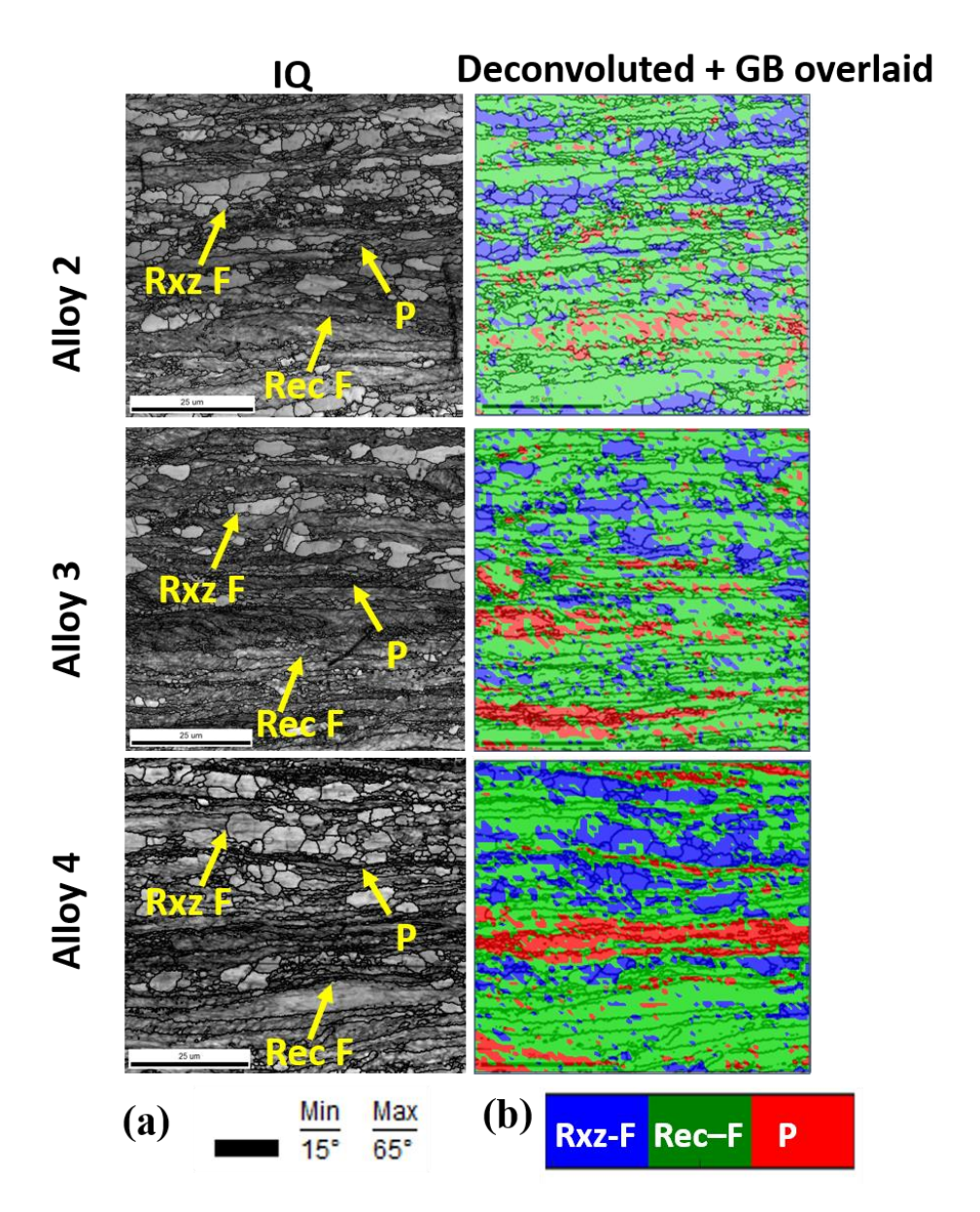


Figure 7-6 shows recrystallized, recovered ferrite and pearlite after annealing at 700 °C in (a) IQ map (a) and (b) deconvoluted maps overlaid by grain boundary map, in alloy 2, alloy 3, and alloy 4

7.3.5 Hardness distribution

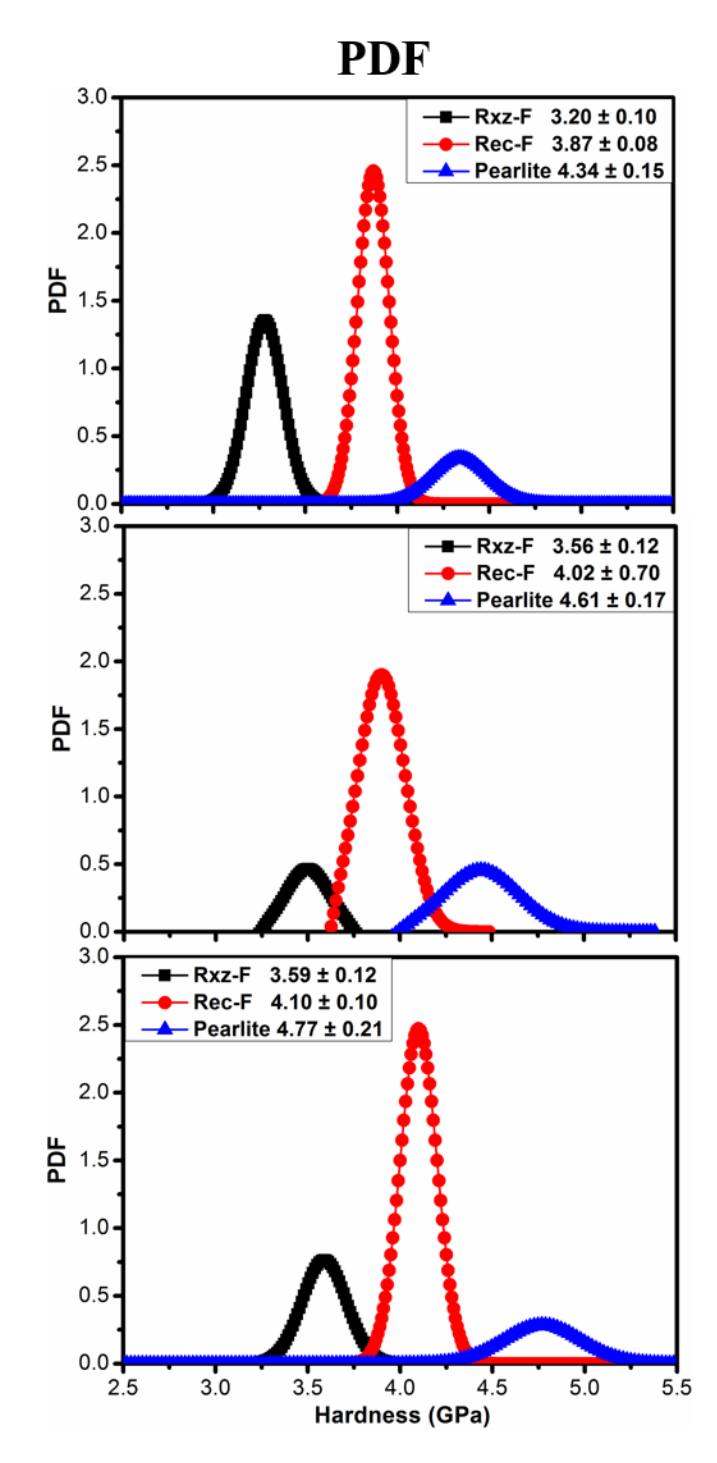


Figure 7-7 hardness histograms of alloys 2, alloy 3 and alloy 4 Rxz-F recrystallized ferrite, Rec-F recovered ferrite, P-pearlite

Quantitative hardness Probability Density Function (PDF)'s of recrystallized, recovered ferrite and pearlite phase are shown in Figure 7.7. The shift in the peak position in alloys 2, 3 and 4

after partial recrystallization annealing at 700 °C is tracked. The average peak values and the corresponding standard deviation of each material at a given condition are reported in the legend of Figure 7-7. In all the alloys 2-4, it was observed that recrystallized ferrite had the lowest hardness, recovered ferrite had slightly higher hardness and pearlite had maximum hardness. It was also interesting to observe that the hardness of recrystallized, recovered ferrite and pearlite, also varied in alloys 2, 3 and 4, the reasons for the same will be discussed later in section 7.4.1.

7.4 Discussion

In this section, combining the results of microscopy, nanoindentation will be provided to present a comprehensive understanding of partial recrystallization in all three alloys.

SEM micrographs in Figure 7-3, show on annealing at 700 °C resulted in grain boundary mobility in all three alloys leading to recrystallization of ferrite. Along with it, recovered ferrite and pearlite is present. In pearlite, cementite is spherodized in all three alloys. EBSD employing IQ, KAM maps as in Figure 7-4, and hardness, as well as deconvolute maps obtained from nanoindentation mapping as in Figure 7-5 and 7-6 revealed a strong spatial correlation exists between recrystallized, recovered ferrite and pearlite. The hardness of individual micro constituents presents these were quantitatively obtained by deconvolution nanoindentation mapping data and is reported in Figure 7-7. Recrystallized ferrite, which is free of defect/substructure has less than 1-degree misorientation as shown in KAM maps, and the lowest hardness was reported in these regions shown in hardness maps in Figure 7-5 and quantitatively reported in Figure 7-7. Slightly higher hardness was reported in recovered ferrite where the cold rolled grain structure is retained and has higher than 1-degree misorientation as observed from KAM maps. Maximum hardness was reported in the pearlite

region and the KAM maps show maximum misorientation. However, it was observed that local difference in hardness was observed across three alloys in recrystallized, recovered ferrite and pearlite. The probable reason for the same might be due to the difference in soaking time leading to different recrystallization fractions in three alloys. Higher hardness in pearlite and recovered ferrite was observed in alloys 3, alloy 4 compared to alloy 2. In the case of alloy 4 and alloy 3 due to the presence of a higher amount of pearlite, a higher amount of carbon might dissolve and precipitate in ferrite and pin dislocations or subgrain/grain boundaries and retard the process of recrystallization, [11,12]. This might be the reason the grains are still in the recovered stage and causing slightly higher misorientation and hardness in alloy 3, alloy 4 compared to alloy 2 as observed in Figure 7-4 and 7-5. Whereas in alloy 2, due to higher soaking time and low pearlite fraction, less amount of carbon might dissolve in ferrite and with increasing time precipitates might coarsen and allow higher migration of HAGB.

To further investigate the role of pearlite and provide an understanding of the role or individual phases, hardness changes obtained from nanoindentation in both ferrite and pearlite from cold rolled, to recovery and partially recrystallized annealed at 300-500-700 °C. Only alloy 2 and alloy 3 were chosen for representative purposes as shown in Figure 7-8.

7.4.1 Role of pearlite

The hardness of individual phases obtained from deconvolute phases maps were plotted as a function of temperature to see how cold rolling is influencing, recovery and recovery further influencing recrystallization in alloy 2 and alloy 3 as shown in Figure 7-8. The associated microstructural changes during the above-mentioned processing are shown in the form of a schematic in Figure. 7-9 based on the TEM observation in chapters 5 and 6 in this thesis. In the case of ferrite, in cold rolled condition alloy 2 and 3 show similar hardness. Whereas in

pearlite, it was observed that alloy 3 had higher hardness compared to alloy 2 mainly due to an increase in pearlite area fraction. Figure 7-9 (a) shows that dislocations are accumulated in ferrite and pearlite regions, also there strong solute (carbon) gradient from pearlitic ferrite, adjacent to cementite, to the bulk ferrite, which is a carbon lean region. The cementite dissolution in deformed samples upon annealing at 300 °C, leads to significant dislocationcarbon interaction as schematically shown in Figure 7-9(b) resulting in the formation of a Cottrell atmosphere [13,14] which ultimately leads to a hardness increase as observed in Figure 7-8 in the pearlite. The presence of dislocations and solute gradients in bulk ferrite can facilitate carbon diffusion from the ferrite/cementite interface to bulk ferrite leading to Cottrell formation and hardness increase. As alloy 3 consists of a higher pearlite fraction than alloy 2, a higher amount of carbon dissolution might take place resulting in higher carbon dislocation interaction causing higher hardness increases in both ferrite-pearlite as observed in Figure 7-8 and reported in chapter 5. On annealing at 500 °C, the dislocation density decreases in the bulk ferrite, pearlite band and leaves behind the carbon that pinned the dislocations, alongside fragmentation and spherodization of cementite as shown in Figure 7-9(c). An increase in temperature also causes enhanced carbon diffusion to bulk ferrite due to solute gradient as reported in previous work [11,12]. These sub-structural changes result in overall strength or hardness decrease. It may be noted that the cementite fragmentation and dislocation annihilation result in a higher amount of strength drop in the pearlite in alloy 3 and alloy 2. In bulk ferrite excess carbon due to enhanced diffusion driven by solute gradient and the carbon left behind by the annihilated dislocations can redistribute and enhance the formation of precipitates, which retard the recovery process by pinning the subgrain boundaries in alloy 3 and alloy 2 [11,12,15]. A higher amount of precipitates might present in alloy 3 compared to

alloy 2 which might cause less decrease in hardness are higher retardation of recovery. Further increasing the temperature to 700 °C, resulted in boundary mobility by recrystallization of ferrite. The difference in the hardness of recrystallized and recovered ferrite in alloys 3 and 2 is well captured.

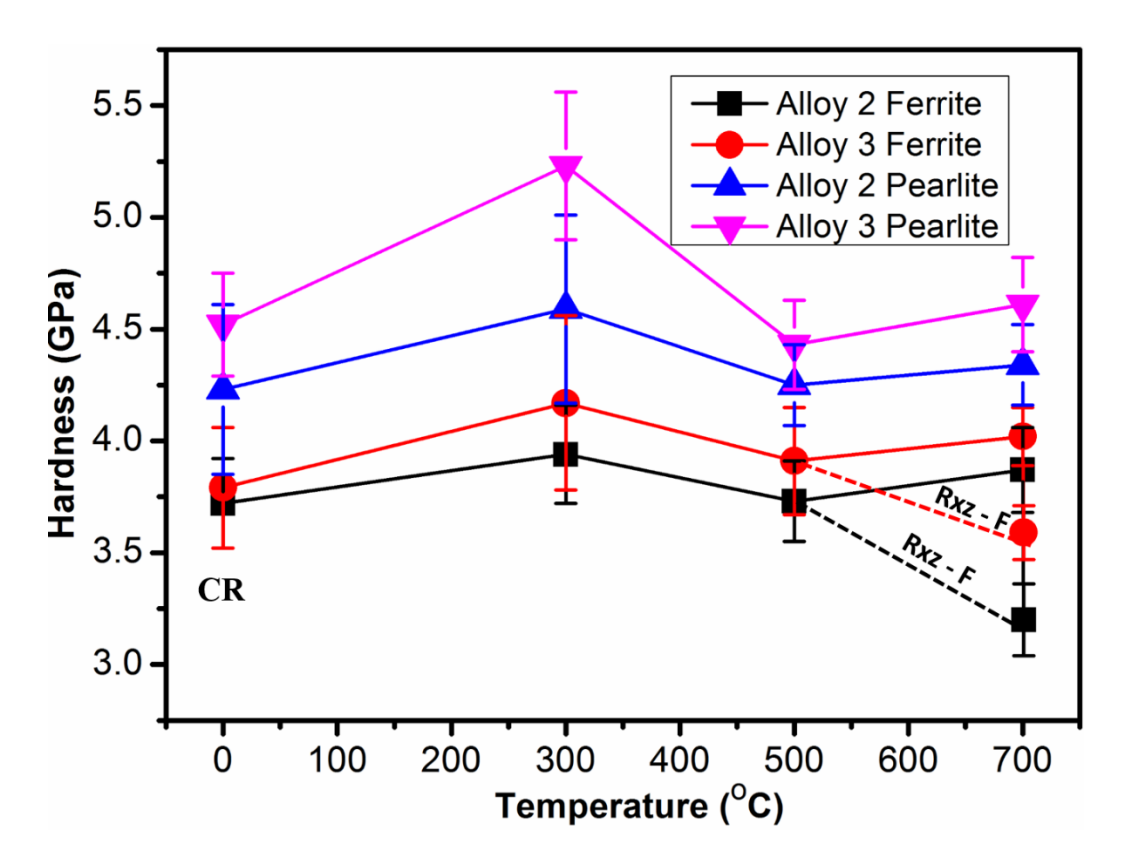


Figure 7-8 Shows hardness vs temperature in individual phases of ferrite and pearlite in alloy 2 and alloy 3.

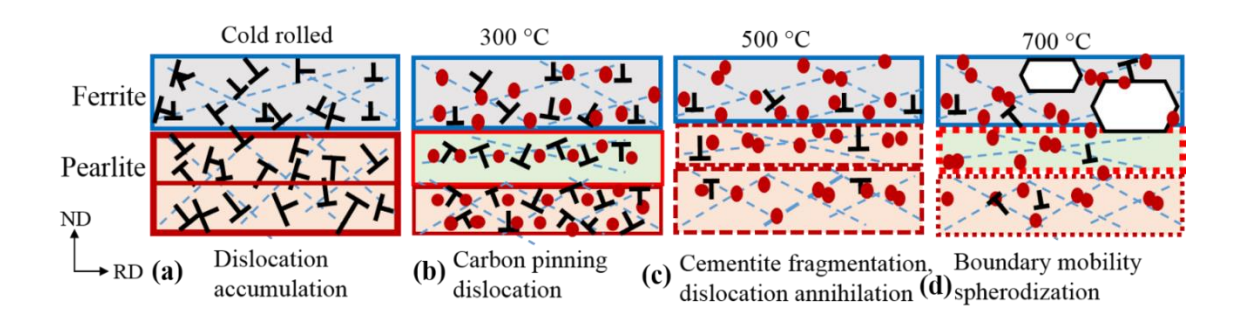


Figure 7-9 schematic of structural changes in ferrite- pearlite in (a) cold rolled state, recovery at (b) 300 (c) 500 °C and partial recrystallization (d) 700 °C.

7.5 Summary and conclusions

The chapter focuses on partial recrystallization of 80% cold-rolled steel sheets consisting of ferrite-pearlite in three different AHSS. Mainly pearlite fraction and its distribution were varied to investigate the role of pearlite on boundary mobility response at 700 °C for various soaking times. Using complementary techniques such as nanoindentation and electron microscopy with EBSD gave a better understanding of the role of pearlite during boundary mobility. The reasons for the same are well summarized and the following conclusions can be drawn:

- Annealing at 700 °C resulted in partial recrystallization of ferrite, along with its showing the presence of recovered ferrite, and pearlite where cementite is completely spherodized.
- 2. KAM maps show recrystallized ferrite having misorientation less than 1 degree, recovered ferrite having misorientation higher than 1 degree.
- 3. Nanoindentation was able to capture the hardness of the recrystallized ferrite (boundary mobility response), recovered ferrite and pearlite at the micrometer length scale.

- 4. The lowest hardness in recrystallized ferrite is due to defect-free grains. In recovered ferrite, carbide pining dislocations or subgrain/grain boundaries and retard the process of recrystallization and lead to higher hardness. Maximum hardness in pearlite can be linked to the presence of cementite (spherodized) with ferrite.
- 5. The hardness difference across the different alloys was also well captured in recrystallized, recovered ferrite and pearlite.

A much more systematic study is required at a fixed recrystallization fraction to get a better understanding and insights into the recrystallization of HSS/AHSS.

References

- [1] C.C. Tasan, M. Diehl, D. Yan, M. Bechtold, F. Roters, L. Schemmann, C. Zheng, N. Peranio, D. Ponge, M. Koyama, K. Tsuzaki, D. Raabe, An Overview of Dual-Phase Steels: Advances in Microstructure-Oriented Processing and Micromechanically Guided Design, Annu. Rev. Mater. Res. 45 (2015) 391–431. https://doi.org/10.1146/annurev-matsci-070214-021103.
- [2] C. Zheng, D. Raabe, Interaction between recrystallization and phase transformation during intercritical annealing in a cold-rolled dual-phase steel: A cellular automaton model, Acta Mater. 61 (2013) 5504–5517. https://doi.org/10.1016/j.actamat.2013.05.040.
- [3] T. Nanda, V. Singh, V. Singh, A. Chakraborty, S. Sharma, Third generation of advanced high-strength steels: Processing routes and properties, Proc. Inst. Mech. Eng. Part L J. Mater. Des. Appl. 233 (2019) 209–238. https://doi.org/10.1177/1464420716664198.
- [4] N. Peranio, Y.J. Li, F. Roters, D. Raabe, Microstructure and texture evolution in dual-phase steels: Competition between recovery, recrystallization, and phase transformation, Mater. Sci. Eng. A. 527 (2010) 4161–4168. https://doi.org/10.1016/j.msea.2010.03.028.
- [5] J. Teixeira, M. Moreno, S.Y.P. Allain, C. Oberbillig, G. Geandier, F. Bonnet, Intercritical

- annealing of cold-rolled ferrite-pearlite steel: Microstructure evolutions and phase transformation kinetics, Acta Mater. 212 (2021). https://doi.org/10.1016/j.actamat.2021.116920.
- B. Hutchinson, Practical aspects of texture control in low carbon steels, Mater. Sci. Forum. 157–6 (1994) 1917–1928. https://doi.org/10.4028/www.scientific.net/msf.157-162.1917.
- [7] H. Ghiabakloo, M. Kazeminezhad, Rapid annealing of severely deformed low carbon steel in subcritical temperature range, Met. Mater. Int. 23 (2017) 984–993. https://doi.org/10.1007/s12540-017-6753-2.
- [8] J. Gautam, A. Miroux, J. Moerman, C. Barbatti, P. Van Liempt, L.A.I. Kestens, Determination of the non-recrystallisation temperature (Tnr) of austenite in high strength C-Mn steels, Mater. Sci. Forum. 706–709 (2012) 2722–2727. https://doi.org/10.4028/www.scientific.net/MSF.706-709.2722.
- [9] S. Janakiram, J. Gautam, L.A.I. Kestens, Effect of pearlite morphology on recrystallization behaviour in cold rolled high strength automotive steel sheets, J. Phys. Conf. Ser. 1270 (2019). https://doi.org/10.1088/1742-6596/1270/1/012015.
- [10] S.I. Wright, M.M. Nowell, And, D.P. Field, 2011 a_review_of_strain_analysis_using_ebsd_hr Rxz with KAM.pdf, (n.d.). https://doi.org/10.1017/S1431927611000055.
- [11] D.H. Shin, K.T. Park, Y.S. Kim, Formation of fine cementite precipitates in an ultra-fine grained low carbon steel, Scr. Mater. 48 (2003) 469–473. https://doi.org/10.1016/S1359-6462(02)00512-2.
- [12] D.H. Shin, Y.S. Kim, E.J. Lavernia, Formation of fine cementite precipitates by static annealing of equal-channel angular pressed low-carbon steels, Acta Mater. 49 (2001) 2387–2393. https://doi.org/10.1016/S1359-6454(01)00165-3.
- [13] A.H. Cottrell, B.A. Bilby, Dislocation theory of yielding and strain aging of iron, Proc. Phys. Soc. Sect. A. 62 (1949) 49–62. https://doi.org/10.1088/0370-1298/62/1/308.
- [14] N, Mossbauer Effect in Deformed Fe-C Alloys, 201 (1975) 201–210.
- [15] L. Storojeva, D. Ponge, R. Kaspar, D. Raabe, Development of microstructure and texture of medium carbon steel during heavy warm deformation, Acta Mater. 52 (2004) 2209–2220. https://doi.org/10.1016/j.actamat.2004.01.024.

Chapter 8

Summary and conclusions and future scope of work

8

The present chapter focuses on the overall summary and conclusions of the thesis investigated HSS/AHSS Steel during each stage of thermomechanical processing i.e. after cold rolling, early recovery, recovery regime and partial recrystallization. Mainly three different AHSS sheets consisting of ferrite-pearlite in comparison to single ferrite subjected to 80% cold-rolled steels were investigated. In three AHSS, pearlite fractions and their distribution were varied to investigate the role of pearlite at different annealing temperatures 300, 500 and 700 °C. Using complementary techniques a qualitative linking between microstructure changes observed from EBSD, TEM, and their corresponding changes in mechanical properties by micro Vickers hardness and nanoindentation were successfully investigated during each stage of thermomechanical processing. Deconvolution of individual phases gave a better understanding and insights into the driving force for recovery kinetics.

The reasons for the same are well summarized and the following conclusions can be drawn.

The following summary and conclusions can be drawn from the present work.

Microstructural evolution after hot rolling resulted in a single ferrite phase in alloy 1, and ferrite-pearlite in alloys 2-4. The fraction of pearlite and distribution varied in pearlite consisting of alloys 2-4, due to varying alloy chemistry mainly C-Mn content. Increasing Carbon content resulted from 7.6% pearlite in alloy 2, 29.5% in alloy 3 and 33.5 % in alloy 4. In Alloy 3 and alloy 4 the banded distribution of pearlite was linked to higher Mn content.

Cold rolling to 80% reduction resulted in severe pancaking of ferrite-pearlite grains and are aligned in the rolling direction. Micro Vickers hardness test reveals, an increase in hardness with the increase in pearlite fraction. Nanoindentation confirms higher hardness in pearlite regions compared to ferrite. Deconvolution of KAM and hardness maps in alloys 1-4, revealed, that in the ferrite phase, hardness and KAM values are independent of pearlite fraction (almost zero slope). In alloys, 2-4, in the pearlite phase, hardness is dependent upon the pearlite fraction, whereas KAM is independent of the pearlite fraction.

On annealing at 300 °C, single ferrite consisting alloy 1, hardness decreases from cold rolled state indicating recovered and confirmed by KAM maps. In alloys 2-4 consisting of ferrite-pearlite, hardness increases from cold rolled state. Hardness increase varied with pearlite fraction and soaking time. The presence of pearlite during early recovery annealing causes the dissolution of carbon from cementite leading to Cottrell formation in both ferrite and pearlite phases as confirmed by Nanoindentation mapping and TEM. Hardness increases with soaking time were modeled using the Cottrell equation. The recovery kinetics in the case of alloys 3 & 4 show a time exponent of $t^{2/3}$ expected for Cottrell kinetics. Alloy 2, deviates from $t^{2/3}$ kinetics

might be due to the lower area fraction of pearlite and also due to the presence of microalloying elements Nb. Cottrell kinetics is mainly driven by the pearlite fraction. An increase in pearlite fraction increases the amount of free carbon available for Cottrell formation and consequently leads to an increase in the solute content on dislocation causing a higher amount of hardness increase in both ferrite and pearlite. It was also well observed that sharpening of cell boundaries by dislocation rearrangement in cells leads to subgrain formation. Suggesting that concurrently recovery by dislocation rearrangement and Cottrell formation takes place, Cottrell being more dominant and causing hardness increase.

On annealing at 500 °C, in the single ferrite phase, alloy 1 recovery, recrystallization dominated as confirmed from KAM maps and leads to a significant decrease in hardness. In ferrite-pearlite consisting of alloys 2-4, hardness decreases with time, hardness decreases following a similar trend in all ferrite-pearlite consisting steels. Recovery is initiated in pearlite mainly by fragmentation-induced spherodization. Whereas recovery in ferrite is being retarded mainly due to pinning the dislocation and sub boundaries by carbides causing retardation as confirmed by TEM, EBSD and nanoindentation maps. Recovery in alloys 2-4 is dominated by the thermally activated process leading to structural changes such as spherodization cementite, dislocation annihilation and subgrain growth as confirmed by TEM and KAM maps. Recovery kinetics suggest that fractional change is a property that is inversely proportional to temperature and the logarithmic time and follows Khulmanns models.

response on grain boundary mobility was well captured by nanoindentation mapping and correlated well with the KAM and IQ maps. The difference between recrystallized, recovered ferrite and pearlite was also well captured. The hardness differences across all three alloys were also observed. A much more systematic study is required at a fixed fraction of recrystallization for insights on recrystallization.

Overall, after cold rolling defect dominating response, early recovery at 300 °C carbon dislocation interaction, recovery at 500 °C dislocation annihilation-cementite spherodization and partial recrystallization at 500 °C resulted in boundary mobility response was successfully captured and correlated.

8.1 Future scope of work,

As we have observed pearlite area fraction and its distribution is influencing the recovery, recovery further influences recrystallization. During intercritical recrystallization and the austenite, nucleation is a concurrent process and the difference in mechanical properties of individual phases might affect the morphology of austenite which affect the properties of dual or multiphase steels. The findings of this study have important implications in fine-tuning the processing like heating rate or soaking time or temperature of the intercritical annealing treatment, or may even lead to a better alloy design in terms of chemical composition for subsequent development of high and advanced high strength steels

As nanoindentation was able to capture the hardness difference between recrystallized, recovered ferrite and pearlite at micrometer length scale and the different temperature regime. The methodology used for deconvolution of individual phase's features from EBSD and their correlation with the properties were successfully in two phase's ferrite-pearlite, this can be further used to characterize and quantify the multiphase in AHHS steels.

Understanding recovery behavior of AHSS automotive steels

by Sabavath Janaikiram Naik

Submission date: 25-May-2022 11:31AM (UTC+0530)

Submission ID: 1843757178

File name: Sabavath_Janaikiram_Naik.pdf (9.57M)

Word count: 28586 Character count: 155044

Understanding recovery behavior of AHSS automotive steels

ORIGINALITY REPORT

10%

2%

10%

0%

SIMILARITY INDEX

INTERNET SOURCES

PUBLICATIONS

STUDENT PAPERS

PRIMARY SOURCES

3%

S Janakiram, Jai Gautam, P Sudharshan Phani, 1 Leo A I Kestens. "Microstructural and micro hardness variation during low temperature recovery annealing in C-Mn high strength Steels", Journal of Physics: Conference Series, 2019

Publication

S. Janakiram, P. Sudharshan Phani, Govind

2%

2

Ummethala, Sairam K. Malladi, J. Gautam, Leo A.I. Kestens. "New insights on recovery and early recrystallization of ferrite-pearlite banded cold rolled high strength steels by high speed nanoindentation mapping", Scripta Materialia, 2021

<1% "Proceedings of the 13th World Conference 3 on Titanium", Wiley, 2016 4 B. Vignesh, W.C. Oliver, G. Siva Kumar, P.Sudharshan Phani. <1% "Critical assessment of high speed nanoindentation mapping technique and data deconvolution on thermal barrier coatings", Materials & Design, 2019 Publication www.hindawi.com <1% 5 Internet Source "ICAA13 Pittsburgh", Springer Nature, 2016 <1% 6 Publication F HUMPHREYS. "The Deformed State", 7 Recrystallization and Related Annealing Phenomena, 2004 Publication

John Humphreys, Gregory S. Rohrer, Anthony 8 Rollett. "Recovery After Deformation", Elsevier BV, 2017

<1%

9

J.J. Roa, P. Sudharshan Phani, W.C. Oliver, L.

<1%

Llanes. "Mapping of mechanical properties at microstructural length scale in WC-Co cemented carbides: Assessment of hardness and elastic modulus by means of high speed massive nanoindentation and statistical analysis", International Journal of Refractory Metals and Hard Materials, 2018

Publication

etheses.whiterose.ac.uk

10 Internet Source

<1%

www.amse.org.cn

Internet Source

11

<1%

"Magnesium Technology 2014", Springer

<1%

Science and Business Media LLC, 2016

Publication

Fan Zhang, Annie Ruimi, David P. Field. "Phase 13 Identification of Dual-Phase (DP980) Steels by Electron Backscatter Diffraction and Nanoindentation Techniques", Microscopy and

Microanalysis, 2016

Publication

<1%

<1%

Marti@?nez-de-Guerenu, A.. "Recovery during
14 annealing in a cold rolled low carbon steel. Part I:
Kinetics and microstructural characterization",
Acta Materialia, 20040712

Publication

J.Z Zhao, A.K De, B.C De Cooman. "Kinetics of 15 Cottrell atmosphere formation during strain aging of ultra-low carbon steels", Materials Letters, 2000

<1%

Publication

Submitted to Indian Institute of Science,

<1%

16

Bangalore

Student Paper

Morris, M.A.. "High temperature properties of ductile Cu@?Al@?Ni shape memory alloys <1% with boron additions", Acta Metallurgica Et Materialia, 199207

A. V. Mikhailovskaya, I. S. Golovin, A. A. 18 Zaitseva, V. K. Portnoi, P. Dröttboom, J. Cifre. "Effect of Mn and Cr additions on kinetics of recrystallization and parameters of grainboundary relaxation of Al-4.9Mg alloy", The Physics of Metals and Metallography, 2013 Publication

<1%

users.encs.concordia.ca <1% 19 Internet Source Submitted to University of Wales Swansea <1% 20 Student Paper cronfa.swan.ac.uk <1% 21 Internet Source dspace.epoka.edu.al <1% 22 Internet Source Okan Poyraz, Bilgehan Ögel. <1% 23

"Recrystallization, grain growth and austenite formation in cold rolled steels during intercritical annealing", Journal of Materials Research and Technology, 2020

24 F HUMPHREYS. "Recrystallization of Two-Phase Alloys",

Recrystallization and Related < 1%

Annealing Phenomena, 2004

Publication

Lynn A. Boatner, Bryan C. Chakoumakos,

<1%

25

Sudharshan Phani Pardhasaradhi, Sebastien N. Dryepondt et al. "Cryo-quenched Fe-Ni-Cr alloy decorative steel single crystals II: Alloy phases, structure, hardness, tensile, tribological, magnetic and electronic properties", Journal of Alloys and Compounds, 2020 Publication

X. Sauvage, J. Copreaux, F. Danoix, D.

26

Blavette. "Atomic-scale observation and modelling of cementite dissolution in heavily deformed pearlitic steels", Philosophical Magazine A, 2009 Publication

Chen, Chi-Tsong. "Analog and Digital Control System Design", Oxford University Press

<1%

<1% P. Chatakanonda. "Water Uptake and Solid 28 Loss During Soaking of Milled Rice Grains", Water Properties in Food Health Pharmaceutical and Biological Systems ISOPOW 10 Reid/Water Properties in Food Health Pharmaceutical and Biological Systems ISOPOW 10, 05/14/2010 Publication epdf.pub Internet Source <1% 29 theses.insa-lyon.fr <1% 30 Internet Source www.oim.com <1% 31 Internet Source <1% Electron Backscatter Diffraction in Materials 32 Science, 2000. Publication

<1% Merriman, C.C.. "Orientation dependence of 33 dislocation structure evolution during cold rolling of aluminum", Materials Science & Engineering A, 20081025 Publication orbit.dtu.dk <1% 34 Internet Source Camila Pucci Couto. "The effect of hot-35 stamping process on the local electrochemical behaviour of the 22 MnB5 steel coated with hot-dip aluminium-silicon", Universidade de Sao Paulo, Agencia USP de Gestao da Informação Academica (AGUIA), 2021 Publication dokumen.pub <1% 36 Internet Source 37 hdl.handle.net <1% Internet Source www.mdpi.com 38 Internet Source

Chun, Y.B.. "Monte Carlo modeling of microstructure evolution during the static recrystallization of cold-rolled, commercial purity titanium", Acta Materialia, 200608

Publication

F HUMPHREYS. "Recovery After Deformation", 40 < Lange Recrystallization and Related Annealing Phenomena, 2004

Publication

Ishwar Kapoor, Yongjun Lan, Arjan Rijkenberg, 41 < 1% Geoff West, Zushu Li, Vit Janik. "Correlative analysis of interaction between recrystallization and precipitation during subcritical annealing of cold-rolled low-carbon V and Ti–V bearing microalloyed steels",

Materials Science and Engineering: A, 2020

Publication

K. Liu, X. Cao, X.-G. Chen. "Solid-State

<1%

42

Transformation of Iron-Rich Intermetallic Phases in Al-Cu 206 Cast Alloys During Solution Heat Treatment", Metallurgical and Materials Transactions A, 2013

43 0	P. Sudharshan Phani, W.C. Oliver. "A direct comparison of high temperature nanoindentation creep and uniaxial creep measurements for commercial purity aluminum", Acta Materialia, 2016 Publication	<1%
44	Rajesh Khatirkar, Basavaraj Vadavadagi,	<1%
	Satish Kumar Shekhawat, Arunansu Haldar, Indradev Samajdar. "Orientation Dependent	
	Recovery in Interstitial Free Steel", ISIJ	
	International, 2012	
	Publication	
	d-nb.info	
45 lr	nternet Source	<1%
	pdfs.semanticscholar.org	
46 lr	nternet Source	<1%
	www.dierk-raabe.com	
47 Ir	nternet Source	<1%
48	J. Laria, E. Meza, M. Mondragón, R. Silva, J.L.	<1%
	Peña. "Comparison of overall water uptake by corn	
	kernel with and without dissolved calcium	
	hydroxide at room temperature", Journal of Food	
	Engineering, 2005 Publication	

		OVERY AND <mark>49</mark> ON", Elsevier BV, 1996	<1%
"Con	tinuum Sca	le Simulation of Enginee	ring <1%
Materia Publication	als", Wiley,	2004	
	•	behaviors and effect fact el-base superalloys",	ors <1%
Materia Publication	als Science	& Engineering A, 200901	15
Exclude quotes	On	Exclude matches	< 14 words
Exclude bibliography	On		